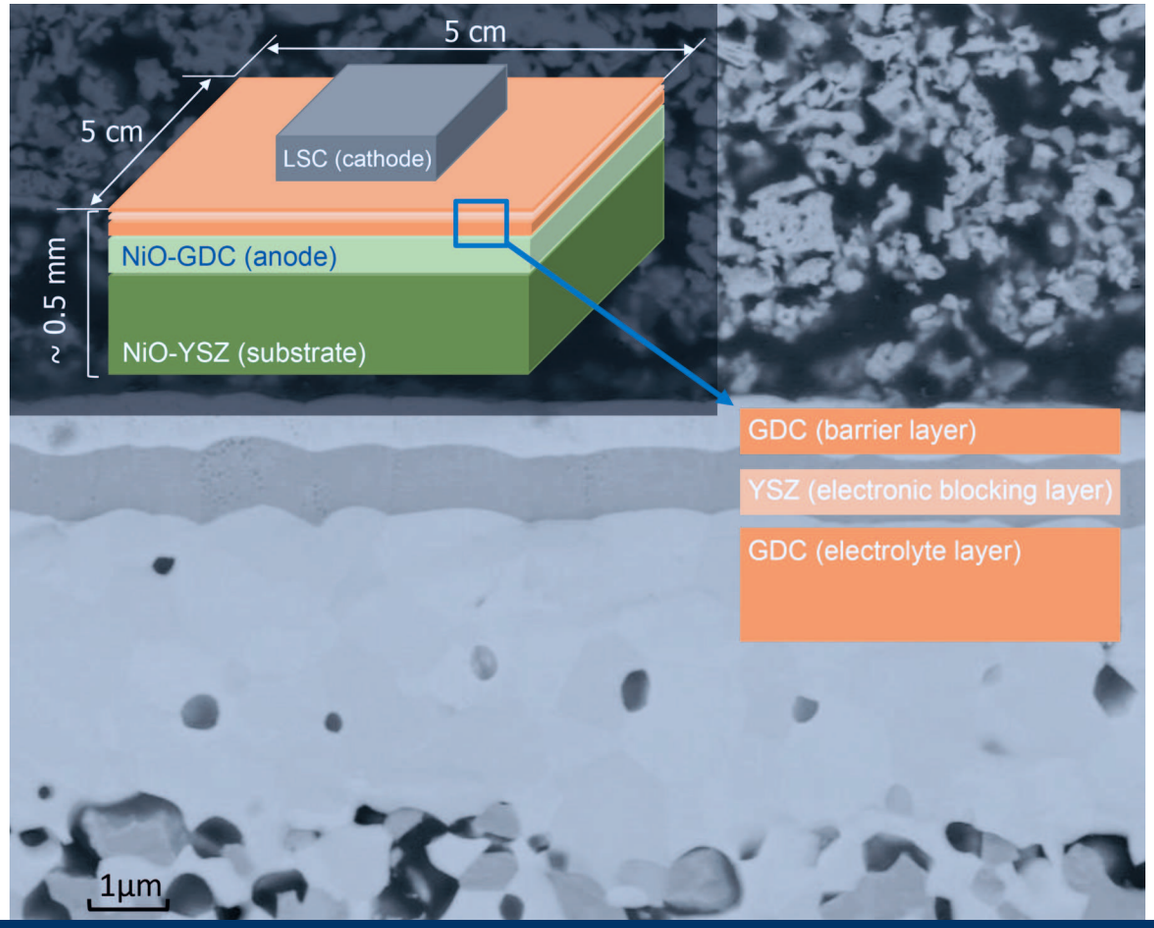

Electrolyte development for a SOFC operating at low temperature

Jun Zhang

Energie & Umwelt / Energy & Environment
Band / Volume 492
ISBN 978-3-95806-471-3

Mitglied der Helmholtz-Gemeinschaft

JÜLICH
Forschungszentrum

Schriften des Forschungszentrums Jülich
Reihe Energie & Umwelt / Energy & Environment Band / Volume 492

Forschungszentrum Jülich GmbH
Institut für Energie- und Klimaforschung
Werkstoffsynthese und Herstellungsverfahren (IEK-1)

Electrolyte development for a SOFC operating at low temperature

Jun Zhang

Schriften des Forschungszentrums Jülich
Reihe Energie & Umwelt / Energy & Environment Band / Volume 492

ISSN 1866-1793 ISBN 978-3-95806-471-3

Bibliografische Information der Deutschen Nationalbibliothek.
Die Deutsche Nationalbibliothek verzeichnet diese Publikation in der
Deutschen Nationalbibliografie; detaillierte Bibliografische Daten
sind im Internet über http://dnb.d-nb.de abrufbar.

Herausgeber
und Vertrieb: Forschungszentrum Jülich GmbH
Zentralbibliothek, Verlag
52425 Jülich
Tel.: +49 2461 61-5368
Fax: +49 2461 61-6103
zb-publikation@fz-juelich.de
www.fz-juelich.de/zb

Umschlaggestaltung: Grafische Medien, Forschungszentrum Jülich GmbH

Druck: Grafische Medien, Forschungszentrum Jülich GmbH

Schriften des Forschungszentrums Jülich
Reihe Energie & Umwelt / Energy & Environment, Band / Volume 492

D 82 (Diss. RWTH Aachen University, 2020)

ISSN 1866-1793
ISBN 978-3-95806-471-3

Vollständig frei verfügbar über das Publikationsportal des Forschungszentrums Jülich (JuSER)
unter www.fz-juelich.de/zb/openaccess.

ACKNOWLEDGMENTS

Many thanks to the people who gave me the continuous assistance and support in the last three years. Without you, I could not complete this work.

First of all, I would like to thank Prof. Dr. Olivier Guillon to agree to accept me as his doctoral student. Although as the director of our institute he is so busy, we still can have a lot of productive and fruitful discussions. I can still remember that when I had some problems, he was always able to pick up some books from his bookshelf or come out of some literature from his mind. His experience, knowledge, and working style, inspire and change me. Thank you!

Special thanks to Dr. Christian Lenser to be my scientific advisor. I could say that without the persistant guidance and support from him, this work is never possible to come out. He assisted me for some experiments hand by hand in the first two years; corrected every my written work again and again, some times even as tiny as a punctuation; practiced with me together for the rehearsal of every my presentations. Such kind of support is teaching me how to be a researcher step by step. Vielen Dank!

Special thanks also to Dr. Chih-Long Tsai for his very generous and kind help for my whole Ph.D. study. His rich experience and knowledge in the field of electrochemistry help me to deal with so many challenges related to that. Besides that, we are also very good friends out of work, sharing so many happy time of our two family.

I would also like to thank Prof. Dr. Christian Roos for agreeing to be a second reviewer for this work and for his help through the whole thesis procedure.

I would further like to thank the colleagues in SOCs department, Dr. David Udomsilp, Dr. Florian Thaler, Werner Herzhof, Ralf Kauert, Dr. Norbert H. Menzler, Dr. Mariya Ivanova, Dr. Siri Johanna Harboe and Mr. Fabian Grimm, for their help, support and discussions related to SOFC field, especially thank Dr. David Udomsilp for his generous help with some German translation.

Besides that, I would also like to thank the help of some colleagues in IEK-1, Dr. Sven Uhlenbruck for the helpful discussions of PVD; Mr. Frank Vondahlen for the conduction of PVD experiment; Mr. Mark Kappertz for the help of sample preparation for SEM; Dr. Doris Sebold for the help of SEM observation; Dr. Robert Mücke for the modelling; Mr. Kai Wilkner for the help of "Cyber Scan" to measure the surface roughness and bending behavior; Dr. Tim Van Gestel for the help of sample preparation for the fractured SEM check; Dr. Yoo Jung Sohn for the XRD measurement; Ms. Sigrid Schwartz-Lückge for the B.E.T

characterization; Ms. Andrea Hilgers for the viscosity and particle size distribution characterizations; Dr. Anna Windmüller for the help of VISA application; Ms. Vanessa Rossaint, Ms. Yvonne Lichtenfeld, Ms. Vicky Tirtey and Mr. Stefan Weitz for all the administration things.

In addition to our colleagues in IEK-1, Ms. Cam-Ahn Thieu and Dr. Ji-Won Son from Center of Energy Materials Research, KIST, Korea; Mr. Niklas Russner, Dr. André Weber from Institut für Angewandte Materialien – Werkstoffe der Elektrotechnik, KIT, Germany; Mr. Yujie Wu, Mr. Kangwei Wei and Prof. Yihan Lin from China University of Mining and Technology, CMUT, China, are all appreciated for their help with single cell performance tests.

I would further like to thank some Chinese Friends for their shared happy time: Dr. Bowen Lv, Mr. Tu Lan, Dr. Qianli Ma, Ms. Chen Cao, Dr. Guanghu He, Dr. Dapeng Zhou, Dr. Wenting He, and Dr. Yang Liu.

I would also like to thank the China Scholarship Council (CSC, with number of 201606460053) for the financial support.

Last but not least, I would like to express a great debt of gratitude to my family. My parents, whose fundamental support could not be described by several words but I want to say that without you, I could not get this far. My parents-in-law, who stand behind me and encourage me all the time. And most importantly, my beautiful and wonderful wife, Yi, who devotes herself to our family and brought me a biggest gift during my Ph.D. study, our lovely daughter, Yisu. Ph.D. study sometimes is boring, challenging and depressing, but with you two lighting up the light of my life, sharing the joyful time, accompanying me all the time, I finally reach here. Thank you!

Jülich, Germany

CONTENTS

1

INTRODUCTION

Wherever and whenever people live and work, energy is consumed. Today, we still rely mostly on the energy resources derived from the finite and polluting fossil fuels (seen in Figure 1.1).

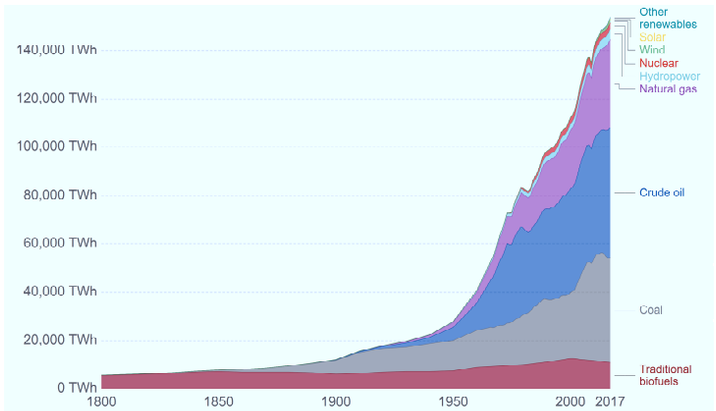

Figure 1.1: Global primary energy consumption (measured in terawatt-hours (TWh) per year, here 'other renewable' are renewable technologies not including solar, wind, hydropower and traditional biofuels)[1]

The annual "BP Statistical Review of World Energy" from British Petroleum (BP) published in 2018 concluded that the world had 50.2 years of oil and 134 years of coal left at the current rate of production [1]. However, depending on the way of use, we may reach that day sooner or later. According to the data from "World Development Indicators" by World Bank [2], carbon dioxide (CO_2) accounts for around three-quarters of the total greenhouse gas emissions. While the top two sources of CO_2 are coal and oil, accounting for 41.3 % and 38.4 %, respectively. The temperature is projected to increase around 3.1–3.7 °C by the end of this century, if the current trend of CO_2 emission continues.

Therefore, to create an environmentally friend and sustainable economic system, we must lower the consumption of fossil fuels by replacing them with renewable energy sources and improving the efficiency of energy consumption. Solid oxide fuel cells (SOFCs) are energy conversion devices which can convert a wide variety of fuels, such as H_2, CH_4 or CO, into electricity with high efficiency (electricity efficiency of more than 60 % [3]), but low emission of greenhouse gas.

The typical operating temperature of state-of-the-art SOFCs is around 700–850 °C, providing important advantages including high efficiency,

production of waste heat, and the ability of internal reforming of fuel. However, the availability of low temperature SOFC (LT-SOFC) will broaden the potential applications of SOFC beyond stationary applications to small-scale, portable applications in transport and mobility, as the low operation temperature can further reduce system costs by allowing the use of cheap materials for interconnects, non-glass seals, shortening the start-up time, and slowing down the thermal degradation rate [4, 5].

The main purpose of this thesis is the fabrication of a thin and high conductivity electrolyte on an anode support. As a first step, a suitable material is chosen. As a second step, a thin and dense electrolyte is fabricated and characterized. Chapter 2 introduces the basic knowledge of solid oxide fuel cell, including its operation, principle and development. A literature review of the material science and fabrication techniques of electrolyte is presented. Chapter 3 discusses all the experimental techniques used for this study. Chapter 4 compares the ionic conductivity of YSZ, ScSZ, and GDC by using electrochemical impedance spectroscopy (EIS). The properties of starting powders, powder processing and the microstructure after sintering are taken into account. Chapter 5 talks about the fabrication of a thin GDC electrolyte using screen printing. The fabrication on two different substrates, synthesis of a screen printing paste, drying, sintering and reducing behavior of the fabricated layer, as well as the single cell performance are discussed. Chapter 6 summarizes this work and gives an outlook.

2 BACKGROUND AND THEORY

This chapter begins with a brief introduction of SOFC, on the subjects of working principle, different components involved, development history, basic electrochemistry. Then, the material science of several frequently investigated electrolytes is reviewed, with regard to material properties, advantages and disadvantages as usage of electrolyte for SOFC. After that, various fabrication methods of thin electrolyte layers are presented. Finally, a short summary is given.

2.1 SOLID OXIDE FUEL CELL (SOFC)

SOFC is an energy conversion device that can convert chemical energy of a fuel (such as H_2 or CH_4) into electricity through electrochemical reactions. As a result, the efficiency of SOFC is not limited by the theoretical Carnot efficiencies since the electrical work is directly converted from a substantial fraction of the enthalpy associated with the electrochemical oxidation of the fuel into water and/or carbon dioxide, without a combustion process. Therefore, SOFCs can deliver higher electrical conversion efficiencies and produce less (or negligible) SO_x and NO_x emissions when compared to traditional technologies such as coal-fired power plants and electrical generators based on internal combustion engines. In addition to high efficiency, SOFCs have two major advantages compared with other fuel cells due to the high operation temperature of 700–1000 °C. First, not only H_2 but also a wide variety of other fuels, ranging from carbon to hydrocarbons, can be used as fuel for SOFC without an external reformer. Second, the significant amount of exhaust heat produced by SOFCs can be used in combined heat and power system (CHP). For example, Mitsubishi heavy industries reported a power generation efficiency of up to 70 % by applying the exhaust heat to a gas turbine combined-cycle power generation [6] and Forschungszentrum Jülich reported an electrical efficiency of more than 60 % [3]. In addition, quiet and vibration-free operation of SOFC also eliminates the usual noise associated with power generation systems [7–9], which is a significant advantage for some specific applications, i. e., recreational vehicles or the marine sector.

2.1.1 *Working principle*

A SOFC consists of two porous electrodes, separated by a dense electrolyte (seen in Figure 2.1). On the anode side, fuel gas, such as H_2 and/or CH_4, CO, etc., is oxidized by the oxygen ions, coming from

the cathode through the electrolyte, into H_2O and/or CO_2, releasing electrons. On the cathode side, the oxygen gas is reduced into oxygen ions. Under the electromotive force caused by the different oxygen chemical potential, the oxygen ions migrate through the electrolyte to the anode, while the electrons flow around an external circuit, producing electric power. The half-reactions happening at the two electrodes are summarized as following:

$$\begin{aligned} \text{anode:} \quad & H_2 + O^{2-} \rightarrow H_2O + 2e^- \\ & CH_4 + {}_4O^{2-} \rightarrow CO_2 + {}_2H_2O + 8e^- \\ & CO + O^{2-} \rightarrow CO_2 + 2e^- \\ \text{cathode:} \quad & O_2 + 4e^- \rightarrow 2O^{2-} \end{aligned} \tag{2.1}$$

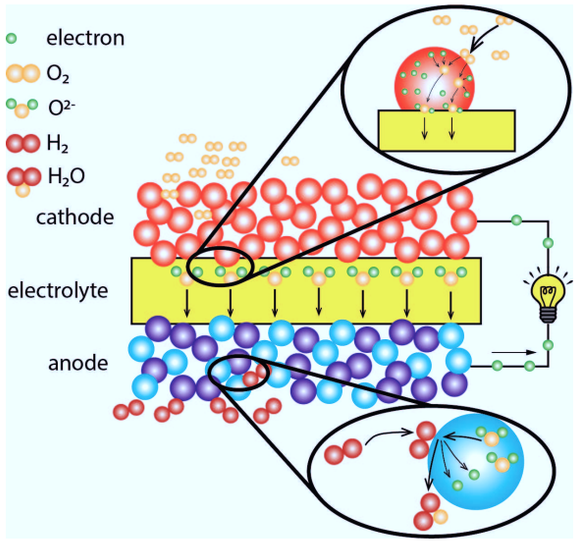

Figure 2.1: The working principle for SOFC

2.1.2 *SOFC development*

The majority of SOFC development to date focuses on electrolyte-supported cells (ESCs), anode-supported cells (ASCs) and metal-supported cells (MSCs), named after the structural support. The structures are illustrated in Figure 2.2.

ESCs, often called the first generation SOFCs, have a thick electrolyte layer (typically around 100–1000 μm). The ESCs have two main advantages: first, the manufacturing flexibility, the electrolyte can be fully sintered prior to the electrode sintering to avoid some reported degradation caused by the co-sintering of electrolyte and electrode

[10, 11]; second, the less susceptibility of the anode to be re-oxidized. On the other hand, a significant degree of ohmic resistance is caused by the thick electrolyte. Therefore, ESCs have to be operated at high temperature (around 850–1000 °C) to minimize the ohmic resistance.

ASCs, the second generation SOFCs, with a thick anode as the structural support, are developed with a much thinner electrolyte (typically around 10 μm, can be as thin as several hundred nm) compared to ESCs to decrease the ohmic resistance. Therefore, lower operation temperature below 850 °C is possible for the ASCs. However, the thick anode support potentially limits the mass transportation to the electrochemical reaction area close to the electrolyte, leading to a higher polarization resistance. Moreover, a thin but gas-tight electrolyte is a significant challenge of fabrication.

Compared to the all-ceramic-based SOFC discussed above, MSCs, referred as the third generation SOFCs, apply a porous metal as the structural support. Therefore, MSCs have the potential advantages of lower material cost and easier cell assembling (the use of conventional metal joining techniques, such as welding or brazing for sealing) [12]. Besides the cost decrease, introduction of alloy support in the cell is expected to improve the mechanical strength of substrate and the tolerance to redox cycles. Therefore, MSCs have attracted attention for non-stationary applications such as auxiliary power units (APUs). However, their practical performance is still lower than state-of-the-art ASCs.

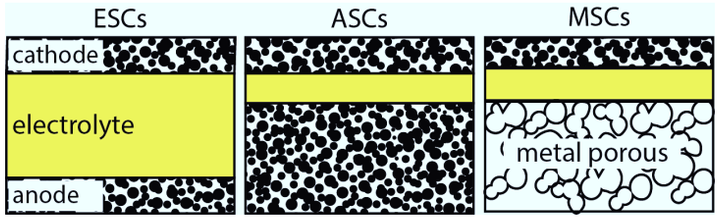

Figure 2.2: The development of SOFC

2.1.3 *Electrochemistry*

As we see in the working principle of SOFC, the basic reaction is (assuming pure H_2 is used):

$$H_2 + \frac{1}{2}O_2 \rightarrow H_2O \tag{2.2}$$

Then, the change of the Gibbs free energy of formation, $\Delta\bar{G}_f$, gives us the energy produced by Equation 2.2 (assuming pure H_2 and O_2 at standard pressure, 0.1 MPa):

$$\Delta\bar{G}_f = (\bar{G}_f)_{H_2O} - (\bar{G}_f)_{H_2} - \frac{1}{2}(\bar{G}_f)_{O_2} \tag{2.3}$$

where $(\bar{G}_f)$ means molar specific Gibbs free energy of formation.

Assuming cell losses are neglected, the total released Gibbs free energy is converted into electricity by driving 2N electrons (from each molecule of H_2, N is the Avogadro constant) from anode to cathode through an external circuit, implying following equation:

$$\Delta\bar{G}_f = -2NeE = -2FE \tag{2.4}$$

where E is the voltage of the cell, $-e$, the charge on one electron, F, the Faraday constant. Thus,

$$E = \frac{-\Delta\bar{G}_f}{2F} \tag{2.5}$$

The Equation 2.5 defines the electromotive force (EMF) for the reaction Equation 2.2.

However, it should be pointed out that Equation 2.5 only takes the temperature into consideration but does not consider the reactant pressure and concentration effects. For example, the actual fuel condition for a fuel cell might be a mixture of H_2 and minor H_2O while the oxidant condition is the ambient air (O_2 has a partial pressure of 0.021 MPa in air). In other words, taking the corresponding partial pressure of the reactants into consideration, Equation 2.3 is changed to [13, 14]:

$$\Delta\bar{G}_f = \Delta\bar{g}_f^0 - RT\ln\frac{p_{H_2}p_{O_2}^{1/2}}{p_{H_2O}} \tag{2.6}$$

where $\Delta\bar{G}_f^0$ is the change in molar Gibbs free energy of formation at standard pressure.

Combining Equation 2.5 with Equation 2.6 yields the "Nernst equation":

$$\begin{aligned} E &= \frac{-\Delta\bar{G}_f^0}{2F} + \frac{RT}{2F}\ln\frac{p_{H_2}p_{O_2}^{1/2}}{p_{H_2O}} \\ &= E_0 + \frac{RT}{2F}\ln\frac{p_{H_2}p_{O_2}^{1/2}}{p_{H_2O}} \end{aligned} \tag{2.7}$$

where E_0 is the EMF at standard pressure.

Figure 2.3 shows the typical current-voltage curve (I-V curve) of a SOFC. The characteristic shape of the I-V curve is resulted from different losses in the cell discussed below.

A. The activation loss, η_{act}, consists of two parts, anode and cathode activation losses, caused by the slow electrocatalytic (charge transfer) reaction. The well-known Bulter-Volmer equation[16] describes the η_{act} in (the following equation applies separately at the anode and cathode):

$$i = i_0(\exp\frac{\alpha_1 F\eta_{act}}{RT} - \exp\frac{\alpha_2 F\eta_{act}}{RT}) \tag{2.8}$$

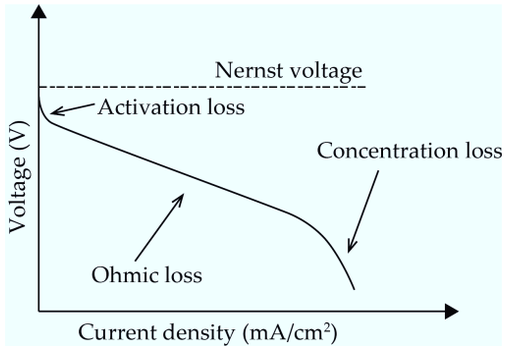

Figure 2.3: Ideal and actual performance of a fuel cell with respect to the potential current response [15]

where i_0 is the exchange current density, defined as the equal forward and reverse flow of electrons across the electrode-electrolyte interface under open-circuit conditions. The i_0 is of crucial importance as it determines the magnitude of the η_{act}, therefore, a good electrode is characterized by an i_0 with high value. Evidenced from Equation 2.8, activation loss dominates at low current density.

B. The ohmic loss, η_{ohm}, is caused by the resistance to the flow of ions in the electrolyte and electrodes. It is generally accepted by the SOFC community that ohmic resistance is mainly caused by electrolyte (though in a stack, this might be different as the cell contact resistance is also significant), therefore, η_{ohm} is described by:

$$\eta_{ohm} = iR \tag{2.9}$$

where R is the ohmic resistance of the electrolyte. Due to the linear behavior between η_{ohm} and i, the observed linear I-V curve at intermediate current density is caused by the ohmic resistance.

C. Concentration loss, η_c: it is evident that during the cell operation there is a reduction of hydrogen concentration. The extent to decrease depends on the current density taken from the fuel cell and the velocity of the fuel provided externally[17]. This change in concentration causes a reduction in the p_{H_2}. According to Equation 2.7, the reduction in gas pressure results in a reduction in voltage. For an SOFC operating on H_2 fuel, the concentration loss can be expressed by[16]:

$$\eta_c = \frac{-RT}{4F}[\ln(1 - \frac{i}{i_{L,c}}) + 2\ln(1 - \frac{i}{i_{L,a}})] \tag{2.10}$$

where i_L is the limiting current density, defined as the maximum possible current density for which the reactants are consumed at

their maximum possible replenishment rates. Expected from this equation, η_c becomes important at high current density.

D. Other losses due to internal current and/or gas leakage. It is easy to understand that a leaky electrolyte drops the cell voltage due to the reduced gradients in Equation 2.7. Similarly, an electron conducting electrolyte decreases the cell performance by allowing electrons transport through electrolyte rather than external circuit to the cathode.

2.1.4 *Components*

2.1.4.1 *Anode*

As introduced before, anode is where the electrochemical oxidation of the fuel happens, associated with transfer of electrons and oxygen ions. Therefore, it must have a porous structure for the gas diffusion, good catalytic properties for the electrochemical reactions, and adequate mixed ionic and electronic conductivity (MIEC). The latter can either be achieved by a single MIEC material, or a cermet of a metal and an ion conductor.

The reducing atmosphere at the anode allows use of metal as anode material. However, the stability of anode at elevated operation temperature of SOFC (around 850 °C) must also be considered and that limits the material choice to nickel, cobalt and some noble metals. But only nickel is widely used in SOFCs because of its low cost (compared to precious metals) and high catalytic activity. However, there are still two main concerns about the use of pure nickel as anode. First, the sintering of Ni in long-term operation at high temperature, results in loss of active surface area. Second, the significant degree of mismatch of thermal expansion coefficient (TEC) of Ni ($14.5 \times 10^{-6}\,K^{-1}$) compared to the solid electrolytes, for example, yttria-doped ZrO_2 (YSZ) ($10.5 \times 10^{-6}\,K^{-1}$) [18], could cause cracking or delamination during fabrication and operation. Therefore, an SOFC anode cermet is commonly made from the mixture of electrolyte materials and nickel, where the electrolyte material could inhibit coarsening of the nickel particles at the fuel cell operating temperature and provide an anode TEC acceptably close to the electrolyte. Additionally, the introduction of electrolyte material in anode offers a significant part of ionic conductivity to the overall conductivity. Since the anode is fabricated in air, NiO is used as a starting material. The porosity of the anode is formed through the *in situ* reduction of NiO to Ni when exposed to the reducing atmosphere, caused by the oxygen loss and concomitant volume change.

The anode structure for anode-supported SOFC is normally made of two layers. One is thicker (around a few hundred micrometer) support layer, normally called substrate, and the other is an inner thinner (around several micrometer) electrochemically active anode

layer. The fabrication of anode support layer has switched from warm pressing [19] to tape casting [20–22] while the deposition of anode layer has changed from vacuum slip casting to screen printing at Forschungszentrum Jülich [22] due to a better scalability (automated and continuous operation). The anode support is fabricated by tape casting a slurry of NiO/YSZ mixture with one composition of coarse particles, while the anode is fabricated by screen printing a paste of NiO/YSZ mixture with a different composition of finer particles. By controlling the slurry composition and processing of these two anode layers, the anode microstructure has higher porosity and finer grains than the anode support because of the different functions of each layer. The main role of the coarse anode support includes the mechanical support of the cell, rapid transport of fuel, and electrical connection, while the finer anode acts to maximize the electrochemical reaction area and mitigates the TEC mismatch between anode and electrolyte.

Despite the fact that NiO/YSZ is currently the state-of-the-art anode, there is much interest in developing alternative anode to the NiO/YSZ cermet, such as using gadolinium doped ceria (GDC) instead of YSZ [23–28]. As mentioned before, one distinguished advantage of SOFC over other fuel cells is its variety of fuels. However, when biomass is applied to SOFC, the tar impurity in the fuel induces carbon deposition on Ni containing anodes[29–31], resulting in nickel particle coarsening and depletion, which degrades the cell performance. An efficient solution would be to employ materials with higher resistance towards carbon deposition, such as Ni-GDC based cermet [28, 31], since ceria has a better tolerance of carbon precipitation and is able to electrochemically oxidize carbon.

2.1.4.2 *Cathode*

The cathode functions as the site for the electrochemical reduction of oxygen. Therefore, similar to the anode, the cathode also must have: (1) high MIEC; (2) matched TEC with the electrolyte; (3) adequate porosity to allow gas diffusion and electrochemical reaction; (4) stability under oxidizing atmosphere during fabrication and operation; (5) high catalytic effect for the oxygen reduction reaction (ORR).

The most widely used materials for SOFC cathode are perovskites with the general formula $ABO_{3-\delta}$, in which A and B are cations with a total nominal charge of +6. Illustrated in Figure 2.4 is the general crystal structure of $ABO_{3-\delta}$, related to the electronic and ionic transport properties of some transition-metal oxides. In this case, the A site is usually occupied by a mixture of rare earth elements (typically La) and alkaline earth elements (such as Sr, Ca and Ba), while the B site is occupied by reducible transition metals such as Mn, Fe, Co, or Ni (or combinations thereof). The octahedral symmetry around the transition metal often promotes a metallic or semiconducting band structure at high temperature, leading to high electronic conduction. Such structure

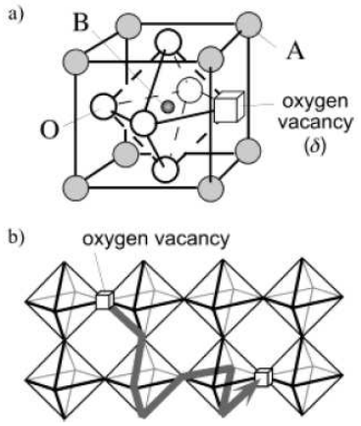

Figure 2.4: Atomic structure and oxygen transport in mixed conducting perovskites $ABO_{3-\delta}$. (a) Basic structure. (b) Bulk oxygen transport mechanism [32]

is also quite stable relative to other crystalline phases, and thus with a judicious choice of A- and B-site cations, it can support a large number of oxygen ion vacancies at SOFC operating conditions, thus facilitating significant bulk ionic oxygen transport [32].

For high operation temperature (> 800 °C), $La_{1-x}Sr_xMnO_{3-\delta}$ (LSM) is the state-of-the-art cathode material due to its excellent properties in terms of high electrical conductivity (200–300 $S\,cm^{-1}$ at 900 °C) [33]; high thermal stability; and compatibility with electrolyte material YSZ [34–36]. However, the poor electrocatalytic activity with decreasing temperature of LSM limits its application at low temperature. Research nowadays aims at developing cathode materials with higher electrocatalytic activity than LSM at low temperature. For example, the iron and cobalt containing perovskite, $La_{1-x}Sr_xCo_{1-y}Fe_yO_{3\pm\delta}$ (LSCF), is another state-of-the-art cathode material developed for SOFC operating below 800 °C. It has a good compromise between the high ionic and electronic conductivity and good ORR (given by the Co cation). Another cobalt-analogon to LSM, $La_{1-x}Sr_xCoO_{3-\delta}$ (LSC), also has higher ionic and electronic conductivity than LSM. Though LSC is reported to have a much higher TEC ($21.3 \times 10^{-6}\,K^{-1}$) [37], the single use of LSC presents higher performance than LSCF and no cracking is found between the cathode and electrolyte in Han et al.'s [38] report. Additionally, Shao and Haile [39, 40] reported another cathode material, $Ba_{0.5}Sr_{0.5}Co_{0.8}Fe_{0.2}O_{3-\delta}$ (BSCF), which has extremely low area specific resistance at low temperatures, only 0.055–0.071 $\Omega\,cm^2$ at 600 °C and 0.51–0.60 $\Omega\,cm^2$ at 500 °C. However, BSCF has issues of structural instabilities at intermediate temperature. For example, an exponential decay in the measured oxygen permeation flux of BSCF is observed at temperature below 825 °C [41]. Some other groups revealed that this

degradation is resulted from a phase transition from a cubic structure into a two-phase mixture of hexagonal and cubic perovskites [42–44].

2.1.5 *Electrolyte*

As the main topic of this dissertation, the electrolyte is reviewed in terms of materials science and processing in the following in detail.

2.2 ELECTROLYTE FOR SOFC

2.2.1 *Requirements*

As introduced in the operation principle of a SOFC, an electrolyte is inserted between the cathode and anode, and thereby has two main functions:

1. conducting oxygen ions from cathode to anode;
2. separating reducing atmosphere (fuel side) from oxidizing gas (air side).

By definition of its role, requirements that need to be met for the electrolyte materials are [7–9]:

1. high oxygen ion conductivity and negligible electron conductivity;
2. chemical compatibility with electrodes;
3. chemical stability under both oxidizing and reducing atmosphere;
4. mechanical stability against thermal cycling (match of TEC between electrolyte and electrodes);
5. low cost of material and fabrication.

It is true that even up to today, no single electrolyte material can meet the requirements all at once. Therefore, the choice of an electrolyte material is usually made on a promise of those criteria depending on the targeted application.

2.2.2 *Oxygen ion transport in the electrolyte*

The oxygen ions move diffusely: they "hop" randomly to available oxygen vacancies. Directed transport therefore requires a concentration gradient, as described in Fick's first law. Since diffusion requires a vacant site next to the diffusing particle, it is analytically much simpler to describe the movement of oxygen vacancies since a vacancy is usually surrounded by occupied sites and can therefore move freely, while a

lattice oxygen is usually surrounded by other lattice oxygen and cannot move. The oxygen vacancy conductivity can be determined by:

$$\sigma = n q \mu = [V_O^{\cdot\cdot}] q \mu \tag{2.11}$$

where n is the oxygen vacancy concentration, written as $[V_O^{\cdot\cdot}]$ (in Kröger-Vink notation); q is the charge of the carrier (here should be $2e$); μ is the mobility of the oxygen vacancy. The Nernst-Einstein equation correlates the mobility, μ , of oxygen vacancies with their diffusion coefficient, D,:

$$\mu = \frac{qD}{kT} \tag{2.12}$$

where k is the Boltzmann constant, T is absolute temperature. Following an analysis by Kilner [45] and considering the "dilute" [46] oxygen vacancy, the D can be determined by:

$$D = [V_O^{\cdot\cdot}] \gamma a_0^2 \nu_0 \exp\left(\frac{-\Delta E_a}{kT}\right) \tag{2.13}$$

where a_0 is the jump distance of the vacancy (half of the lattice parameter) and ΔE_a is the activation energy of migration, while ν_0 is the jump attempt frequency, and γ is a constant.

Correlating Equation 2.11, Equation 2.12 with Equation 2.13 lets us obtain:

$$\sigma = [V_O^{\cdot\cdot}] 2 q^2 a_0^2 \frac{\gamma \nu_0}{kT} \exp\left(-\frac{\Delta E_a}{kT}\right) \tag{2.14}$$

By defining a factor σ_0, the above equation can be simplified to

$$\sigma = \frac{\sigma_0}{T} \exp\left(\frac{-E_a}{kT}\right) \tag{2.15}$$

which is the common equation to describe the conductivity dependence on temperature.

Observing from Equation 2.14, some terms are constant, e. g., q, k, a_0 and the pre-factor γ are not expected to alter substantially from oxide to oxide. This leaves $[V_O^{\cdot\cdot}]$ and ΔE_a to mainly determine the level of ionic conductivity. Therefore, for a material to achieve high ionic conductivity, a large number of mobile oxygen vacancies must be present in the lattice, which can be achieved by non-stoichiometry, as for example by adding yttria to zirconia. The process can be illustrated by the following equation in Kröger-Vink notation:

$$Y_2O_3 \longrightarrow 2\, Y_{Zr}^{'} + 3\, O_O^x + V_O^{\cdot\cdot} \tag{2.16}$$

The two lower valence Y^{3+} ions occupy the Zr^{4+} sites ($Y_{Zr}^{'}$) and one oxygen vacancy is introduced into the lattice ($V_O^{\cdot\cdot}$) to provide charge balance, illustrated in Figure 2.5. The resulting electroneutrality condition $[Y_{Zr}^{'}] = 2[V_O^{\cdot\cdot}]$ makes it clear that the conductivity is proportional to the degree of substitution in the dilute regime.

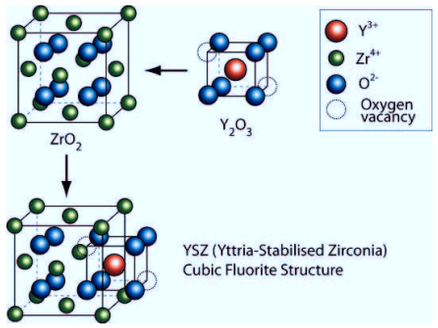

Figure 2.5: Oxygen vacancy formed due to the substitution of ZrO_2 by Y_2O_3 [47]

So far, what has been introduced is the oxygen ion transport in the lattice. However, oxide conductors in practical applications are mostly polycrystalline materials, which adds the influence of grain boundaries to be considered. A polycrystalline ceramic can be ideally assumed to consist of cube-shaped grains and flat layered grain boundaries, illustrated in Figure 2.6. According to the space-charge theory, the electrical potential of the grain boundary (or space-charge layer) is negative, which causes dopant segregation and $V_O^{\cdot\cdot}$ depletion in the space-charge layers, as shown in Figure 2.6. Therefore, due to the $V_O^{\cdot\cdot}$ depletion near the space-charge layers, the grain-boundary resistance is high [48, 49]. In addition to that, the disordered structure of the grain-boundary interface causes an accumulation of less conducting secondary phase within the ceramics. Therefore, the above mentioned features of the grain boundary result in a higher resistance for the ionic conduction compared to the grain.

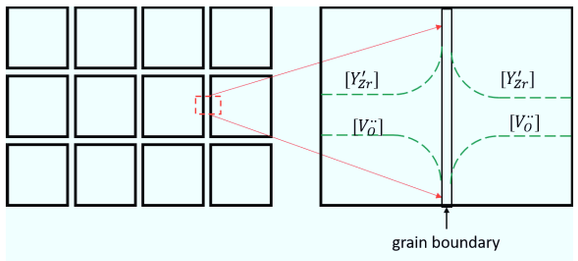

Figure 2.6: Left: Brick layer model of a polycrystalline material. Right: enlarged grain boundary with defect and oxygen vacancy concentration distributions (in green dash line)

2.2.3 *Materials*

Many materials with fluorite, perovskite, apatite, and related structures can be considered as electrolyte materials for SOFC. Among these structures, the most thoroughly investigated are fluorite-type oxides (AO_2) such as zirconia and ceria [18, 50, 51].

2.2.3.1 *Doped ZrO_2*

Pure zirconia exhibits three crystal structures at different temperatures: monoclinic structure at room temperature; tetragonal structure above 1170 °C; and a cubic fluorite structure above 2370 °C. Among all these structures, the high temperature cubic structure has the highest ionic conductivity [18, 52]. Replacing partial Zr^{4+} with a small amount of acceptor dopant cations, for example, yttria [53] or scandium [54], the high conductivity cubic structure can be stabilized to room temperature.

Among the zirconia electrolyte materials, yttria-stabilized zirconia (YSZ) is the most frequently used and investigated SOFC electrolyte. The doping of yttria not only stabilizes the cubic structure of zirconia, but also introduces oxygen vacancies (as illustrated in Equation 2.16). It is reported that the ionic conductivity of YSZ depends on the yttria content: the conductivity increases with the increase of the yttria content of up to a range of 8–11 mol % but then decreases for higher yttria contents [55]. The conductivity decrease with yttria content higher than 11 mol % is believed to relate to the agglomeration of oxygen vacancies, which leads to a reduction in defect mobility and thus conductivity [45] decreases. Moreover, YSZ is characterized by good chemical and mechanical stability with high quality raw materials available as well as pure ionic conductivity [9]. However, the operation of YSZ at temperature below 700 °C is highly challenging due to the significantly increased resistance [4, 56].

Another zirconia electrolyte, ScSZ, is also quite popular as it shows a higher ionic conductivity than YSZ. The higher conductivity is due to the smaller mismatch in size between Zr^{4+} and Sc^{3+}, as compared to that between Zr^{4+} and Y^{3+}, leading to a smaller energy for defect formation, which increases mobility and thus conductivity [54]. However, the activation energy for ionic conduction in ScSZ tends to increase with decreasing temperature, such that the conductivity of ScSZ is similar or even lower than that of YSZ below 500 °C, consistent with the observed increase in the migration energy of co-doped zirconia at 380–560 °C when yttria is replaced with scandium [57]. Another main issue for the use of ScSZ as electrolyte for SOFC is its phase instability. Similar to YSZ, there are also four main phases for ScSZ, monoclinic, tetragonal, rhombohedral and cubic [58]. Among the four main phases, the cubic phase (α) is known to have the highest ionic conductivity and is thus suitable for being used as a solid electrolyte for SOFCs. The α phase is indeed the main phase for a doping of Sc_2O_3 with 8–12 mol %. However,

it is not stable at temperatures below 650 °C, which has been the cause of an observed abrupt decrease in ionic conductivity during cooling [59, 60]. Moreover, some aging effects are observed at high temperatures (700–1000 °C) due to the local ordering effect towards the formation of tetragonal phase in the cubic matrix [61]. Many researchers have proposed various dopants like CeO_2, Sm_2O_3, Yb_2O_3, and Al_2O_3[54, 58, 62] to alleviate or prevent such an undesirable phase transition from α phase to the lower rhombohedral or tetragonal phase. According to Arachi et al.'s study [62], the stabilizing mechanism could be that the larger tetravalent dopant cation normally forms eight-fold coordination with oxygen, leaving oxygen vacancies to the Zr ion, which is mostly effective in stabilizing the high conductive α phase.

2.2.3.2 *Doped CeO_2*

Electrolytes based on ceria (CeO_2) have been suggested as alternative electrolytes to doped zirconia for low-temperature SOFCs [63]. Ceria possesses the same fluorite structure as stabilized zirconia but keeps the cubic structure over the whole temperature range from room temperature to the melting point. Similar to zirconia, the oxygen vacancies in ceria are introduced by substituting Ce^{4+} with trivalent rare earth ions, such as Gd^{3+}, Sm^{3+} and Y^{3+} [64]. The maximum conductivity occurs for the dopants Sm^{3+} and Gd^{3+}, which has the smallest ionic radius mismatch with Ce^{4+}, though there exists scatter in the conductivity values for these two kinds of dopants even for the same dopant content ($Ce_{0.8}Sm_{0.2}O_{1.9}$ and $Ce_{0.8}Gd_{0.2}O_{1.9}$) [64].

The gadolinium doped ceria (GDC) has been widely used as an electrolyte in SOFC due to its high ionic conductivity. Low ohmic resistance of a GDC electrolyte for SOFC has been reported by many researchers at low temperature. For example, Xia and Liu [65] reported an ohmic resistance of $0.67\,\Omega\,cm^2$ for 26 µm GDC electrolyte at 500 °C. Similarly, a 30 µm GDC electrolyte with $0.7\,\Omega\,cm^2$ at the same temperature was also reported by Doshi et al. [66] and $0.306\,\Omega\,cm^2$ for 20 µm GDC electrolyte reported by Zha et al. [67]. In addition to the low resistance, the better material compatibility with Sr containing cathodes, such as the state-of-the-art cathode material LSC and LSCF, makes GDC a better electrolyte than YSZ in terms of the compatibility with cathode [11, 68].

However, a second phase with high resistance is easily formed between GDC and YSZ [11, 69–71] at high co-sintering temperature (> ~ 1200 °C). Therefore, GDC can not be fabricated on the state-of-the-art NiO/YSZ anode by conventional powder processing methods, like tape casting or screen printing, because of the high temperature required for sintering. Another issue for using GDC as electrolyte is the reduction behavior of Ce^{4+} under reducing atmosphere. Two problems are caused by such behavior: first, the chemical expansion and the stress generated could cause mechanical failure of the electrolyte [63, 64]; second, the

current leakage due to the electronic charge carriers induced by the reduction, which decreases the cell performance [72, 73]. It is reported that the degree of reduction depends on the temperature and oxygen partial pressure (p_{O_2}) [63, 64, 74]. However, there is some disagreement regarding the temperature range for which there is no reduction. For example, Atkinson did some mathematical analysis and suggested that the maximum "safe" operation temperature for GDC should not exceed 750 °C [75]. On the other hand, Arachi et al. [62] reported that at 600 °C, no obvious expansion of GDC could be observed, indicating no obvious reduction of GDC only exists at temperature below 600 °C. Kudo and Obayashi [76] found that the content of dopant ($Ce_{1-y}Gd_yO_{2-y/2}$) affects the reduction behavior of Ce^{4+}, with higher dopant the less possible to be reduced. For example, at 700 °C, when y is increased from 0.1 to 0.2, the p_{O_2} is decreased from 1.3×10^{-17} atm to 1.24×10^{-19}. This could be explained by the fact that the oxygen vacancy concentration increases with the increase of dopant concentration, which in turn could suppress the reduction [64].

2.2.3.3 *Doped $LaGaO_3$*

In addition to the fluorite-structure electrolytes, doped $LaGaO_3$ with perovskite structure is also potentially attractive for application as electrolyte for LT-SOFC [77, 78]. By substitution of lower valence cations on La site, oxygen vacancies are introduced in order to maintain electrical neutrality, increasing the ionic conductivity, in a similar way to that shown for the vacancy formed mechanism for ZrO_2 and CeO_2. Also, the conductivity depends strongly on the particular alkaline earth cation placed onto the La site and increases in the order Sr>Ba>Ca. Therefore, strontium appears to be the most suitable dopant for $LaGaO_3$. However, there is a limited solubility of Sr on the La site and second phases is formed when the Sr content is higher than 10 mol % [77]. In addition to the substitution of La site, partial substitution of Ga site can also increase the ionic conductivity substantially, for example, reaching a composition maximum with 20 mol % Mg doping on the Ga site. At the same time, Sr solubility can be increased up to 20 mol % due to the enlarged crystal lattice induced by the larger ionic radius of Mg (compared to that of Ga) [79]. Ishihara et al. [80] reported that the highest ion conductivity in these oxides could be obtained with the composition $La_{0.8}Sr_{0.2}Ga_{0.8}Mg_{0.2}O_3$ (LSGM).

The conductivity of LSGM is higher than the YSZ and ScSZ but similar or lower than that of GDC [81]. Unlike GDC, LSGM does not show chemical reduction, it is thereby seems to be suitable for use in low oxygen partial pressure. However, problematic issues with LSGM relate to gallium evaporation under reducing atmosphere [8, 82], long-term mechanical stability with a high creep rate when compared to YSZ [83], difficulties in thin films processing [84], and the poor material compatibility with nickel [85]. Though LSGM has been demonstrated

to show better performance (due to the higher conductivity) than YSZ of equal thickness, LSGM poses difficulties in processing films as thin as other materials. This means that very thin GDC could outperform a thick LSGM at low operation temperature.

2.2.3.4 *Doped δ-Bi_2O_3*

The bismuth oxide system exhibits high oxide ion conductivity and has been proposed as a good electrolyte for SOFC. Four structures of Bi_2O_3 have been reported in the literature: the monoclinic α phase, the fluorite δ phase (fcc), the tetragonal β phase, and cubic γ phase (bcc) [86]. Among these four structures as well as the other known solid-state ion conductors, δ-Bi_2O_3 has the highest ionic conductivity [5, 86], for example, around $1\,S\,cm^{-1}$ at 700 °C [87]. The relatively high ionic conductivity of δ-Bi_2O_3 is due to the high oxygen vacancy concentration (nearly 1/4 of the oxygen sites are vacant); the high oxide mobility (caused by the high polarizability of the Bi^{3+} with its "lone pair" of electrons); and the highly disordered state (caused by Bi^{3+}) [88]. However, δ-Bi_2O_3 is not stable and transforms to α-Bi_2O_3 on cooling below 1000 K, and as a result the conductivity drops more than three orders of magnitude [88, 89]. Like zirconia, an effective way to stabilize the high temperature δ-Bi_2O_3 to room temperature can also be realized by doping with rare-earth dopants (such as Y, Dy or Er) and their combination with higher valence cations, such as W or Nb [86, 88, 90, 91]. For example, after doping with Er, at 500 °C, the ionic conductivity of $Er_{0.4}Bi_{1.6}O_3$ (ESB) is more than 2 orders of magnitude higher than GDC ($Gd_{0.1}Ce_{0.9}O_{1.95}$) and 4 orders of magnitude higher than YSZ ($Y_{0.148}Zr_{0.852}O_{1.926}$) [5]. However, the doped δ-Bi_2O_3 is thermodynamically stable only under high oxygen partial pressure. Therefore, a double layer electrolyte is commonly applied to protect doped δ-Bi_2O_3 from the reducing atmosphere. For example, Wachsman et al. [92] proved that using a bi-layer electrolyte consisting of GDC (on the fuel side) and ESB (on the air side) could prevent ESB from decomposing. But the strategy is quite challenging for two reasons. First, the relative thickness ratio between GDC and ESB has to be delicately controlled according to their report. Second, the additional decrease of ohmic resistance for bi-layer GDC and ESB with corresponding thickness of 10 µm and 4 µm at 650 °C ($0.046\,\Omega\,cm^2$), compared to that for single GDC with 10 µm ($0.062\,\Omega\,cm^2$), [93], has to be weighed against the increased processing cost. Such strategy is also quite doubtful that increasing an additional layer could decrease the ohmic resistance, not to mention that there is more room left for decreasing the thickness of GDC to decrease its resistance.

2.3 THIN ELECTROLYTE FILM FABRICATION TECHNIQUES

A common criteria to evaluate the performance of the electrolyte in SOFC is its resistance, R, during operation, which evaluates the electrolyte in terms of geometry, with thickness of l and area of A, and conductivity:

$$R = \frac{l}{\sigma A} \tag{2.17}$$

It is obvious from Equation 2.17 that the options to decrease R is either to use a material with higher ionic conductivity, which can be addressed by materials science indicated from previous section, or minimizing the thickness l and maximizing the area A of the electrolyte, which is related to the processing techniques. Therefore, another challenge for the electrolyte of SOFC, more specifically, anode-supported SOFC (AS-SOFC), is the fabrication of a thin and large-scale electrolyte membrane. Therefore, methods to fabricate thin electrolyte layer are introduced in the following.

2.3.1 *Ceramic powder processing*

2.3.1.1 *Screen printing*

Screen printing is a low-cost route for ceramic film processing, quite suitable for the fabrication of large-area, thin and flat ceramic layers (with a thickness range from a few µm to a few tens of µm). For screen printing, a paste (also called ink or slurry) has to be prepared first with acceptable rheological properties, e. g., viscosity, yield stress and viscoelastic properties. These properties depend on many factors such as the particle size distribution of the powder [94, 95], solid content [96], and the composition of the binder, dispersant, and solvent [97, 98]. For example, excessive amounts of binder might result in: increased tackiness of the paste, which in turn affects the printability and quality of the film; not enough density of the electrolyte, which is due to the burn out of the excessive binder. On the other hand, an insufficient binder content reduces the particle network strength within the paste, which could cause film cracking during drying. Similarly, increasing solid content increases the viscosity of the paste, while too little solid content leads to the cracking of the film. Therefore, due to the density requirement of the electrolyte, as little binder but as much solid content as possible is normally required. However, the maximum solid content is determined by the particle size distribution and specific surface area of the powder for a given solvent. For example, Mücke et al. [99] reported that the maximum solid content can be increased from 50 wt.% to 65 wt.% by pre-calcining the powder to increase the particle size (the d_{50} is increased from 0.25 µm to 0.44 µm). Besides, the quality of film can also be affected by the processing parameters, like the screen

options (e. g., dimension, thickness), substrate, screen printer settings (e. g., squeegee speed and load).

2.3.1.2 *Tape casting*

Tape casting is widely used to form thin ceramic films, with thickness from a few micrometers to a few millimeters, for SOFC. As illustrated in Figure 2.7, the underlying principle of tape casting is that a reservoir of slurry with a slit-shaped outlet at the base is moved across a surface, producing a layer of slurry. By adjusting the height and the speed of the movement of the blade as well as the characteristics of the slurry (composition, viscosity), the thickness of the layer can be adjusted [100]. Similar to screen printing, the slurry composition is the most crucial factor in tape casting. Generally, the slurry also consists of a mixture of powder and organics. The organics are usually the solvent, binder, dispersant agent, and plasticizer. The sintering behavior and final structures of the tape-cast layer depend mainly on the composition of the slurry, such as the particle size distribution of the powder, content ratio between the powder and the organics. Therefore, the slurry is usually fine-tuned to adjust the desired microstructure from highly porous to fully dense. The remaining organics in the tape-cast layer can be removed with subsequent heat treatment.

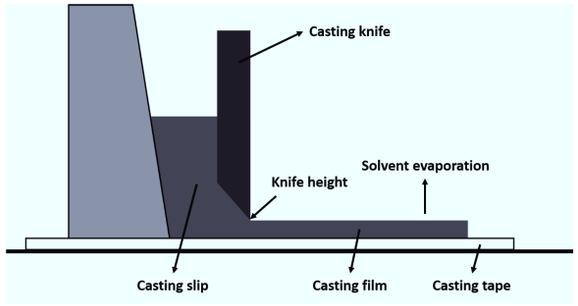

Figure 2.7: Scheme of tape casting process

2.3.2 *Sol-gel processing*

2.3.2.1 *Spin coating*

Spin coating is a very simple method for fabricating a thin film on a substrate. For example, Han et al. [38] used spin coating to fabricate a YSZ electrolyte as thin as 1 µm; Oh et al. [101] used the same method to obtain a bi-layer electrolyte with YSZ of 100 nm and GDC of 400 nm. The spin-coating process is performed in four steps: deposition, spin up, spin off and evaporation, as shown in Figure 2.8. Starting from the deposition of sol onto the substrate (stage i), the substrate is subsequently

accelerated to a defined speed and the sol is distributed homogeneously via centrifugal force (stage ii). Next, the excessive solvent is flung off the substrate surface when it rotates at high speed (800–2000 rpm) and the flow of the sol is ceased when enough sol has been removed and as a result the viscosity increased to a high level (stage iii). For the final evaporation process, further solvent is evaporated into the air (stage iv). Uniform evaporation of the solvent is possible because of rapid rotation and the high spinning speed results in thinning of the layer. Normally, after the evaporation stage, a low temperature baking is still required to evaporate the residual solvent. The quality and thickness of the thin coating layer depend mainly on the spinning speed [102], solvent evaporation rate [103, 104], viscosity or concentration of the polymer solution [105], and surface characteristics of the support [106].

However, one of the main disadvantages of spin coating a thin electrolyte for SOFC is the time consuming feature. Usually, multiple repeated spin coating and baking processes are needed to obtain the desired thickness of the electrolyte [38, 101]. Another disadvantage of spin coating is the size limitation of the substrate: the high-speed spinning process becomes more difficult as the substrate size increases [107].

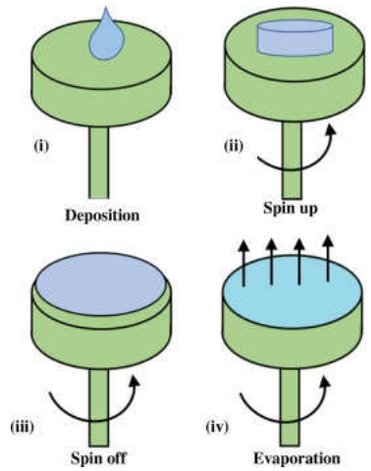

Figure 2.8: Stages of spin coating on substrate [107]

2.3.2.2 *Dip coating*

Dip coating is also a simple, low-cost, reproducible process to produce a thin film. The deposition of a thin film is realized by immersion of the substrate into a solution and as a result a homogeneous layer is formed on the surface of the substrate after withdrawing the substrate from the solution. That means dip coating is especially suitable for

producing a thin electrolyte film on substrates in flat geometries [108, 109]. Neacşu et al. [110] summarized the dip coating process into four steps (illustrated in Figure 2.9). First, immersion, at a constant speed, the substrate is dipped into the coating solution. Second, startup, the substrate remains in the solution for a designated time, and then be pulled out. Third, deposition, when the substrate is being pulled out, a thin film coating is being deposited on it and the thickness of the coating depends on the pulling out speed of the substrate. Final step, evaporation, the solvent starts to evaporate from the surface of the substrate to form a thin film.

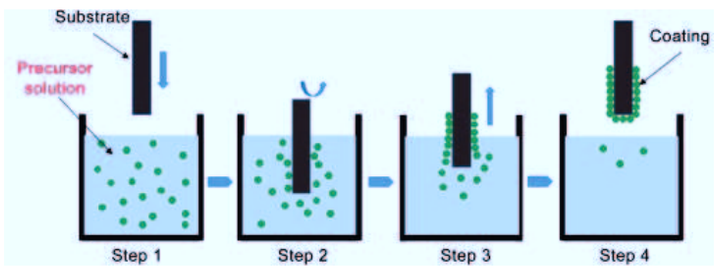

Figure 2.9: Graphical representation of dip-coating technique [110]

2.3.3 *Physical vapor deposition*

Physical vapor deposition (PVD) is a thin film fabrication process in which deposited film is formed by atom cluster, which are ejected from a solid target material by laser or a bombardment of energetic gas ions (such as Argon), impinging on the substrate. PVD technologies have attracted high interest in the manufacturing of ceramic high-temperature SOFC due to their ability to fabricate thin and dense ceramic films at low substrate temperatures compared to conventional ceramic powder processing methods [111, 112]. For example, a ceria barrier layer is needed between YSZ electrolyte and Sr containing cathode to prevent Sr diffusion from the cathode to the zirconia electrolyte. Such ceria barrier layer needs to be: thin to decrease resistance; dense to prevent reaction between cathode and zirconia electrolyte; able to be processed at low temperature (less than 1200 °C [10, 11]) to avoid the inter-diffusion between the ceria and zirconia layer. The ceria barrier layer fabricated by PVD has been demonstrated to fulfill all these requirements. In addition to the GDC barrier layer, Nédélec et al. [113] reported a 1 µm dense YSZ electrolyte by PVD and Uhlenbruck et al. [114] reported the fabrication of all the anode, electrolyte, cathode layers by PVD.

However, one prerequisite for a dense electrolyte by PVD deposition is that the substrate has an appropriate surface morphology, e. g., adapted roughness, sufficiently small surface pore size and in general no large

defects. For example, Haydn et al. [115] reported that the PVD deposited electrolyte (around 4–5 µm thick) on the anode with finer grain size and less porosity is more dense (lower gas leakage rate) and homogeneous than the anode with coarse and more porous microstructure. That means the application of PVD to fabricate electrolyte on industrial-scale anode might be challenging if the anode has a poor surface quality.

2.4 LOW TEMPERATURE SOFC

SOFC running at high temperature (850–1000 °C) can achieve high efficiencies, especially when combining it with a gas turbine (up to 70 % [6]). The Siemens-Westinghouse tubular system provides a good example for that [116]. However, for smaller units that are not intended to be coupled to a turbine, like some small scale CHP applications, auxiliary power unit (APU) and portable devices, it is better to lower the temperature as that could allow a broader choice of materials (for example, the use of cheap stainless steel for the bioplar plates and the balance of the plant) [63], quick start-up and shut down time. However, the switch of SOFC from high temperature to low temperature (400–600 °C) puts much pressure on YSZ electrolyte that is commonly used for high temperature SOFC, as it has a significantly lower ionic conductivity at low temperature. Table 2.1 compares the ionic conductivity at 500 °C for some typical electrolyte materials discussed before and lists the required thickness by assuming a theoretical area specific resistance for electrolyte of $0.1\,\Omega\,cm^2$ (calculated according to Equation 2.17). From which we can see that only an YSZ electrolyte as thin as 1 µm allows its use at 500 °C. Though the previously discussed spin coating or PVD could enable an electrolyte with such thickness, however, spin coating is time consuming and PVD requires a high surface quality of the substrate. Therefore, using an electrolyte material with higher ionic conductivity than YSZ could decrease the fabrication challenge.

Table 2.1: Comparison of ionic conductivity values for different electrolyte materials at 500 °C (with calculated required thickness based on an $ASR_{el} = 0.1\,\Omega\,cm^2$)

Material	Conductivity ($S\,cm^{-1}$)	Thickness (µm)	Reference
YSZ	1.1×10^{-3}	1.1	[117]
DWSB	9.8×10^{-2}	98	[118]
GDC	6.3×10^{-3}	6.3	[23]
ScSZ	4.9×10^{-3}	4.9	[119]
LSGM	6.0×10^{-3}	6.0	[77]

However, as discussed above, a high ionic conductivity is not the only requirement for the material to serve as the electrolyte in SOFC.

Further properties such as chemical compatibility with electrodes or chemical stability under both oxidizing and reducing atmosphere also need to be considered. Although it is true that none of the previously discussed electrolyte materials meets all the requirements at once, the interest in YSZ, ScSZ and GDC is higher than other materials as they show a promising mix of those criteria.

Despite the fact that the electrical performance of YSZ, ScSZ and GDC has been broadly investigated [4, 55, 81, 120–123], the conductivity values presented in some widely circulated literature are scattered. For example, in the review article by Brett et al. [120], ScSZ has nearly the same ionic conductivity as GDC at 500 °C and even has a superior conductivity than GDC at temperatures lower than 500 °C, while the conductivity of both GDC and ScSZ are given as significantly larger than that of YSZ at all temperatures. In contrast to this, in review [4], ScSZ has a lower conductivity than GDC at temperature of 500 °C and below. Moreover, in this review [4], the conductivity of ScSZ is similar to that of YSZ at temperatures lower than 450 °C. On the other hand, Kumar et al. [119] suggest that ScSZ exhibits much higher oxygen-ion conductivity than YSZ, and thus has a potential to be utilized as an electrolyte for low temperature SOFC. Similar expression can also be seen in some other publications [124, 125]. Citing an overview article by Mahato et al.,[126] Thommy et al. state that "Gadolinium-doped ceria $Ce_{0.9}Gd_{0.1}O_{1.95}$ (GDC) appears as a good candidate for such an application since it presents at 600 °C the same level of conductivity as the benchmark electrolyte YSZ at 900 °C". This is a vast overstatement, but illustrates the false impressions that can arise from conflicting literature information. Even for the more frequently investigated intermediate or high temperature range (> 650 °C), there exists confusing data for the conductivity comparison, as shown in Table 2.2.

Table 2.2: Conductivity comparison for YSZ, ScSZ and GDC from different literature sources (data is approximated from plots in each reference)

Materials	Conductivity ($S\,cm^{-1}$)		Reference
	500 °C	700 °C	
YSZ	7.2×10^{-4}	8.4×10^{-3}	
ScSZ	9.6×10^{-3}	5.5×10^{-2}	[120]
GDC	8.8×10^{-3}	7.3×10^{-2}	
YSZ	8.2×10^{-4}		
ScSZ	1.6×10^{-3}		[4]
GDC	5.7×10^{-3}		
YSZ		3.0×10^{-2}	
ScSZ			[56]
GDC	5.9×10^{-3}	4.4×10^{-2}	
YSZ	9.1×10^{-4}	1.2×10^{-2}	
ScSZ			[121]
GDC	1.5×10^{-2}	7.4×10^{-2}	
YSZ	3.4×10^{-3}	5.5×10^{-3}	
ScSZ			[5]
GDC	7.8×10^{-3}	1.8×10^{-2}	

There are two points that need to be considered with regards to the conductivity presented in the aforementioned reviews. First, all of them use data referenced from other literature or reviews. For example, conductivity data from review [120] are referenced from review [127] and references therein. However, the conductivity data in review [127] are referenced to review [128], in which we cannot find the actual conductivity data. In much the same way, the data from review [4] are calculated from the center of the mass of the conductivity values from review [5] and [81]. This is, of course, a valid strategy when writing a review, but does present the danger of error propagation. Second, details about the property of the starting powders, the processing of the powders and the microstructure after sintering, which influence the ionic conductivity, are often missing in the aforementioned reviews and their referenced sources provided. For example, Mori et al. [129] investigated the effects of the morphology of the starting powders and found that $Sm_{0.2}Ce_{0.8}O_{1.9}$ sintered from round-shaped particle had higher conductivity than that sintered from elongated particles. Furthermore, Chen et al. [130] studied the effects of the sintering condition and found that YSZ sintered at 1350 °C for 4 h had a lower conductivity ($0.015\,S\,cm^{-1}$) compared to the one sintered at 1250 °C

for 8 h ($0.112\,S\,cm^{-1}$). Their explanation was the variation of relative density and grain size. Besides those effects, the level of impurities in the material is crucial, especially the content of SiO_2, which segregates to the grain boundary to cause a larger grain boundary resistance and imposes deleterious effects on the ionic conductivity [63, 131].

3 EXPERIMENTAL TECHNIQUES

This chapter briefly reviews the experimental techniques used in this work and lists the specific instruments.

3.1 MATERIAL CHARACTERIZATION

3.1.1 *Electrolyte materials*

The materials used are commercially available. Their composition and manufacturer information are summarized in Table 3.1.

Table 3.1: Summary of the powder information used

powder	composition	lot No.	manufacturer
YSZ	$(Y_2O_3)_{0.08}(ZrO_2)_{0.92}$	Z803541P	TOSOH, Japan
ScSZ	$(Sc_2O_3)_{0.1}(CeO_2)_{0.01}(ZrO_2)_{0.89}$	J2728	DKKK, Japan
GDC	$(Gd_2O_3)_{0.1}(CeO_2)_{0.9}$	CB080	Fuelcellmaterials, USA

3.1.2 *X-ray diffraction*

The room-temperature X-ray diffraction experiments were carried out using a D4 ENDEAVOR (Bruker AXS) with Cu-K_α radiation. The qualitative phase analysis of the diffraction patterns was carried out based on the powder diffraction file (PDF) database and the inorganic crystal structure database (ICSD) using the software package EVA (Bruker AXS). Quantitative phase analysis by means of Rietveld refinements was carried out with the software package Topas 4 (Bruker AXS).

The phase evolution of ScSZ during heating was investigated by in-situ high temperature XRD (HT-XRD) using an Empyrean R2020 diffractometer (PANalytical) with Cu-K_α radiation. The ScSZ powder was pressed into a pellet using a die with a diameter of 20 mm at a force of 15 kN. Diffraction patterns were collected at room temperature before and after each in-situ measurement. The in-situ measurements were performed at selected temperatures starting from a minimal temperature to a maximal temperature with a step size of 100 K/step. The heating ramp in between the steps was 5 K min^{-1}.

3.1.3 *Chemical analysis*

The impurity level for the raw YSZ, ScSZ and GDC powders was checked by inductively coupled plasma optical emission spectroscopy (ICP-OES) after dilution. For YSZ and ScSZ, around 50 mg of powder were weighted and heated with 2 g $(NH_4)_2SO_4$ and 4 ml of H_2SO_4 and then diluted (with distilled water) to 50 ml, while 50 mg GDC was dissolved into 1 ml HCl and 1 ml H_2O_2 and then diluted (with distilled water) to 50 ml. The samples were diluted in a ratio of 1:100 for measurement with a Thermo Scientific iCAP 7600 dual-view spectrometer. External calibration was performed with standards prepared by the dilution of Merck Certipur certified plasma emissions standards with diluted acids. The measurements were performed by using a radio frequency power of 1150 *W* and a cool gas flow of $12\,\mathrm{l\,min^{-1}}$, auxiliary gas flow of $0.5\,\mathrm{l\,min^{-1}}$ and nebulizer gas flow of $0.55\,\mathrm{l\,min^{-1}}$ for 10 s. Each solution was measured twice and the average result of three emission lines per element was used for quantification.

3.1.4 *Scanning electron microscopy*

The microstructure investigations were conducted by using scanning electron microscopy (SEM) (ZEISS ULTRA 55, Oberkochen, Germany) equipped with an energy-dispersive X-ray spectrometer (EDX) (Oxford X-Max, Oxford Instruments- Wiesbaden, Germany). For the SEM observation of powders, powders were dispersed in ethanol prior to observation, sonicated for 2 minutes, and then dropped on an polished aluminum sample holder and finally dried for observation. For the observation of grain boundaries on ceramic specimen, the sintered ceramic was first polished and then thermally etched by annealing 100 °C under the sintering temperature for 1 h. For the observation of different function layer in the cell, the sample was ground and polished prior to the check.

3.1.5 *Thermal analysis*

The dilatometry measurements were carried out with dilatometer 402C and 402E from Netzsch. The samples were prepared by pressing the powder into pellets of 8 mm in diameter and 10 mm in height before the dilatometry measurement. The measurement was performed from room temperature to a target temperature with a ramp of $5\,\mathrm{K\,min^{-1}}$, and then a dwell stage at the target temperature for 2 h.

Thermogravimetry (TG) measurement for the sintered full cell was carried out using a NETZSCH STA 449F1 in Ar/H_2 (2.9 %) atmosphere (forming gas). The measurement was done from room temperature to a target temperature: 500 °C, 600 °C, 700 °C and 800 °C, with a ramp of $5\,\mathrm{K\,min^{-1}}$ and then a dwell stage for different time.

3.1.6 *Archimedes characterization*

The relative density of the sintered ceramics ($\rho_{Material}$) was determined by "Archimedes methods", described by the following equation:

$$\rho_{Material} = \frac{m_1}{m_3 - m_2} \times \rho_{H_2O} \tag{3.1}$$

where m_1 is the weight of the dry specimen in the air, m_2 is the measured weight after completely immersing the ceramic into the water, m_3 is the measured weight of the ceramic after taking out of the water and ρ_{H_2O} is the density of the water.

3.1.7 *Particle size distribution*

The particle size distribution was checked by dynamic light scattering (DLC) using a laser particle size analyzer (LA950, Retsch). For data evaluation, the "Mie Theory" was applied. The refractive index used for the GDC powder is 2.2 and 1.48 for the terpineol solvent.

3.2 ELECTROCHEMICAL IMPEDANCE CHARACTERIZATION

3.2.1 *Basic principle*

The impedance is measured by applying a small excitation signal (could be voltage or current, here voltage is used for demonstration) to a system, expressed as a function of time:

$$E(t) = E_0 \sin(\omega t) \tag{3.2}$$

where $E(t)$ is the applied voltage at time t, E_0 is the amplitude and ω is the radial frequency as expressed by $\omega = 2\pi f$, where f is the frequency [132].

As the applied sinusoidal voltage is small (normally dozens of mV), the system can be treated as "pseudo-linear". Then, the current response is also a sinusoidal signal with same radial frequency ω but a shift in phase ϕ (ϕ = 0 for a purely resistive circuit) and different amplitude I_0, expressed as following:

$$I(t) = I_0 \sin(\omega t + \phi) \tag{3.3}$$

with Euler's relationship:

$$\exp(j\phi) = \cos\phi + j\sin\phi \tag{3.4}$$

the Equation 3.2 and Equation 3.3 can be changed to:

$$E(t) = E_0 \exp(j\omega t) \tag{3.5}$$

$$I(t) = I_0 \exp(j\omega t - \phi) \tag{3.6}$$

Similar to the Ohm's law, the impedance Z can be calculated as:

$$Z(\omega) = \frac{E}{I} = Z_0 \exp(j\phi) = Z_0(\cos\phi + j\sin\phi) \tag{3.7}$$

which can be plotted in a simple form as Figure 3.1a, with the imaginary part, Z'', against real part, Z'.

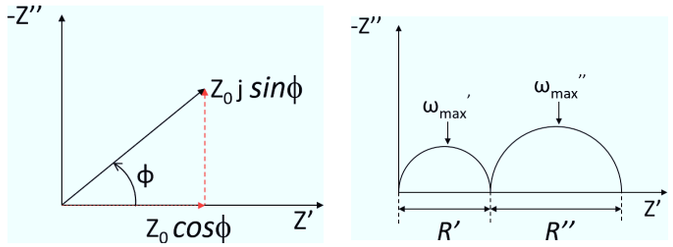

(a) Complex plane (b) Argand plot in semi-circle

Figure 3.1: Argand plot with impedance vector[133]

3.2.2 *Impedance analysis of oxygen ionic conductors*

The impedance spectroscopy of an ionic conductor, is typically in the form of two semi-circles in series, called "Argand plot" as seen in Figure 3.1b. Each of the semicircle can be interpreted as a circuit consisting of a resistor R and a capacitor C in parallel, and these two connected semi-circles can be seen as two "RC" components in series, like Figure 3.2.

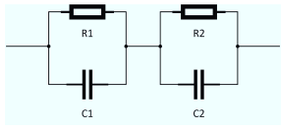

Figure 3.2: Two "RC" components in series

The reason is explained as following:
The impedance of a capacitor can be calculated as:

$$Z(\omega) = \frac{V(\omega)}{I(\omega)} = \frac{V_0 \cdot e^{j\omega t}}{\frac{dQ}{dt}} = \frac{V_0 \cdot e^{j\omega t}}{C\frac{dV}{dt}} = \frac{V_0 \cdot e^{j\omega t}}{C\frac{dV_0 \cdot e^{j\omega t}}{dt}} = \frac{1}{j\omega C} \tag{3.8}$$

Therefore, the total impedance of a "RC" in parallel is calculated as:

$$Z(\omega) = \frac{1}{1/R + j\omega C} = R\frac{1 - j\omega\tau}{1 + \omega^2\tau^2} \tag{3.9}$$

in which, τ, defined as characteristic time constant, is the product of R and C:

$$\tau = RC \tag{3.10}$$

If plotting Equation 3.9 in a complex plane, a semi-circle can be obtained. Furthermore, at the peak of each semi-circle, the following equation applies:

$$\omega\tau = 1 \tag{3.11}$$

where R can be obtained from the intercept of real axis according to previous discussion, ω is known from the given excitation signal of the impedance device. As discussed before, normally, for an ionic conductor, two semi-circles in series can be obtained, one is for the bulk region and the other is for the grain boundary region. The assignment of which semi-circle to which region is according to the magnitude of the C, in Table 3.2.

Table 3.2: Capacitance values and their possible interpretation[134]

capacitance [F]	Phenomenon Responsible
10^{-12}	bulk
10^{-11}	minor, second phase
10^{-11} – 10^{-8}	grain boundary
10^{-10} – 10^{-9}	bulk ferroelectric
10^{-9} – 10^{-7}	surface layer
10^{-7} – 10^{-5}	sample-electrode interface
10^{-4}	electrochemical reactions

Therefore, the resistance and capacitance for bulk (b) and grain boundary (gb) can be obtained from the impedance measurement, denoted as: R_b, R_{gb}, C_b, and C_{gb}. Then the grain conductivity (σ_b), grain boundary conductivity (σ_{gb}), and total conductivity (σ_{total}) is determined by:

$$\sigma_b = \frac{L}{R_b A} \tag{3.12}$$

$$\sigma_{gb} = \frac{C_b}{C_{gb}} \frac{L}{R_{gb} A} \tag{3.13}$$

$$\sigma_{total} = \frac{L}{(R_b + R_{gb}) A} \tag{3.14}$$

3.2.3 *Measurement procedure*

An impedance analyzer (Alpha-A High performance Frequency Analyzer, Novocontrol Technologies GmbH, Germany) with a frequency range from 0.1 Hz to 10 MHz was used to analyze the impedance. The dimension of the pellet used for EIS measurement was with thickness *L* around 3 mm and diameter *D* around ~ 10 mm after sintering. After

the samples were polished to remove possible impurities on the surface, a thin (around 15 nm) platinum layer was sputtered on both surfaces of the sintered pellets, followed by additional hand brushing of Pt paste to serve as electrodes. The samples with coated Pt paste were then fired to 900 °C for 2 h in air to provide good bonding between Pt electrode and ceramic samples. The impedance data were collected during the cooling process from 800 °C to room temperature with a dwell-time of 2 h at each measured temperature to reach thermal equilibrium. The impedance data were analyzed by using the software "Zview 3.2".

3.3 CELL FABRICATION

3.3.1 *Synthesis of screen printing paste*

The function, lot number and manufacturer of all chemicals and materials used for the synthesis of different screen printing pastes are listed in Table 3.3. The following subsections describe the synthesis procedure of each paste.

Table 3.3: The summary of chemicals used for the preparation of the screen printing paste

Chemicals	Function	Lot No.	Manufacturer
GDC-NPs	electrolyte	MKBW2345V	Sigma Aldrich, USA
GDC	electrolyte	CB080	Fuelcellmaterials, USA
NiO	anode	20507	Vogler, Netherlands
GDC	anode		Treibacher, Australia
LSC	cathode	-	in house synthesized
FX9086	dispersant	1023P32421	Nuosperse, UK
terpineol	solvent	BCBL0327V	Sigma Aldrich, USA
ethylcellulose	binder	200689	Sigma Aldrich, USA

3.3.1.1 *Anode paste*

The received GDC powder for anode paste was calcined at 1230 °C for 3 h (with a ramp rate of 3 K min^{-1}). The calcined powder was then milled for 40 h with a tumbling mixer (speed of 72 U/rpm) until a target particle size distribution was achieved ($d_{10} = 0.1 \pm 0.05\mu m$; $d_{50} = 0.3 \pm 0.10\mu m$; $d_{90} < 1.2 \pm 0.05\mu m$). Then the pre-treated powder was used for the anode paste synthesis. The process for synthesizing the screen printing paste for the anode layer is illustrated in Figure 3.3. A mixture of NiO powder (without pre-treatment), terpineol and dispersant with ratio (in wt.%) of: 72 : 27.14 : 0.86, was ball milled by a tumbling mixer for 24 h at a speed of 72 rpm to obtain a pre-suspension for NiO. Following the same recipe (except for the ball

milling time, 40 h), a GDC pre-suspension was obtained. Next, the GDC pre-suspension was mixed with NiO pre-suspension, in 50 wt.% : 50 wt.%, to get the NiO-GDC pre-suspension. In the following step, a transport agent (mixture of ethyl cellulose and terpineol in 15 wt.% : 85 wt.%) was added into the NiO-GDC pre-suspension and mixed in a planetary vacuum mixer (ARV-310, THINKY, Japan) at a speed of 1400 rpm for 2 min to get the anode paste.

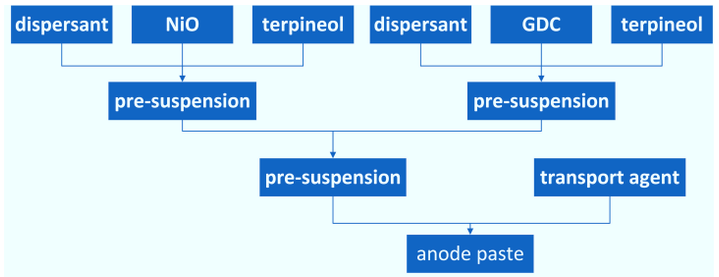

Figure 3.3: Process for the synthesis of screen printing paste for the anode layer

3.3.1.2 *Electrolyte paste*

The GDC powder for the electrolyte paste was used directly without pre-treatment. The process for synthesizing the screen printing paste for the electrolyte is illustrated in Figure 3.4. A solution mixture of GDC powder, terpineol and dispersant with ratio (in wt.%) of: 50 : 26 : 2, was mixed in a tumbling mixer for 24 h at a speed of 72 rpm to get the pre-suspension for GDC. In the following step, the same transport agent as used for the preparation for anode paste was added into the GDC pre-suspension and mixed in the planetary vacuum mixer at a speed of 1400 rpm for 2 min to get the electrolyte paste.

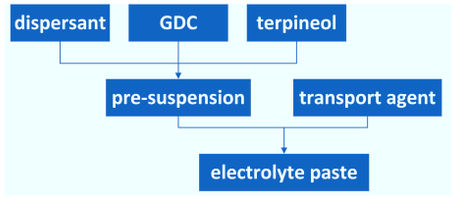

Figure 3.4: Process for the synthesis of screen printing paste for the electrolyte

3.3.1.3 *Cathode paste*

The process for synthesizing the screen printing paste for the cathode layer is illustrated in Figure 3.5. The in-house synthesized LSC powder was diluted into ethanol and ground into a specific particle size distribution ($d_{10} = 0.5 \pm 0.1\mu m$, $d_{50} = 0.8 \pm 0.1\mu m$, $d_{90} \geqslant 2\mu m$). Then the LSC solution was dried completely to evaporate the ethanol and then the dried powder was mixed with the transport agent (mixture of ethyl cellulose and terpineol in 94 wt.% : 6 wt.%) and terpineol in a ratio (in wt.%) of 62.75 : 20.85 : 16.40 using a three roll mill (80E, EXAKT) in multiple steps to destroy some loose LSC agglomerations and finally get a homogeneously mixed and fine LSC cathode paste. The gap between each roll for different rolling iterations are summarized in Table 3.4.

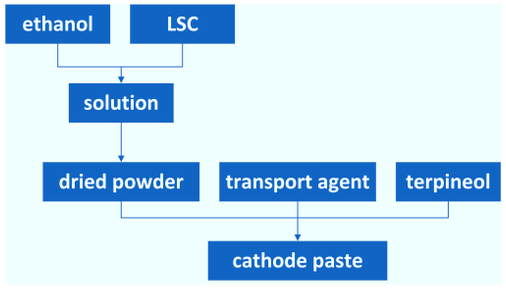

Figure 3.5: Process for the synthesis of screen printing paste for the cathode

Table 3.4: Processing parameters for three roll mixer

order	gap [1] (µm)	gap [2] (µm)
1	110	150
2	55	75
3	25	35
4	10	15

[1] the gap between the two rolls in the front
[2] the gap between the two rolls in the back

3.3.2 *Viscosity measurement*

The viscosity of the paste was tested with a rotational viscometer (MCR301, Anton Paar) with a cone plate (CP25-1-SN8497) at room temperature (20 °C). The working principle is illustrated in Figure 3.6. For the viscosity measurement of electrolyte and anode paste, the shear rate of the cone plate started from a low rate ($0.1\ s^{-1}$) to a high shear rate ($816\ s^{-1}$) and then slowed back from $816\ s^{-1}$ down to $0.1\ s^{-1}$. Such

measurement was repeated for two times (marked with the program ″2 × 816″) to simulate the actual screen printing process. Accordingly, a program named ″2 × 516″ was used for the viscosity measurement of the cathode paste.

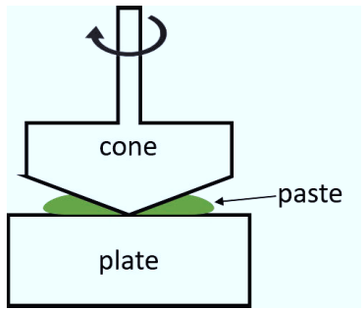

Figure 3.6: The scheme for a cone viscometer[135]

3.3.3 *Process of screen printing*

The scheme of the screen printing process is shown in Figure 3.7a. During the screen printing process, the paste is forced through the open mesh (frame) of a screen onto a substrate using a squeegee. Shown in Figure 3.7b is part of a semi-automated screen printer (E2, EKRA) that was used for this work. To ensure a good and homogeneous coverage, the screen printing process was performed twice. The information of the screen that used for different layers are summarized in Table 3.5. After screen printing, the sample was put into a drier at 60 °C for 20 min to completely evaporate the terpineol. For the final step, the dried sample was sent into an oven to do the heat treatment.

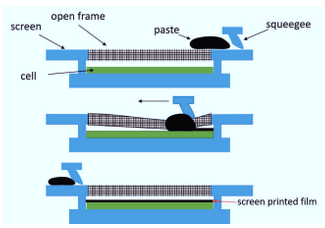

(a) Working scheme[136]

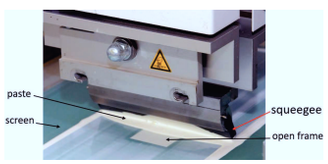

(b) Detail of screen printer used [137]

Figure 3.7: Screen printing

Table 3.5: The summary of information for the screen used as well as the wet layer thickness for different function layer

function layer	information for screen	WLT[1] (µm)
anode	V-screen 98–030–22.5°	26
electrolyte	V-screen 98–030–22.5°	26
cathode	POL-screen 18–180–22.5°	146

[1] WLT is short for wet layer thickness

3.3.4 *Thin GDC electrolyte on two different anode supports*

Two different anode supports were used for the thin GDC electrolyte development, compared in Figure 3.8, one of them used NiO-YSZ as anode layer (shown in Figure 3.8a) but the other one used NiO-GDC (Figure 3.8b). The anode support in Figure 3.8a was pre-sintered at 1300 °C to provide a good inter-connectivity for NiO. Nano-sized GDC (GDC-NPs) was used for the electrolyte to increase the sinter-ability (lower than 1200 °C) to avoid the chemical inter diffusion with YSZ. To reduce the number of sample, a non-shrinking YSZ substrate (company name, with thickness of 200 µm and diameter of 20 mm) was used to simulate the pre-sintered anode support. On the other hand, an actual anode support and micro-sized (or sub-micro-sized) GDC was used in Figure 3.8b.

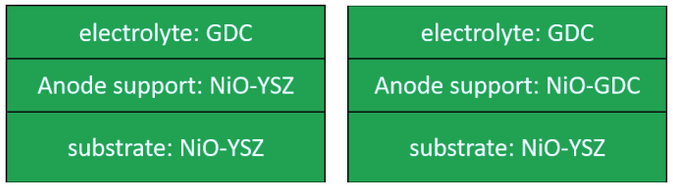

(a) on NiO/YSZ anode support (b) on NiO/GDC anode support

Figure 3.8: GDC electrolyte development on two different anode supports

3.3.5 *Leakage rate test*

The gas tightness of the electrolyte was checked by a home-made leakage measurement device as shown in Figure 3.9. The gas leakage measurement was done for the half cell (here the half cell means the ”fully dense” cell, consisting of substrate, anode function layer and electrolyte, after sintering at 1400 °C for 5 h) prior to the cathode coating. The electrolyte side faced downwards and substrate side faced upwards for the test. There are "O-ring" gaskets on both sides to ensure a good tightness of the device. The permeating gas in the vacuum side was

measured with a mass spectrometer and converted into the permeation rate ($hPa\,dm^3\,cm^{-2}\,s^{-1}$), which was normalized by the measured area and considered the typical pressure difference between cathode and anode (100 hPa) for an SOFC stack [99]. Since the anode functional layer could also be completely densified after sintering at 1400 °C for 5 h, the measured leakage rate after sintering could not completely represent the actual gas tightness of the electrolyte. Therefore, the leakage rate of the half cell after reducing (in which case, due to the reduction of NiO into Ni, the anode functional layer is porous) was also measured. The measured area was $4\,cm \times 4\,cm$. The internal threshold to determine if a cell is dense or not is summarized in Table 3.6.

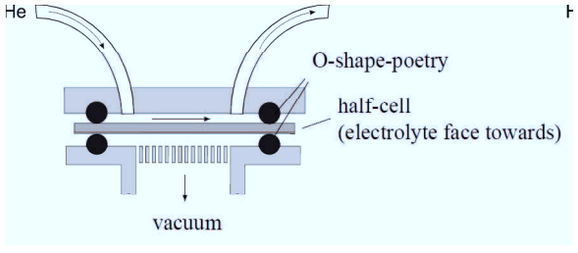

Figure 3.9: The leakage measurement scheme[138]

Table 3.6: Leakage rate ($hPa\,dm^3\,cm^{-2}\,s^{-1}$) threshold for JÜLICH cells

state	atmosphere	
	He	O_2
oxidized	2×10^{-5}	8×10^{-6}
reduced	2.3×10^{-4}	2×10^{-5}

3.3.6 *In-situ optical dilatometry*

The in-situ optical sintering of the half cell was characterized by a thermo-optical measurement system "Tommi Plus" [139]. Single image as well as time-lapsed video of the thermal treatment was obtained every minute.

3.3.7 *Fabrication of full cell*

The manufacturing process of the full cell is evolved from the standard JÜLICH anode-supported half cell fabrication (see the detail in [10, 140]) and described in Figure 3.10.

The JÜLICH type IIIb anode support (substrate) was prepared by tape casting using a slurry consisting of 44 wt.% NiO (Mallinckrodt Baker Inc., USA) and 56 wt.% 8YSZ (Imers, France). The tape-cast substrate was then heat treated at 1230 °C for 3 h and ended with a geometry of 60 mm × 60 mm × 0.5 mm.

Next, an anode layer with a finer microstructure was fabricated by screen printing of a paste, consisting of 50 wt.% NiO (same as that for the substrate) and 50 wt.% 20GDC (Treibacher, Australia), on top of the anode support and heat treated at 1000 °C for 1 h.

Then, an electrolyte layer was prepared by screen printing a paste, consisting of GDC, on top of the anode layer and heat treated at 1400 °C for 5 h to get a dense electrolyte. After this step, the co-sintered cell is called half-cell (anode support + anode function layer + electrolyte).

Following that, a thin YSZ layer was deposited on the surface of the electrolyte layer by electron-beam physical vapor deposition (EB-PVD) to act as the electron blocking layer. Subsequently, a thin GDC layer was additionally applied on top of the YSZ layer via bias-assisted magnetron sputtering to function as a barrier layer.

In the final step, the LSC paste was screen printed on the GDC barrier layer and sintered at 850 °C to function as the cathode layer.

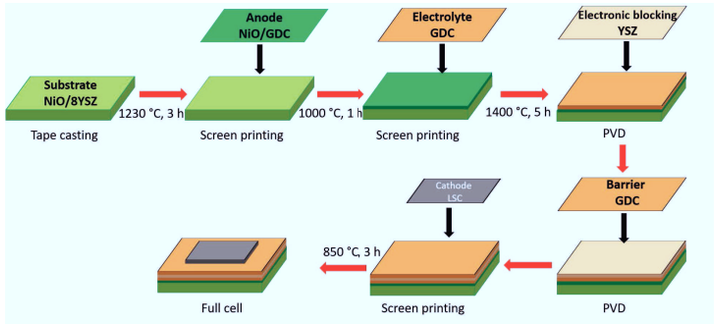

Figure 3.10: Manufacturing process of the full cell

Following the procedure in Figure 3.10, a final (sintered) full cell was fabricated with dimension of 5 cm × 5 cm × 0.5 mm, seen in Figure 3.11. The corresponding thickness for each function layer was around: 7 µm for the anode layer, 3.5 µm for the electrolyte, 600 nm for the electron blocking layer, 500 nm for the barrier layer and 20 µm for the cathode.

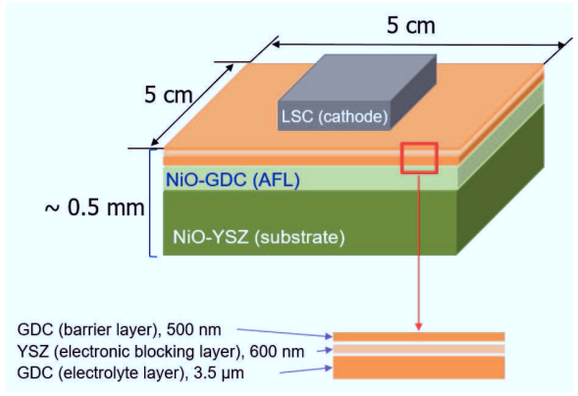

Figure 3.11: Schematic of full cell structure

3.4 SINGLE CELL PERFORMANCE TEST

The single cell performance test is not available in JÜLICH due to the problem of sealing cells at low temperature, therefore, the single cell performance test was conducted in different institutes as described below.

For the single cell test measured in China University of Mining and Technology, China (CMUT), the test was conducted in a home-developed experimental system using $40\,\mathrm{ml\,min^{-1}}$ humidified hydrogen (3 % H_2O) as the fuel and ambient air as the oxidant. IV curve and EIS were recorded using the electrochemistry workstation (IM6e, Zahner). The EIS was measured under open circuit in the frequency range of 0.1 Hz–10 MHz with the amplitude of 0.01 V [141]. Prior to the single cell test, the cell was reduced at 650 °C overnight.

For the single cell test measured in Korea Institute of Science and Technology, Korea (KIST), air and humidified H_2 (3 % H_2O) were used as the oxidant and fuel, respectively, flow rates of each were held constant at 200 sccm for the fuel cell operation. The cell operating temperature varied from 650 °C to 450 °C at interval of 50 °C. An Iviumstat electrochemical analyzer (Iviumstat, Ivium Technologies) was used to obtain the EIS and IV curves, and each EIS was observed over a frequency range from 0.1 Hz to 10 MHz. The AC amplitude of the impedance measurements was 50 mV [142]. Prior to the single cell test, the cell was reduced at 650 °C until a monitored OCV reached stabilization.

For the single cell test measured in the Institute of Applied Materials - Electrical and Electronic Engineering (IAM-WET) of Karlsruhe Institute of Technology, Germany (KIT), the details of the measurement setup are described by Timmermann et al. [143]. The sample used for the test had an active cathode area of $1\,\mathrm{cm} \times 1\,\mathrm{cm}$. The fuel gas flow and composition

was computer-controlled by digital mass flow controllers (MFC). On the cathode side, ambient air was used with a flow of 2.5×10^{-1} l min^{-1} (under standard conditions). On the anode side, different mole fraction of H_2 and O_2 were mixed according to desired humidity in the fuel. The total humidity was determined by measuring the electromotive force (EMF) in front of the electrode, since the humidity in the gas was increased through internal gas leakage. The cell was inserted in an Al_2O_3 housing for the test. Electrical contacts were applied on the cathode side by 2 point-welded gold meshes (net thickness 200 µm, 1024 meshes cm^{-2}). On the anode side, 2 point-welded Ni mesh (net thickness 200 µm, 900 meshes cm^{-2}, wire thickness 0.15 mm) were employed to ensure a homogeneous current distribution over the electrode. A contact weight of 1115 g ensured a reliable contacting. High-precision Al_2O_3 frames with thickness matching the thickness of the anode substrate was used on the anode side to ensure a good sealing against air. All the measurements were carried out script-controlled and automated, the cell voltage was determined by a four-point measurement under constant electrical load, the corresponding cell temperature was measured by thermocouples both in the cathode and anode. Before the experiment, the cell was first heated to 800 °C under dry and pure H_2 for complete reduction and then the cell voltage was measured from 800 °C to 400 °C with current density starting from 0 to 2 A cm^{-2}.

4 CHARACTERIZATION OF IONIC CONDUCTIVITY

In this chapter, the ionic conductivity characterization is discussed for YSZ, ScSZ and GDC. First, the powder properties are examined.Then, the microstructure after sintering the powder to ceramics is characterized. Following that, the grain, grain boundary and total conductivity is determined by EIS for each ceramic. After the analysis of EIS, a simple "brick-layer"model is introduced to predict the influence of the grain size of an electrolyte on its conductivity at 500 °C.

4.1 POWDER CHARACTERIZATION

The powder used for the ionic conductivity characterization were used directly without treatment, like calcining or ball milling.

4.1.1 *Impurity level*

The impurity levels of the three commercial powder were checked after receiving from manufacturer and compared in Table 4.1. The impurity level for each material confirmed that they are highly pure, especially with extremely low Si contents, which was reported to have detrimental effects on the grain boundary ionic conductivity[63, 131]. It can, therefore, be expected that the ionic conductivity of these three powders will not be affected by their impurity level.

Table 4.1: Impurity content in the commercial powder

Powder	Elements content (ppm)			
	Si	Co	Fe	Cu
YSZ	24±6	52±4	38±17	40±20
ScSZ	19±6	47.3±1.0	31±6	30±20
GDC	21±1.4	52±4	37±4	51.7±0.7

4.1.2 *Particle size distribution*

The PSD was checked, compared in Figure 4.1 and the detailed value are summarized in Table 4.2. Both Figure 4.1 and Table 4.2 shows that these three powders have similar particle size distribution, with d_{50} at

the same level. No obvious minor secondary peak was observed for all of the three powders, indicating there are no hard agglomerations.

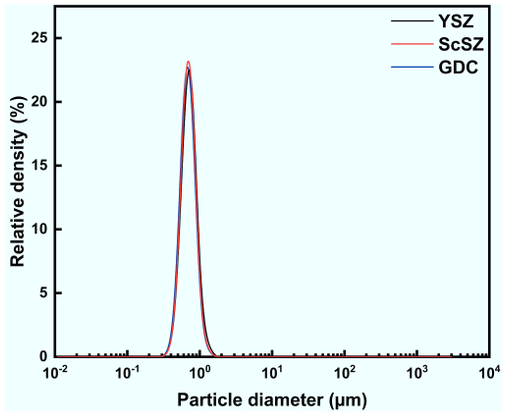

Figure 4.1: Particle size distribution for YSZ (black line), ScSZ (red line) and GDC (blue line) in relative density

Table 4.2: The summary of particle size distribution

powder	Particle size distribution (μm)		
	d_{10}	d_{50}	d_{90}
YSZ	0.493	0.664	0.886
ScSZ	0.488	0.648	0.859
GDC	0.474	0.635	0.851

However, because of the inherent limitations of the particle size distribution characterization (for instance, some particles may accumulated to loose agglomerations), we additionally checked the raw powder morphology by SEM, shown in Figure 4.2. YSZ powders were presented as soft agglomerates consisting of 40–70 nm crystalline particles (Figure 4.2a). Similarly, ScSZ powders were also presented as soft agglomerates but consisted with a little bigger particles with diameter of 40–100 nm (Figure 4.2b). However, GDC powders were presented as pre-sintered agglomerates, which consisted of smaller 20–100 nm crystalline particles (Figure 4.2c). Therefore, it could be expected that their sintering behavior might be different, especially for GDC compared to YSZ and ScSZ.

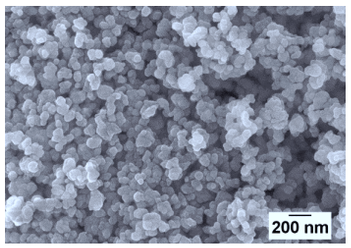

(a) YSZ

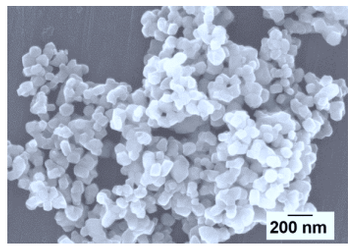

(b) ScSZ

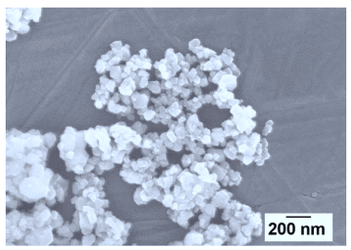

(c) GDC

Figure 4.2: Raw powder morphology observed by SEM

4.1.3 *Sintering behavior*

The sintering behavior of these three powders was checked by dilatometry, shown in Figure 4.3. All of these three powders showed a comparable one-step sintering behavior, mostly likely solid state sintering. On the other hand, YSZ and ScSZ showed a more active sintering behavior than GDC, they shrank faster and the shrinkage nearly finishes at 1300 °C with a heating rate of $3\,\mathrm{K\,min^{-1}}$ and finally could reach a maximum shrinkage around 22.5 % when held at 1400 °C for 2 h. GDC required higher sintering temperature (1400 °C), and its shrinkage only saturated when sintered at 1400 °C for 2 h, finally reaching a maximum around 15 %. The reason for that might be GDC already has a higher relative green density before sintering, 57.2 %, seen in Table 4.3. As a comparison, the relative green density for YSZ, ScSZ is 45.3 %, 43.6 %, respectively. All these values testify the high quality of the powders and their good sinterability. Therefore, based on the dilatometry measurement, a sintering temperature of 1400 °C for 2 h was chosen for all these powders.

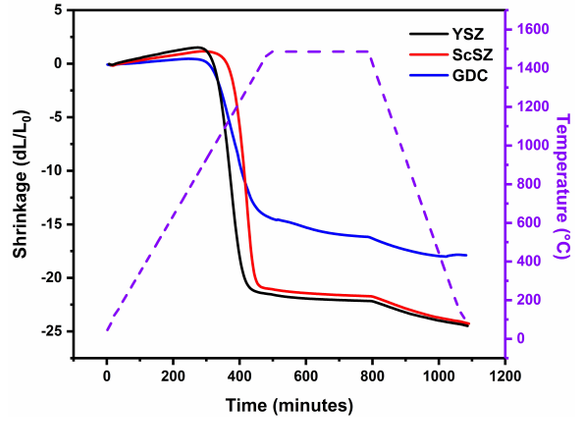

Figure 4.3: Dilatometry measurements for YSZ (black line), ScSZ (red line) and GDC (blue line)

Table 4.3: Comparison of relative green density and sintering density (after sintering at 1400 °C for 2 h) as well as the average grain size of the ceramics for YSZ, ScSZ and GDC

	YSZ	ScSZ	GDC
Relative green density (%)	45.3±0.3	43.6±0.4	57.2±0.7
Relative sintering density (%)	98.9±0.3	98.0±0.1	97.9±0.2
Average grain size (µm)	2.28±1.0	2.97±1.4	0.73±0.3

4.2 MICROSTRUCTURE OF SINTERED CERAMICS

4.2.1 *SEM cross-sectional observation*

Figure 4.4 shows the microstructure of polished and thermally etched (100 °C below the sintering temperature for 1 h) surfaces of the sintered ceramics observed by SEM. After sintering at 1400 °C for 2 h, all of the three ceramics reached a highly dense microstructure, higher than 95 % (seen in Table 4.3, measured by Archimedes method). Few defects, like pores, could be found between the grains. The dense microstructure for all of the three ceramics guarantee that their ionic conductivity will not be affected by the porosity. It was also observed that GDC had a smaller grain size distribution, compared to YSZ and ScSZ (this is also the reason for the higher magnification for GDC pellet seen in Figure 4.4c), indicating more grain boundary resistance for the GDC pellet. However, their detail average grain size will be analyzed in the following.

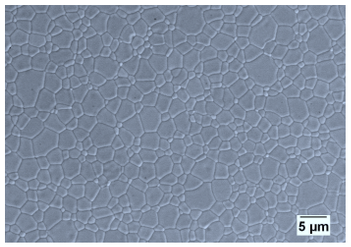

(a) YSZ

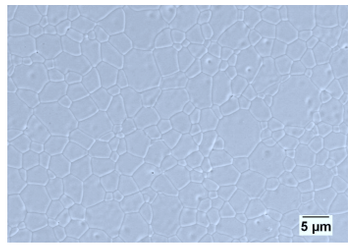

(b) ScSZ

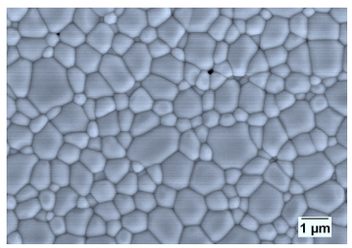

(c) GDC

Figure 4.4: SEM cross-sectional microstructure for sintered pellets

4.2.2 *Average grain size distribution*

Their grain size distribution (calculated from around 1500 grains), shown in Figure 4.5, and the average grain size are summarized in Table 4.3. As shown in Figure 4.5, GDC has a narrower grain size distribution compared to YSZ and ScSZ. In addition to that, GDC has a much

lower average grain size (0.73 µm) than that of either ScSZ (2.97 µm) or YSZ (2.28 µm). Therefore, in terms of total conductivity, GDC could have more contribution of grain boundary resistance compared to ScSZ and YSZ due to higher total thickness of grain boundaries. Furthermore, the highly dense microstructure shown here confirms that for all the three materials porosity will have negligible effects on the conductivity.

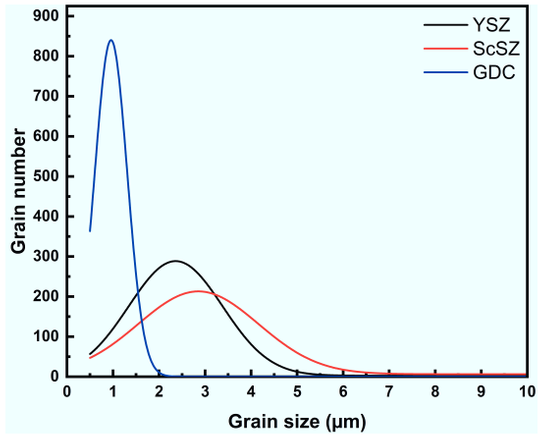

Figure 4.5: Grain size distribution for YSZ, ScSZ and GDC

4.3.1 *Temperature variation*

Figure 4.6 compares the dependence of electrochemical impedance spectroscopy (EIS) on temperature for YSZ. At 340 °C, seen in Figure 4.6a, the diagram consists of two semi-circles at high frequency (~ 600 kHz) and intermediate frequency (~ 13 kHz), with an inclined line at low frequency. According to their characteristics C, the first semi-circle is for the bulk resistance, R_b, and the second for the grain boundary resistance, R_{gb} while the low frequency line corresponds to the ion-blocking Pt electrodes. We can see that, at a higher temperature 440 °C, the high frequency semi-circle for the bulk gradually disappears. This is due to the fact that the characteristic frequency increases above the maximum measurement frequency of the frequency analyzer. While for higher temperature, 550 °C, no semi-circle could be observed as the ionic mobility at such higher temperature is high enough that the ionic charge carriers follow the voltage excitation instantaneously and no phase shift is detected in the investigated frequency range. For this condition, the intercept with the x-axis is attributed to the total resistance from bulk and grain boundary. The other two materials, ScSZ and GDC, have a similar trend of the IS dependence on temperature,

only the temperatures at which the semi-circles gradually disappear are slightly different.

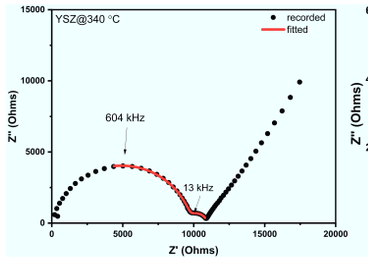

(a) 340 °C

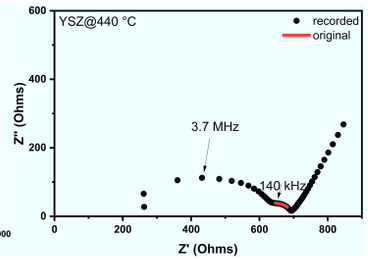

(b) 440 °C

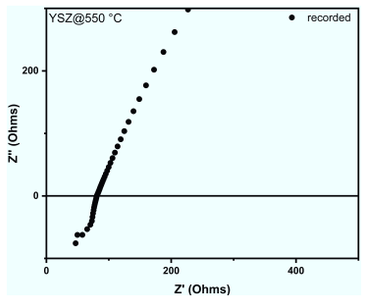

(c) 550 °C

Figure 4.6: Temperature dependence of the impedance spectroscopy for YSZ at three different temperatures

4.3.2 *Bulk and grain boundary conductivity*

Shown in Figure 4.7 is the comparison of EIS for YSZ, ScSZ and GDC at 300 °C. The original recorded EIS is shown as open symbols and the lines are the fitting results. The inset of Figure 4.7 shows the equivalent circuit that was used to fit the data. As we can see here, the circle is not an ideal semi-circle, therefore, a constant phase element (CPE) rather than the ideal capacitor element is used to fit the data.The two "$R-CPE$" represent the bulk and grain boundary contribution, respectively. Moreover, the exponential factor, α, 0.85–0.94, seen in Table 4.4, is also indicative of that as α should be 1 for pure capacitor [144]. The electrode response at low frequencies is excluded from the fit.

Accordingly, the respective pseudo-capacitance C for each semi-circuit is calculated from:

$$C = (R^{1-\alpha}Q)^{\frac{1}{\alpha}} \tag{4.1}$$

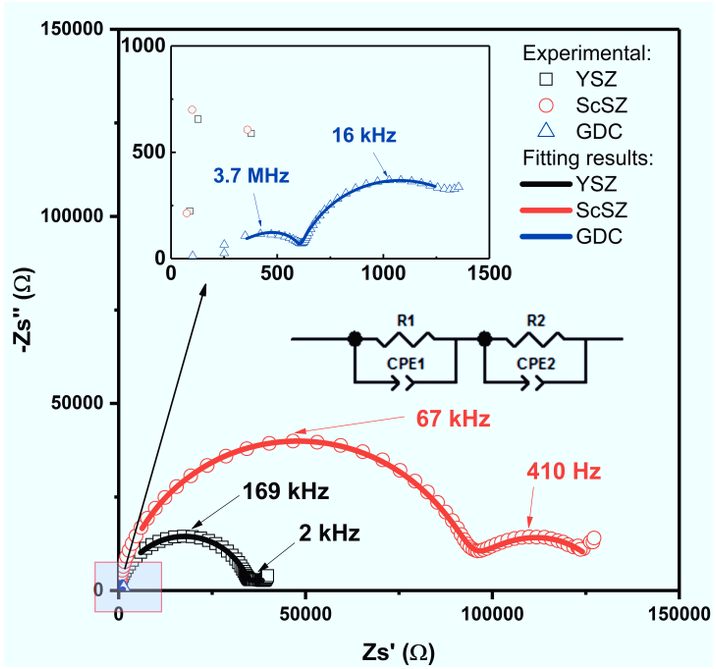

Figure 4.7: Typical impedance spectra of YSZ (black), ScSZ (red) and GDC (blue) at 300 °C. The experimental data are plotting in symbols and fitted data are plotting in lines

The fitted parameters are listed in Table 4.4.Based on the magnitude of capacitance C, the first semi-circle at high frequency is assigned to the bulk response and the second one to the grain boundary response. Accordingly, R_1, R_2, C_1 and C_2 are assigned to the resistance and capacitance for bulk and grain boundary as R_b, R_{gb}, C_b and C_{gb}, respectively. As seen in Table 4.4, the capacitance for C_1 are in the range of 25–40 pF while the stray capacitance of the setup is 5 pF. Therefore, the dielectric constants (or permittivity) ε_R (calculated from C_1 in the high frequency range and at 300 °C) for these three materials are provided for comparison with literature values. The ε_R values in this work are in good agreement with reported values. For example, for doped zirconia: Pimenov [145] (ε_R = 63 – 86, 329 °C, ZrO_2—4 mol % Y_2O_3), Aigars et al., [146] (ε_R= 53, 300 °C, ZrO_2—7.5 mol % Y_2O_3) Boulouz et al., [147] (ε_R = 65.7, 300 °C, ZrO_2—8 mol % Y_2O_3), Tao et al., [148] (ε_R = 71, 340 °C, ZrO_2—8 mol % Sc_2O_3), and for doped ceria by Yamamura et al., [149] (ε_R= 80 – 120, 300 °C, CeO_2—20 mol % Sm_2O_3), Baral et al., [150] (ε_R= 14 – 102, 400 °C, CeO_2—15 mol % Gd_2O_3), Nowick et al., [151] (ε_R = 25, 132.5 °C, 1 MHz, CeO_2—6 mol % Y_2O_3).

Table 4.4: The fitted parameters for YSZ, ScSZ and GDC at 300 °C

	R_1 [Ω]	R_2 [Ω]	Q_1 [F]	ε	Q_2 [F]	α_1	α_2
YSZ	39456	4954	1.49×10^{-10}	66.3	5.65×10^{-8}	0.87	0.91
ScSZ	95207	34356	1.13×10^{-10}	68.5	4.38×10^{-8}	0.88	0.85
GDC	608	763	1.22×10^{-10}	47.9	5.74×10^{-8}	0.94	0.86

The dependence of σ_b and σ_{gb} on temperature for YSZ, ScSZ and GDC is shown in Figure 4.8, in the form of Arrhenius equation:

$$\sigma T = \sigma_0 \exp(-\frac{E}{kT}) \tag{4.2}$$

where σ is the conductivity, can be σ_b, σ_{gb} or σ_{total}, T is the absolute temperature (K), σ_0 is the pre-factor of conductivity, E is the activation energy for ionic conduction, k is the Boltzmann constant.

For all three electrolyte materials, σ_b is always much higher than σ_{gb} at all measured temperatures, consistent with [131]. However, some investigations found that σ_{gb} is higher than σ_b for Sc-doped zirconia. Their proposed reason was that the observed semi-circle for grain boundary was smaller than that for the bulk in the recorded impedance spectroscopy, accordingly indicating $R_b > R_{gb}$ [119, 152]. That is incorrect since the specific thickness of grain boundary is much thinner than that of bulk and therefore a geometrical correction should be done for the σ_{gb} so that the σ_b is compared to the σ_{gb}.

The activation energy (E_a), slope of the linear fit in Figure 4.8, for the σ_b and σ_{gb} in the temperature range between 200 °C and 450 °C are listed in Table 4.5. For GDC and YSZ, E_a of the σ_{gb} is higher than that of the σ_b, which is consistent with other report [131]. However, for ScSZ, the E_a of σ_b is higher than that of the σ_{gb}, the reason for that is not clear yet.

Table 4.5: Activation energy of σ_b and σ_{gb} for YSZ, ScSZ and GDC

sample	Activation energy (*eV*)	
	Bulk	Grain boundary
YSZ	1.09 ± 0.002	1.18 ± 0.022
ScSZ	1.49 ± 0.011	1.40 ± 0.009
GDC	0.74 ± 0.005	0.91 ± 0.003

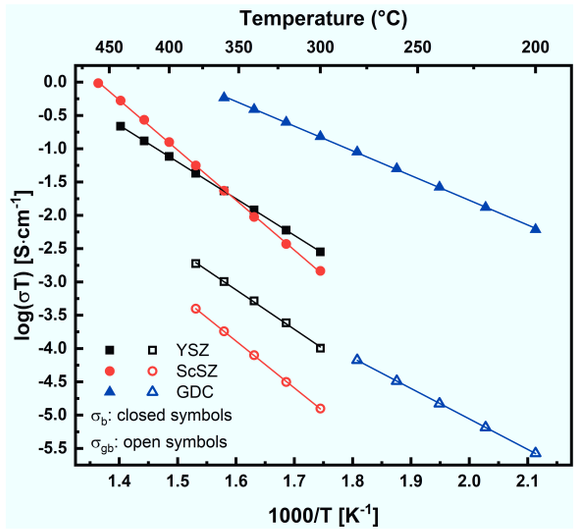

Figure 4.8: Dependence of σ_b and σ_{gb} on temperature for YSZ, ScSZ and GDC

4.3.3 *Total conductivity*

Figure 4.9 compares the σ_{total} of YSZ, ScSZ and GDC from 300 °C to 800 °C. It shows that the ionic conductivity of GDC is not always higher than that of the zirconates at all temperatures. The conductivity of GDC is nearly the same as that of ScSZ at 600 °C (17.6 mS cm^{-1} vs 15.7 mS cm^{-1}) and even lower than that of ScSZ at temperatures above 650 °C. At lower temperatures (< 600 °C), GDC shows a higher ionic conductivity than both zirconates. Regarding ScSZ, though it has the highest ionic conductivity at temperatures higher than 650 °C, its ionic conductivity decreases significantly when lowering the temperature and is even lower than that of YSZ at temperatures below 400 °C.

As indicated by the line shown in Figure 4.9, the dependence of σ_{total} on temperature for YSZ and GDC can both have a good linear fitting, in good agreement with the Equation 4.2. However, for ScSZ, the slope of the linear fitting line obviously changes with increasing temperature. We assume there might be a phase transformation from high ionic conducting phase to a low ionic conducting phase. Therefore, an in-situ high temperature XRD (HT-XRD) was done for ScSZ (sintered at 1400 °C for 2 h), shown in Figure 4.10. It could be observed that there were only peaks corresponding to α phase (the high ionic conducting cubic phase) from room temperature to 800 °C. As a comparison, Yarmolenko et al. [153] observed an obvious transformation of high ionic conducting phase α phase to low ionic conducting rhombohedral β phase and the β phase back to α phase from 300 °C to 500 °C. Therefore, we think there

is no phase transition detected by XRD in our investigated ScSZ ceramic and the changed E_a should not be caused by the phase transition.

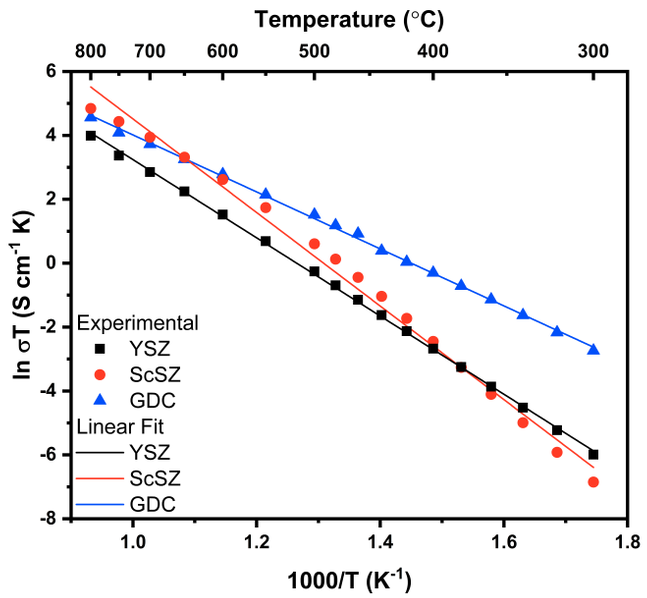

Figure 4.9: Comparison of experimental (denoted as symbol) and linear fit (as line) for YSZ (black), ScSZ (red) and GDC (blue)

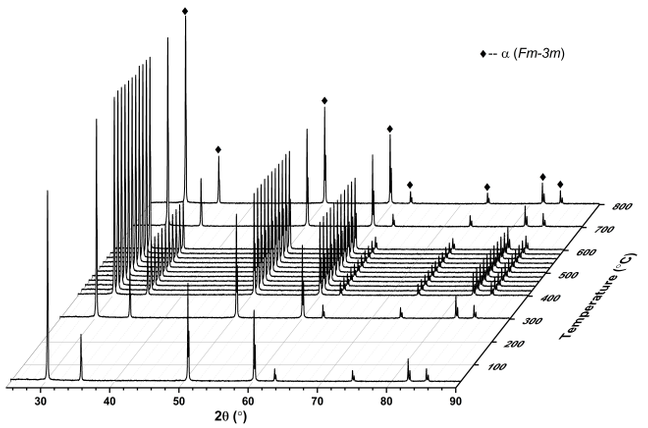

Figure 4.10: High temperature XRD of ScSZ measured from room temperature to high temperature

Recently, Ahamer et al. [144] provided an approach to explain the bending behavior of E_a. They suggested a "two barrier model" that assigns the bending in the Arrhenius plot to two parallel conduction pathways for oxygen vacancies with different barrier heights, which have to be passed along an average path of an oxygen vacancy. These different barrier heights refer to the fact that the potential energy landscape around an oxygen vacancy is strongly influenced by the amount of dopant ions around the vacancy site, and that the activation barrier will be different based on whether a start site or finish site of a jump is located next to Ce^{4+} ions or Gd^{3+} ions (in the case of GDC). This "two barrier model" can be presented in following equation:

$$\sigma T = \left(\frac{1}{\gamma_1 e^{-E_{a,1}/kT}} + \frac{1}{\gamma_2 e^{-E_{a,2}/kT}}\right)^{-1} \tag{4.3}$$

in which, $E_{a,1}$ and $E_{a,2}$ are the two barrier heights and γ_i equals to $\frac{z^2 {e_0}^2 {a_0}^2 n_{V,tot} \nu_i^0}{k\beta_i}$ (where z denotes the absolute charge of the vacancy, e_0 the elementary charge, a_0 the average jump distance, $n_{V,tot}$ the total vacancy concentration, ν_i^0 a pre-factor of the jump frequency, k is Boltzmann's constant and β_i a weight factor of successful jumps across barrier heights $E_{a,i}$). The two conduction pathways are in parallel, which means that appreciable differences in the activation energy of each pathway will lead to one or the other being dominant in a given temperature regime.

Therefore, we implement our experimental data of the the total conductivity, σ_{total}, and corresponding temperature, T in the Equation 4.3. The fitted parameters and results are shown in Table 4.6. As shown in Figure 4.11, our experimental data can be fitted very well using the "two barrier model". The $E_{a,1}$ represents the activation energy dominant at high temperature and $E_{a,2}$ represents the activation energy dominant at low temperature. At low temperature, ScSZ has a higher activation energy than YSZ, and therefore a lower ionic conductivity than YSZ at temperatures below 400 °C. On the other hand, GDC shows a lower activation energy than either YSZ or ScSZ for the whole temperature range. Accordingly, the increase in ionic conductivity with temperature is less pronounced than for the zirconates. For comparison, the activation energy obtained by fitting linearly using the Equation 4.2 (assuming there is only "one barrier" over the whole temperature range compared to the "two barrier model") is also included in Table 4.6. It is obvious that using one barrier model could bring higher error, especially at high temperature, where an error percent of 31.3 %, 54 % and 34.2 % happens for YSZ, ScSZ and GDC, respectively. Moreover, for materials like ScSZ, where a clearly observed bending in the Arrhenius plot, one barrier model could not describe the real activation energy either at high temperature or low temperature.

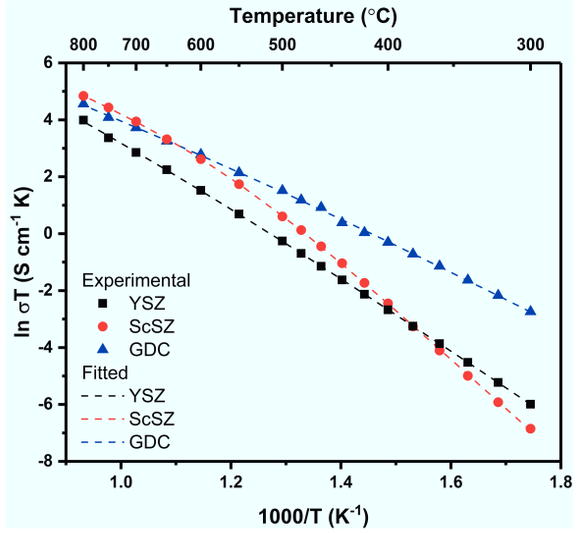

Figure 4.11: Comparison of experimental data (denoted as symbols) and fitted plots from "two barrier model" (as dashed lines) for YSZ (black), ScSZ (red) and GDC (blue) as a function of reciprocal temperature

Table 4.6: Fitting parameters of conductivity data for YSZ, ScSZ and GDC using the two barrier model as well as the fitted activation energy without two barrier mode from 300–800 °C

Material	γ_1 [K S cm^{-1}]	γ_2 [K S cm^{-1}]	γ_1/γ_2	$E_{a,1}$ [eV]	$E_{a,2}$ [eV]	E [eV]
YSZ	5.26×10^5	2.54×10^7	48.3	0.80 ± 0.09	1.14 ± 0.03	1.05
ScSZ	3.55×10^5	1.6×10^{10}	45070	0.72 ± 0.03	1.50 ± 0.01	1.26
GDC	1.01×10^5	4.8×10^6	47.5	0.62 ± 0.06	0.89 ± 0.03	0.77

In Figure 4.12, we compare our measured ionic conductivity with the values reported in other literature for YSZ (Figure 4.12a), ScSZ (Figure 4.12b) and GDC (Figure 4.12c). It should be pointed out here that the selected citations all have exactly the same composition as the materials used in this work. Since YSZ is an established electrolyte material for SOFC, the reported ionic conductivity values for YSZ are consistent with each other [144, 154, 155](all the YSZ used in these references are commercial powder manufactured by TOSOH, Japan). However, some scatters exist for ScSZ and GDC. For ScSZ, our data agree well with other reported values [54, 156, 157]. But the reason for the lower ionic conductivity observed in [158] is not clear, which might be attributed to the microstructure (no detailed information is provided except a relative sintering density of 94 %) or the impurity level of the raw powder (lab-synthesized ScSZ powder by Glycine-nitrate process

and then ball milled). For GDC, our measured values also show a good agreement with other reports [23, 159]. Though the microstructure reported in [160] is similar to ours, with average grain size of 1.22 µm and relative sintering density of 95 % after sintering at 1400 °C, their ionic conductivity is lower, where we assume the reason could be the lower gadolinium content caused by the polyol microwave assisted method they used for the synthesis of the powder.

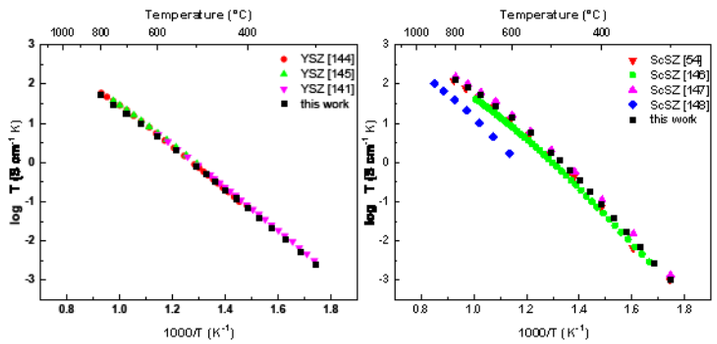

(a) YSZ (b) ScSZ

(c) GDC

Figure 4.12: Ionic conductivity comparison with values in other reports

4.3.4 *Grain size effects - a simple model*

Due to their lower conductivity, the grain boundaries have a detrimental effect on the total ionic conductivity of a given electrolyte. Therefore, we are interested in the effect of grain size on the total conductivity of a material. The idea is that a thin electrolyte consisting of only one single grain in the oxygen transport direction may show a different conductivity than predicted from bulk conductivity values of a polycrystalline ceramic. In addition, effect of grain size for a polycrystalline

material can be predicted. To investigate the magnitude of the grain size effect, we consider a "brick layer" model as shown in Figure 4.13:

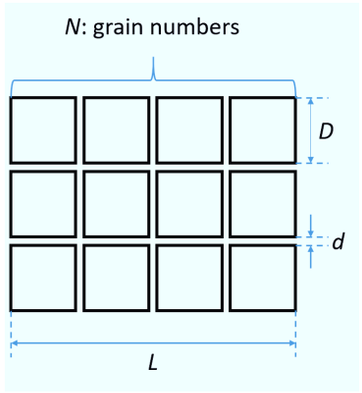

Figure 4.13: "Brick Layer" model of a poly-crystalline material, with grain boundary thickness of d, grain size of D, sample thickness of L and grain number of N

We assume the ceramic consists of identically shaped grains with a size D that equals the average grain size of the real ceramic. The grains are separated by grain boundaries of thickness d. Then the area specific resistance (ASR) for such a poly-crystalline material can be calculated as following:

$$ASR = \frac{L}{\sigma_{total}} = \frac{(N-1)d}{\sigma_{gb}} + \frac{ND}{d} \tag{4.4}$$

The effective grain boundary thickness d can be calculated from:

$$d = \frac{C_b}{C_{gb}} D \tag{4.5}$$

Using the capacitance value in Table 4.4 and average grain size in Table 4.7. The grain boundary thickness was calculated and compared with the grain size D in Table 4.7.

Table 4.7: Comparison of grain size D and grain boundary thickness d

Material	d (nm)	D (µm)	D/d
YSZ	2.3	2.28	990
ScSZ	5.4	2.97	550
GDC	3.6	0.73	203

As we see that, $D \gg d$, therefore, $N \approx L/D$, which can further simplify Equation 4.4 to:

$$ASR = \frac{d}{\sigma_{gb}}(\frac{L}{D} - 1) + L\frac{1}{\sigma_b} \tag{4.6}$$

By assuming that the values of d, σ_b, σ_{gb}, C_{gb} and C_b are independent on the average grain size, the relationship between ASR and grain size D for different given electrolyte thicknesses at 500 °C is plotted Figure 4.14. The targeted ASR with value of $0.1\,\Omega\,cm^2$ is marked by a dashed line.

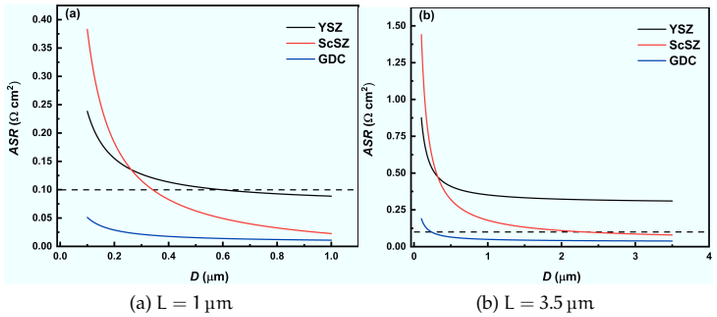

(a) $L = 1\,\mu m$ (b) $L = 3.5\,\mu m$

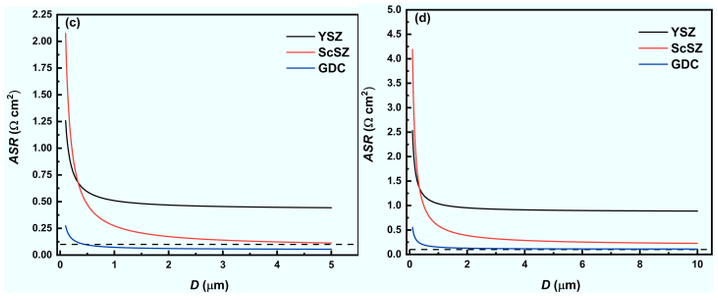

(c) $L = 5\,\mu m$ (d) $L = 10\,\mu m$

Figure 4.14: The dependence of ASR_{el} on the grain size for different fabricated electrolyte thickness L (T = 500 °C)

Comparing Figure 4.14, it is easy to see that using GDC might be easier and cheaper than YSZ and ScSZ in terms of electrolyte layer processing for reaching an ASR of electrolyte lower than $0.1\,\Omega\,cm^2$ at 500 °C. For YSZ, the only possible way of using it at 500 °C is to fabricate an YSZ electrolyte as thin as $1\,\mu m$ and at the same time, the average number of grain boundaries along the ionic conducting pathway should be less than three. While we do not have to fabricate a ScSZ layer as thin as $1\,\mu m$ (only $\sim 3.5\,\mu m$ is needed), the average grain size along the ionic conducting pathway should be larger than $2\,\mu m$. On the other

hand, a thickness of 5 µm with grain size larger than 0.9 µm is required for using GDC, which could be easily achieved by screen printing or tape casting.

4.4 SUMMARY

In this chapter, we compare the conductivity of dense ceramics made from well-defined, industrial-grade starting powders. We provide the information about the starting powder properties (including particle size distribution, powder morphology, impurity level and specific surface area), sintering behavior (dilatometry) and microstructure after sintering (porosity and average grain size). According to the conductivity results, we think that the use of these three materials should depend on the temperature of application. In the traditional high temperature range ($> 700\,^{\circ}C$), thin YSZ can still be viewed as the first choice for the electrolyte material for SOFC. At much lower temperature ($< 500\,^{\circ}C$), GDC seems to be the best potential electrolyte material due to its superior ionic conductivity. Using a simple "brick layer" model, we show that the grain size is relevant for the prediction of ASR values of the electrolyte. This tool gives the possibility to predict the influence of the microstructure of a thin, supported electrolyte on its conductance, and allows the targeted design of electrolyte microstructure.

5 DEVELOPMENT OF GDC ELECTROLYTE

One conclusion from the last chapter is that GDC seems to be the best potential electrolyte material at low temperature compared to YSZ and ScSZ due to its superior ionic conductivity. That means the fabrication of a GDC electrolyte might be easier and cheaper than YSZ and ScSZ in terms of electrolyte layer processing. Therefore, in this chapter, we discuss the development of screen printed GDC electrolyte layer. Due to the development and availability of anode supports in JÜLICH, two different anode layers are used: one is NiO/YSZ and the other is NiO/GDC. The corresponding drying, sintering and reducing behavior of the fabricated electrolyte on these two different anodes are discussed. After achieving a thin and dense GDC electrolyte, we talk about the single cell performance of the full cell with the fabricated GDC electrolyte. The post-test analysis of the SEM cross-section microstructure and laser microscopy top-view for the tested cell are also discussed.

5.1 DEVELOPMENT OF GDC ELECTROLYTE ON NIO/YSZ ANODE

Fabrication of a GDC electrolyte on an anode support with NiO/YSZ anode could be the simplest way, as the development of NiO/YSZ anode is state-of-the-art. However, to avoid the inter-diffusion between YSZ and GDC at high temperature (>1200 °C) [10, 11], nano-sized GDC is needed to lower its sintering temperature. Therefore, the first step is to synthesize the GDC screen printing paste by using nano-sized GDC powder.

However, the preparation of a screen printing paste using nano-sized powder is quite challenging. The reason is that the maximum solid content in the paste is limited due to the high surface area of the powder. For example, 50 % of YSZ powder with a B.E.T of 4.31 $m^2\ g^{-1}$ can be put in the screen printing paste while for the smaller YSZ powder with a B.E.T of 6.01 $m^2\ g^{-1}$, only 45 % can be put in the paste [96]. The standard JÜLICH procedure for the screen printing paste uses a powder with a B.E.T of 12.1 $m^2\ g^{-1}$ while the nano-sized GDC powder we intend to use has a B.E.T of 100 $m^2\ g^{-1}$, indicating a new screen printing paste recipe has to be developed.

5.1.1 *Synthesis of screen printing paste*

5.1.1.1 *Effects of powder content*

Three groups of pre-suspension with different compositions of nano-sized powder to solvent ratio 40:60, 50:50 and 60:40 (in wt.%) were prepared first to find the maximum acceptable solid content in the suspension. For the powder-to-solvent ratio of 40:60, the viscosity of the paste was too low (like water) to do the screen printing, meaning excessive solvent in the paste. For the other two groups with powder-to-solvent weight ratio of 50:50 and 60:40, it was feasible to do the screen printing after mixing with transport agent. As a result, the surface morphology of the dried electrolyte layers screen printed by these two pastes were checked by laser microscopy and shown in Figure 5.1. Some cracks were found after drying for both layers. The trend is that the dried layer with less content of powder has more cracks, indicating that a higher solid content could help to mitigate the crack formation during drying. Thus, another pre-suspension with a little higher solid content was prepared (65:35, in wt.%), however, no homogeneous mixed suspension could be obtained due to the excessive solid. In conclusion, to mitigate the crack forming behavior after drying, more solid content should be put in the paste but at the same time due to the larger B.E.T. of nano-sized powder, only less than 65 wt.% powder content is allowed to be put in the pre-suspension.

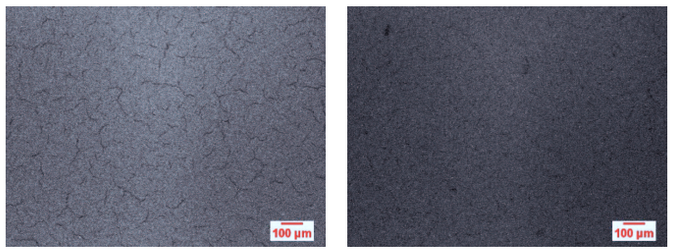

(a) 50 wt.% (b) 60 wt.%

Figure 5.1: Surface morphology of screen printed films after drying at 50 °C for 2 h with different powder content

5.1.1.2 *Effects of binder content*

Generally, binder is used in the paste with the aim of improving the particle network strength within the paste and could help to mitigate the cracks forming behavior. As the binder was added into the pre-suspension in the way of transport agent (a mixture of binder and solvent), we controlled the binder content through the control of transport agent content. Three different pastes were synthesized (named

paste A, B and C, shown in Table 5.1) with different binder content and their surface morphology of dried film are shown in Figure 5.2. It obviously shows that with the increase of binder, the number of crack is decreasing. However, even for the paste C with 5 wt.% binder, there were still cracks, indicating more binder needed to further eliminate the cracks. However, under the ratio of powder to solvent to 1 : 1, it is not possible to add more transport agent to add more binder as that would also add more solvent. Therefore, another powder to solvent ratio of 2 : 5 is set to add more binder content.

Table 5.1: The summary of paste composition for screen-printing paste

paste	paste composition (wt%)				P/S[1]	B/P[2]
	pre-suspension			transport agent		
	powder	solvent	dispersant	binder+solvent		
A	41.9	39.6	15.7	2.8	1	0.01
B	41.6	34.5	15.6	8.3	1	0.03
C	41.2	29.6	15.5	13.7	1	0.05
D	25.2	48.6	9.4	16.8	0.4	0.10
E	24.8	41.0	9.3	24.8	0.4	0.15
F	24.0	19.2	8.9	47.9	0.4	0.30
G	34.4	29.7	12.9	23.0	0.7	0.10
H	25.2	48.6	3.1	16.8	0.4	0.10

[1] P means the powder content, S means the total solvent content, including the solvent in the pre-suspension and transport agent
[2] B means the binder content

Paste D and F were synthesized with more binder content (Table 5.1). The corresponding surface morphology of films after drying are compared in Figure 5.3, from which we can see that there seems to be no cracks after drying for both pastes under lower resolution observation.To further confirm that, we observe the surface morphology with the highest resolution, in which we can see there are still some minor cracks observed for the paste with binder content of 10 wt.%, while in-homogeneous layer observed for the one with binder content of 30 wt.%.

So far, only paste D, with weight ratio between powder and solvent of 40 : 60, binder and powder of 0.1, has nearly crack-free layer after drying. Therefore, we synthesized two more pastes, one paste (paste F in Table 5.1) with same powder content as paste D but more binder content, while the other paste, paste G, with same binder content as paste D but more solid content. The surface morphology of each dried film is shown in Figure 5.4. However, the cracks were still observed after increasing either solid or binder content.

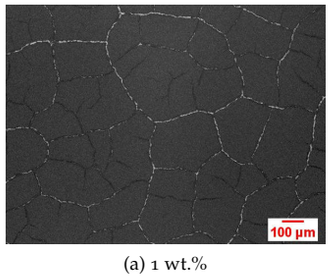

(a) 1 wt.%

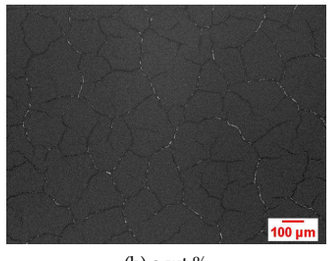

(b) 3 wt.%

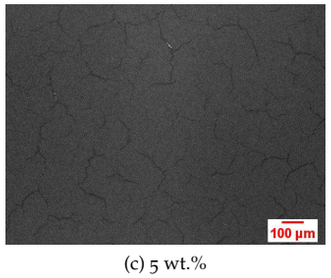

(c) 5 wt.%

Figure 5.2: Surface morphology of screen printed films after drying at 50 °C for 2 h with different binder content

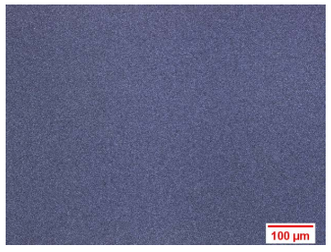

(a) 10 wt.% at lower resolution

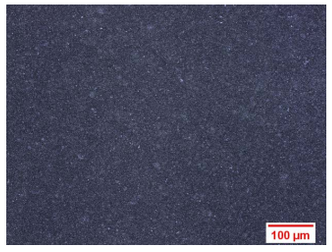

(b) 30 wt.% at lower resolution

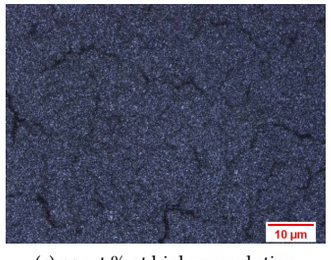

(c) 10 wt.% at higher resolution

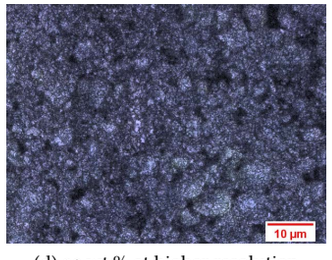

(d) 30 wt.% at higher resolution

Figure 5.3: Surface morphology of screen printed films after drying at 50 °C for 2 h with different binder content

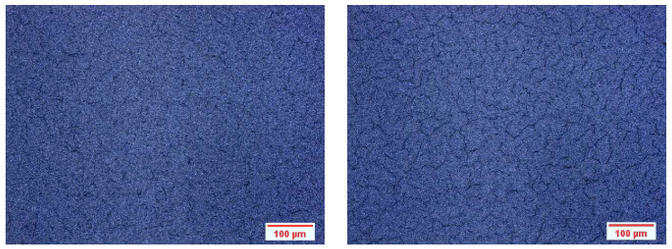

(a) B : P = 15 wt.%, P : S = 40 wt.% (b) B : P = 10 wt.%, P : S = 70 wt.%

Figure 5.4: Surface morphology of screen printed films after drying at 50 °C for 2 h with different ratio of binder to powder (B:P) and powder to solvent content (P:S)

5.1.1.3 *Effects of dispersant content*

Right now, the content of powder, solvent and binder has been optimized. The trend is that with more powder and binder, the cracks formed after drying could be mitigated but there is a maximum acceptable powder and binder content in the paste. However, among all the chemicals in the paste, the dispersant agent content has not been optimized. Normally, the dispersant content is based on the surface area of the particle, a range of 1–3 mg m^{-2}, since the function of dispersant is to separate the particle by forming an electrostatic or a steric barrier around the particle surface (in this work, the BYK-P104 dispersant agent is used and the steric stabilization acts). The B.E.T provided by the manufacturer is around 100 m^2 g^{-1} and all the previous pastes used the dispersant content based on this B.E.T value. However, if the dispersant content is excessive, cracks can be caused due to two reason: fist, the excessive dispersant (free, not adsorbed) can promote the agglomeration of the particle in the paste through a depletion mechanism [161]; second, the green density is decreased after drying due to the excessive dispersant content evaporation. Therefore, we measured the B.E.T and found that the nano-sized GDC powder only have a B.E.T of 33 m^2 g^{-1}, rather than 100 m^2 g^{-1}. Accordingly, on the base paste composition for nearly crack-free paste D, we synthesized a new paste, paste H, with dispersant content based on a B.E.T of 2 g m^{-2}. Compared in Figure 5.5 are the surface morphology after drying for paste D (Figure 5.5a) and paste H (Figure 5.5b). It is obvious that when decreasing the dispersant content to a value based on the B.E.T of 33 m^2 g^{-1}, a crack-free dried layer can be successfully obtained, even observed under the highest resolution.

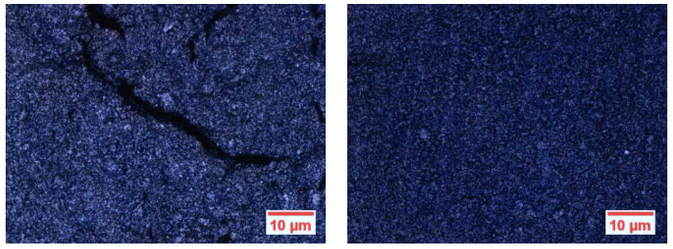

(a) based on B.E.T = 100 $m^2\ g^{-1}$ (b) based on B.E.T = 33 $m^2\ g^{-1}$

Figure 5.5: Surface morphology of screen printed films after drying at 50 °C for 2 h with dispersant content based on different B.E.T area

5.1.2 *Calcination behavior*

The crack-free layer after drying was then calcined to examine its microstructure since the low solid content achieved can be expected to result in a low sinterability. Figure 5.6 presents the cross-sectional SEM microstructure of the thin layer after drying and calcining. Figure 5.6a shows that a 3 µm thick layer with no obvious cracks obtained after drying, in agreement with the top-view morphology observed by laser microscopy. The dried layer was then calcined at 500 °C for 2 h to burn out the binder and the resulted microstructure after calcining was shown in Figure 5.6b. Though the thickness was nearly unchanged after calcination (no shrinkage happens due to the low calcination temperature), some cracks appeared after calcining, which should be caused by the burnout of binder. We calculated the green density after binder burn out, which is only as low as 30 %. Regarding the observed cracks, we assume there might be two reasons. First, some agglomerations observed in the microstructure of dried layer result in cracks during the calcination. Second, the green density is too low to get a dense calcined layer. Techniques to enhance the green density should be considered.

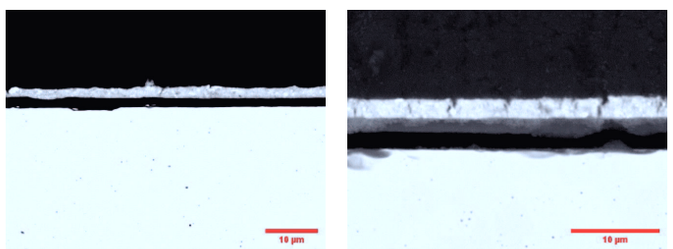

(a) after drying (b) after calcination

Figure 5.6: Cross-sectional microstructure of the electrolyte layer after different heat treatment

5.1.3 *Improvement of green density*

As discussed above, the green density of the single screen-printed layer is too low to fabricate a dense microstructure after calcining. Therefore, we tried to infiltrate more GDC into the calcined GDC layer to improve the green density. A GDC infiltration liquid was synthesized by dissolving $Ce(NO_3)_3 \cdot 6\,H_2O$ and $Gd(NO_3)_3 \cdot 6\,H_2O$ into the deionized water. The precursor solution was infiltrated the calcined layer under vacuum conditions. To increase the infiltrated content, the process was repeated 5 times. As a result, an additional average weight of $0.18\,mg\,cm^{-2}$ was gained after infiltration, a weight increase of 30 % compared to the green density before infiltration. But some minor cracks could still be observed after calcining (shown in Figure 5.7a). Then the layer was sintered to see the effects of infiltration, but as can be observed that the calcined layer was incompletely sintered, shown in Figure 5.7b. We propose that when the electrolyte is sintered on a non-shrinking substrate, there is no compressing effects from the shrinkage of the substrate to densify the electrolyte layer.

In conclusion, we believe it is difficult and challenging to fabricate a dense GDC electrolyte layer by screen printing a paste with nano-sized GDC powder on a non-shrinking substrate. First, the green density is too low after screen printing using the nano-sized GDC powder. Second, it is challenging to densify the electrolyte without the shrinking effects from substrate.

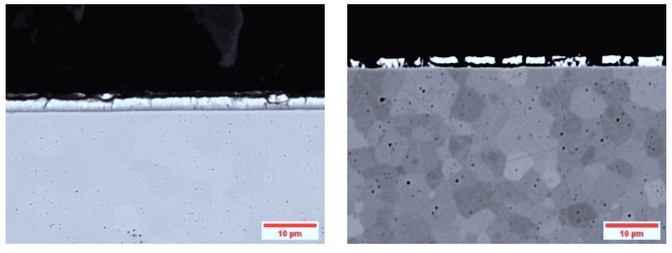

(a) after calcination (b) after sintering

Figure 5.7: Cross-sectional microstructure of the infiltrated electrolyte layer after different heat treatments

5.2 DEVELOPMENT OF GDC ELECTROLYTE ON NIO/GDC ANODE

Owing to the difficulties to fabricate a dense GDC electrolyte on non-shrinking substrate by using nano-sized GDC powder, we turned to the development of a thin GDC electrolyte on NiO/GDC anode. By using NiO/GDC as anode, we have no inter-diffusion issues and as a result, no need to use nano-sized powder to decrease the sintering temperature of the GDC electrolyte.

5.2.1 *Paste characterization*

5.2.1.1 *Particle size distribution in the pre-suspension*

The GDC pre-suspension was prepared following the standard recipe for preparing the YSZ pre-suspension. The PSD of GDC in the pre-suspension was checked and compared with the PSD of YSZ in the pre-suspension used for the synthesis of standard YSZ electrolyte paste, shown in Figure 5.8. Similar to YSZ, the GDC powder also has a narrow PSD without significant agglomeration, indicating that a homogeneous mixing and effective ball milling was achieved for the pre-suspension. However, their average particle size (d_{50}) are obviously different, detailed in Table 5.2. The d_{50} of GDC is much smaller than that of YSZ, 0.13 µm compared to 0.33 µm. This should be the reason why the maximum solid content of GDC in the pre-suspension is less than that of YSZ.

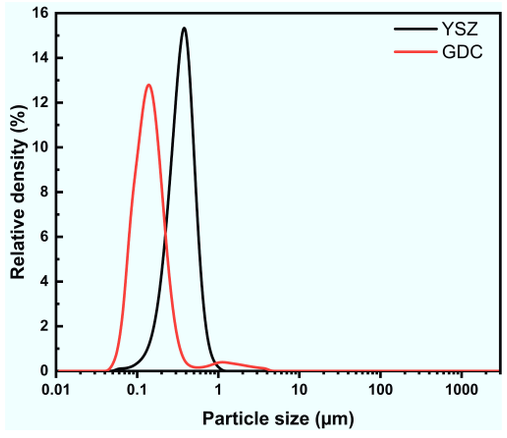

Figure 5.8: The comparison of particle size distribution for YSZ and GDC in the pre-suspension

Table 5.2: Comparison of PSD for YSZ and GDC

powder	PSD (μm)		
	d_{10}	d_{50}	d_{90}
YSZ	0.19	0.33	0.50
GDC	0.08	0.13	0.23

5.2.1.2 *Viscosity of the paste*

After getting a satisfactory GDC pre-suspension (composition is detailed in the "Experiment" Chapter), the GDC paste was synthesized and its viscosity was examined and compared with the standard YSZ screen printing paste, in Figure 5.9. No delatant behavior was observed for the GDC paste even at high shear rate. Its viscosity is close to that of the YSZ suspension. For example, at a reference shear rate of 104 s^{-1}, the viscosity of YSZ electrolyte paste is 17.9 Pa s and the GDC electrolyte paste has a similar viscosity of 16.1 Pa s. This could provide a good printability generally correlating with viscosity in the range from 4 Pa s to 12 Pa s at 100 s^{-1} [96]).

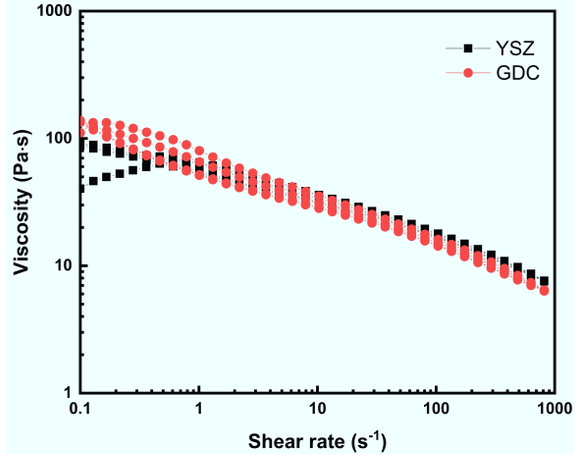

Figure 5.9: The comparison of viscosity between standard YSZ electrolyte paste and GDC electrolyte paste

5.2.2 *Drying behavior*

Using the GDC paste with similar viscosity to the standard YSZ paste discussed above, a thin GDC layer was screen printed on the anode support with NiO/GDC as AFL. After drying (60 °C for 30 min), the top

surface morphology of the dried electrolyte layer was checked by laser confocal microscopy. In overview, no cracks were observed after drying and a homogeneous dried layer was achieved , shown in Figure 5.10a. In addition to that, some black spots were observed, which could be some holes or agglomerates. To observe the local defects in detail, observation at highest resolution was carried out, shown in Figure 5.10b. It shows that these black spots are convex, resulting from agglomerates in the paste (the minor second peak of PSD for GDC observed in Figure 5.8). Besides the black spots, there also exists some dust from the air, like the fiber observed in the left corner in Figure 5.10a.

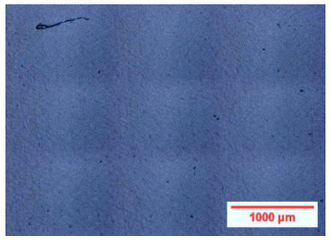

(a) Overview

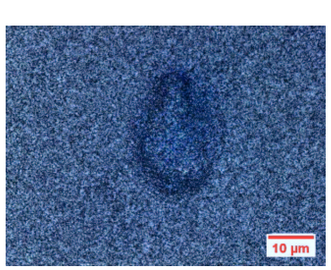

(b) local defect

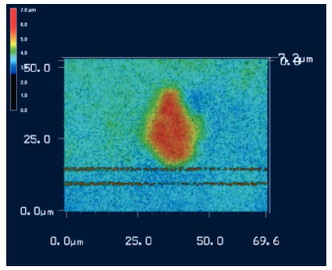

(c) local defect in 3D view

Figure 5.10: Top view (observed by laser microscope) of screen printed electrolyte layer after drying at 60 °C for 30 min

5.2.3 *Sintering behavior*

5.2.3.1 *Thermo-optical analysis at different temperatures*

The sintering behavior for the thin GDC electrolyte on NiO/GDC anode is shown in Figure 5.11, with the anode support side faces downwards and electrolyte side upwards. Figure 5.11a and Figure 5.11b are for anode support without GDC electrolyte while Figure 5.11c and Figure 5.11d are for anode support with GDC electrolyte. As shown in Figure 5.11a, the anode layer shrank faster than the anode support due to the finer structure of anode, compared to that of anode support, and the sample cambered upwards at first. When the anode support began

to sinter appreciably (1194 °C, nearly the same as the initial shrinkage temperature of the single anode support without any function layer), the curvature decreased and eventually the sample flattened. However, around 1346 °C, the cell started to camber slightly again. This could be a second sintering stage for the anode, which might be clarified through the observation of the sintering behavior for a free-standing anode layer. Similarly, as shown in Figure 5.11c and Figure 5.11d, when fabricating a GDC electrolyte layer on top of the anode, the sintering behavior was nearly the same, with around the same initial shrinkage temperature and same two sintering stages. However, due to the addition of GDC electrolyte layer, the curvature was a little larger than Figure 5.11a when the first sintering stage finished. But finally, due to the shrinkage of the anode support and the gravity force acting on the viscous materials at these high temperatures, the half cell got flattened.

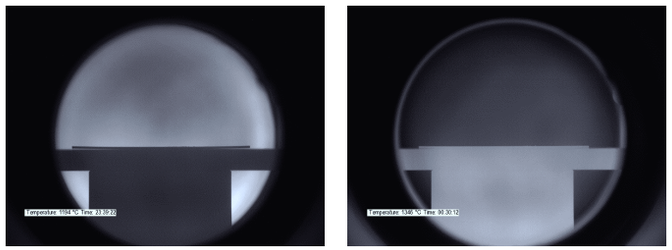

(a) T=1194 °C, without electrolyte

(b) T=1346 °C, without electrolyte

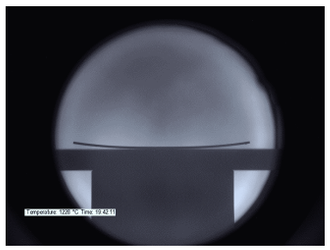

(c) T=1228 °C, with electrolyte

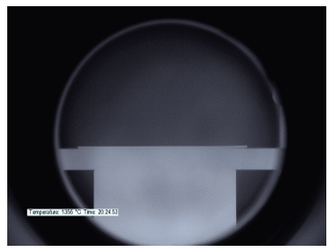

(d) T=1356 °C, with electrolyte

Figure 5.11: Comparison of warpage behavior during sintering

Shown in Figure 5.12 is a topography measurement of the half-cell after sintering without an additional flattening step. A small waviness was observed, possibly caused by the in-homogeneity of the substrate. However, the sintered half-cell could still be treated as "flat", if comparing the profile of the height in 'Z' axis (maximum 0.12 mm) with the thickness of the cell (~ 0.51 mm). This thin electrolyte development simplifies further the electrolyte processing as normally an additional flattening step is needed to flatten the thicker YSZ electrolyte (10 µm). That could be explained by Cai [162] as he mentioned that a

thickness decrease (under an critical value) of the top layer for a bi-layer system could decrease the bending.

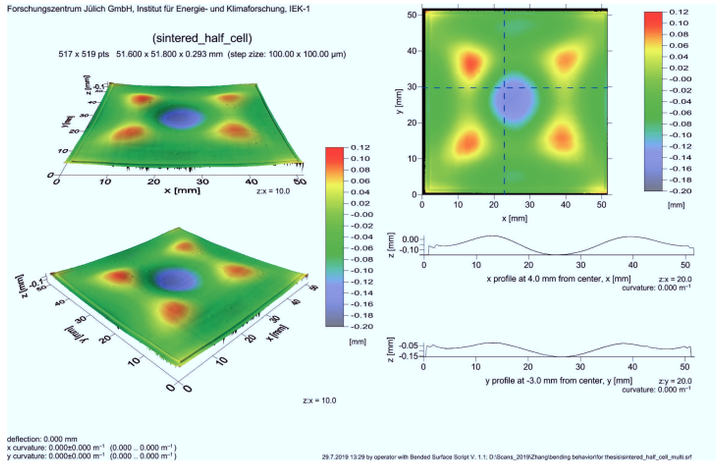

Figure 5.12: Topography measurement of the sintered half-cell

5.2.3.2 *SEM cross-sectional microstructure after sintering*

The cross-sectional microstructure after sintering was checked by SEM and shown in Figure 5.13a, with the top layer corresponding to the electrolyte, middle to the anode and the bottom to the anode support. The thickness of the electrolyte obtained is around 3.5 µm. If calculated on an ASR_{el} of 0.1 $\Omega\,cm^{-2}$ and the ionic conductivity we measured previously, a thin GDC electrolyte layer with thickness around 5.9 µm is enough to achieve this ohmic resistance for the SOFC operation at 500 °C. To clearly observe the grain boundary density in the electrolyte layer, the electrolyte was thermally etched at 1300 °C for 1 h, and the microstructure is shown in Figure 5.13b. On average, the electrolyte consists of only 3 to 5 grains along the direction of ionic conduction. As the grain boundary resistance is a big contribution to the total resistance in low temperature regime [163], a small grain boundary density observed in our sintered electrolyte layer is of great importance. Moreover, from Figure 5.13a and Figure 5.13b, we can see that we can obtain a thin electrolyte layer without compromising the density of the microstructure. The surface morphology after sintering was also checked by SEM and shown in Figure 5.13c. The grain size distribution was very homogeneous and only a few defects were observed. From the higher magnification image Figure 5.13d, it was clearly presented that the diameter of these holes was less than 0.5 µm. In addition to the SEM images, the air leakage rate was checked, which is a more representative and practical criterion for the gas tightness of the electrolyte. The cell area for air leakage rate measurement was a normal half-cell size with

$4\,\mathrm{cm} \times 4\,\mathrm{cm}$ after sintering, and the result was shown in Table 5.3. Compared with the JÜLICH threshold for the leakage rate, the cell after sintering is dense enough and does not contain initial defects.

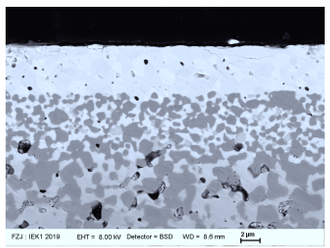

(a) Cross-section of half cell

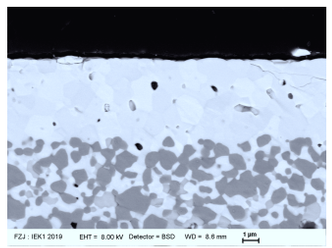

(b) Cross-section of electrolyte

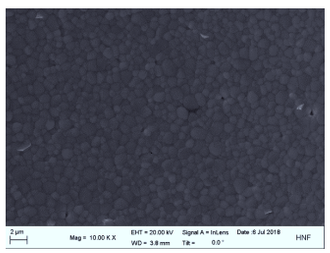

(c) Top-view of electrolyte

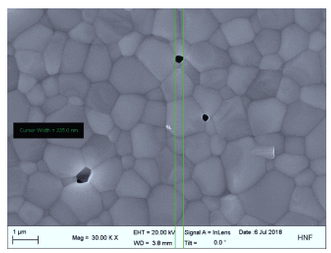

(d) Top-view of electrolyte with residual pores

Figure 5.13: SEM images of the half-cell after sintering at 1400 °C for 5 h

Table 5.3: Leak test results comparison

sample	leakage rate ($\mathrm{hPa\,dm^2\,s^{-1}\,cm^{-2}}$)	
	air	He
3.5 µm GDC electrolyte half-cell	3.54×10^{-6}	
JÜLICH standard half-cell	8.0×10^{-6}	2×10^{-5}

5.2.4 *Reducing behavior*

5.2.4.1 *Chemical expansion*

As observed in Figure 5.13a, both the anode and anode support were dense after sintering, which could contribute to the low air leakage. Therefore, the cell was reduced to make the anode and anode support porous (due to the NiO reduction to Ni) to further examine the "real" air leakage rate of electrolyte alone. However, the standard reduction condition for a standard JÜLICH half cell (900 °C for 3 h) does not apply for a half cell involved GDC layer as it will deform severely due to the chemical expansion of GDC at high temperature. Introduced by Jeong [31], reducing a half cell with GDC layer at lower temperature but longer time could alleviate the deformation behavior. Therefore, we tried to reduced the half cell at 700 °C for 10 h. However, the cell still had a high degree of deformation after reduction. To suppress that, we put a load on top of the half cell during reduction (schemed in Figure 5.15), with a Ni mesh between the load and cell to improve the contact area between the reducing atmosphere and the cell. As shown in Figure 5.14a, the cell deformation can be effectively suppressed and looks nearly flat after reduction.

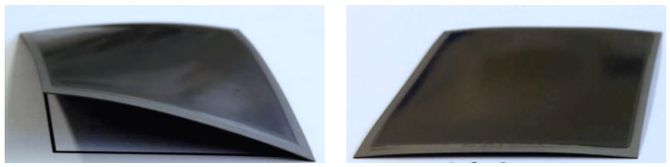

(a) without load on top (b) with load on top

Figure 5.14: Comparison of photographs for reduced cell under different state

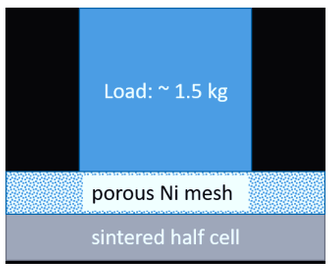

Figure 5.15: The scheme for using a load to depress the deform during reduction

5.2.4.2 *SEM cross-sectional microstructure*

The cross-sectional microstructure of the reduced cell was checked by SEM, shown in Figure 5.16. The anode support and anode layer became porous due to the reduction of NiO. Then the air leakage rate was measured again for the reduced cell. Compared to the JÜLICH threshold (seen in Table 5.4), the low air leakage rate after anode reduction proves the GDC electrolyte fabricated by screen printing and after sintering at 1400 °C remaining dense.

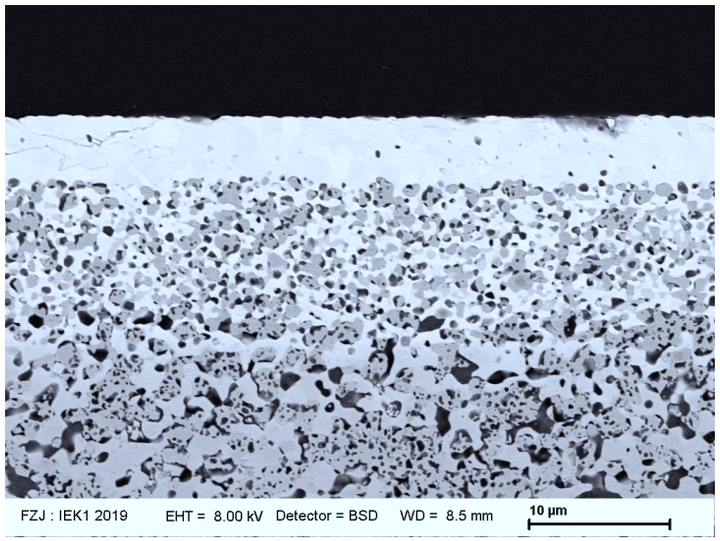

Figure 5.16: SEM cross-section image for the reduced half-cell after reducing at 700 °C for 10 h

Table 5.4: Leak test results comparison after reducing at 600 °C for 10 h

sample	leakage rate ($hPa\ dm^2\ s^{-1}\ cm^{-2}$)	
	air	He
3.5 µm GDC electrolyte half-cell	2.3×10^{-5}	
JÜLICH standard half-cell	2.0×10^{-5}	2.3×10^{-4}

5.2.4.3 *TGA measurement*

A series of thermal gravity analysis (TGA) measurements for the half-cells reduced at different temperatures in Ar atmosphere with 2.9 % H_2 atmosphere were done, shown in Figure 5.17. The temperature has a significant effect on the reduction kinetics. The reduction proceeded

much faster and the mass stabilized within 10 h when the cell was reduced at 800 °C. On the other hand, when the cell was reduced at 500 °C, the reduction process was so sluggish that the mass did not stabilize even after 48 h. Therefore, to ensure a complete reduction of the cell in Ar with 2.9 % H_2, the temperature should at least be higher than 700 °C. However, during the single cell performance test, the cells are measured under pure or moist H_2, and reduction will be much faster than reduction under a low concentration of H_2. Table 5.5 compares the weight loss of the cell reduced at 600 °C, 700 °C and 800 °C for 12 h. The cell can be completely reduced at 600 °C for 12 h. Therefore, from a point of view to minimize the deformation of the cell caused by the chemical expansion of the GDC electrolyte at high temperature, the reduction temperature should be decreased to as low as 600 °C.

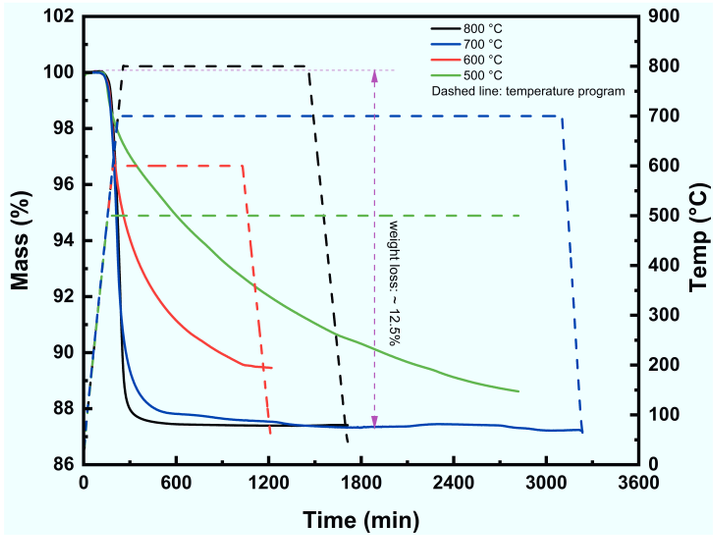

Figure 5.17: Thermogravimetric (TG) measurement for half cells measured under Ar/H_2 (2.9 % H_2) at different temperatures

Table 5.5: Weight loss for half cell reduced at different temperature under pure H_2 for 12 h

	600 °C		700 °C		800 °C	
oxidized (g)	1.8406	1.8125	1.807	1.8549	1.8213	1.8969
reduced (g)	1.6103	1.5856	1.582	1.6234	1.5936	1.6599
weight loss (%)	12.51	12.52	12.45	12.48	12.50	12.49

5.2.5 *Single cell performance*

The single cell performance of the cell with GDC as electrolyte discussed above was characterized in China University of Mining and Technology (CMUT), shown in Figure 5.18. A low OCV, lower than 0.9 V, was observed over the entire temperature range. Even the temperature was as low as 500 °C, the OCV was still as low as 0.85 V. The OCV measured here are lower compared to the values reported by other literature [164–167] (compared in Table 5.6) and the Nernst Voltage (Figure 5.19). We assume two reasons could lead to the low OCV: first, the gas leakage, caused by some minor defects in the electrolyte; second, the current leakage, caused by the partial reduction of Ce^{4+}. As a result of the low OCV, the power density was also poor. The cell only generated a power density of 0.034 $W\,cm^{-2}$ at 0.7 V and 650 °C, far lower compared to other reports (listed in Table 5.6). Despite the fact low OCV could lead to a low power density [166], the difference between the OCV in this work and the reported values is small (around 50 mV difference). Therefore, we assume the low power density should be mainly caused by the large cell resistance, but this will be further checked by the impedance measurements.

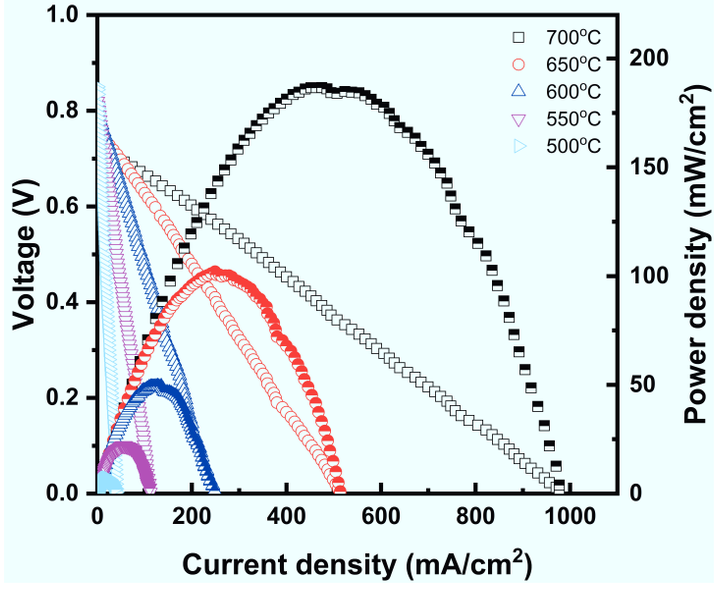

Figure 5.18: Cell voltage and power density as a function of current density

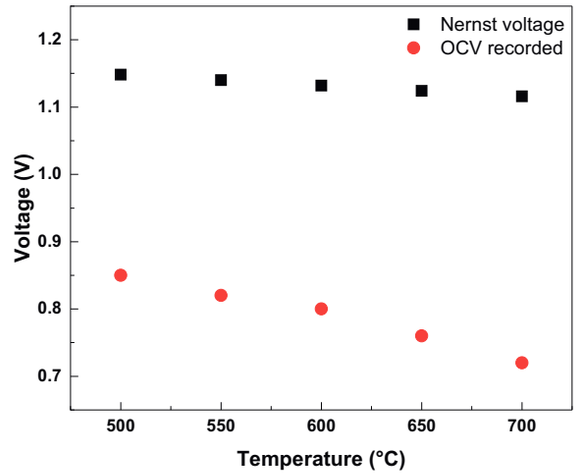

Figure 5.19: Cell voltage as a function of temperature

Table 5.6: Cell performance comparison with reported values at different temperature

650 °C		600 °C		550 °C		Ref.
OCV	PD*	OCV	PD	OCV	PD	
V	$W\,cm^{-2}$	V	$W\,cm^{-2}$	V	$W\,cm^{-2}$	
0.76	0.034	0.8	0.024	0.85	0.011	this work[a]
-	~ 0.139	0.85	~ 0.126	0.92	~ 0.109	[164][b]
0.79	~ 0.252	0.85	~ 0.329	0.89	~ 0.252	[165][c]
0.80	~ 0.612	0.83	~ 0.505	0.91	~ 0.345	[166][d]

* PD is short for the power density, measured at a voltage of 0.7 V
[a] NiO/GDC-GDC(3.5 µm)-$La_{0.58}Sr_{0.4}CoO_{3-\delta}$
[b] NiO/GDC-GDC(26 µm)-$Sm_{0.5}Sr_{0.5}CoO_{3-\delta}$/GDC
[c] NiO/GDC-GDC(20 µm)-$Sm_{0.5}Sr_{0.5}CoO_{3-\delta}$/GDC
[d] GDC-GDC(10 µm)-$La_{0.6}Sr_{0.4}Co_{0.2}Fe_{0.8}O_{3-\delta}$/GDC

Shown in Figure 5.20 is the impedance spectrum of a single cell measured under open circuit conditions from 700 °C to 500 °C. The low-frequency and high-frequency intercept correspond to the total resistance and ohmic resistance (R_o), respectively, while the difference between low-frequency and high-frequency intercepts represents the polarization resistance (R_p). First, it shows that the major contribution to the total cell resistance is R_p. As temperature decreases, the R_p increases significantly, indicating the main resistance for the low temperature SOFC comes from the electrodes. Second, from the comparison in

Table 5.7, both the R_o and the R_p are much higher than other reports, especially the R_p. As the thickness of our GDC electrolyte is the thinnest (3.5 µm) among all these references (26 µm in [164], 20 µm in [165], 10 µm in [166]), it can be assumed that the high ohmic resistance does not only come from the electrolyte itself. It is assumed that, apart from the electrolyte, some other resistance may contribute to R_o, such as the contact resistance that comes from the test setup. Another potential reason is that the effective measured cell area is decreased due to the bad adhesion of the cathode. With regard to much higher R_p, there might be a bad adhesion between electrodes and electrolyte or the porosity of the electrodes is too low, which will be examined by SEM.

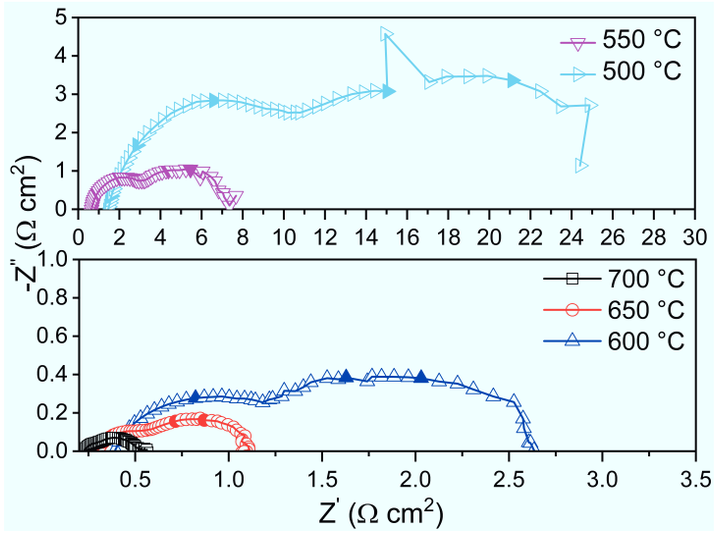

Figure 5.20: Impedance spectra under OCV conditions

Table 5.7: R_o and R_p ($\Omega\,cm^2$) comparison with reported values at different temperature

650 °C		600 °C		550 °C		Ref.
R_o	R_p	R_o	R_p	R_o	R_p	
0.3	0.79	0.39	2.24	1.44	22.96	this work
0.5	0.1	0.6	0.7	0.8	1.8	[164]
0.141	0.112	0.160	0.175	0.306	1.146	[165]
0.051	0.036	$\leqslant$0.1	$\leqslant$0.1	~0.2	~0.48	[166]
0.82	953	0.85	497	0.92	101	[167]

5.2.6 *Post-test analysis of the tested cell*

Observed from the fracture microstructure of the cell after testing (seen in Figure 5.21), nearly no cathode layer could be found after testing. Only some loose cathode residue was seen on the surface of the electrolyte. The cathode layer was found to delaminate from the electrolyte during testing, indicating a weak adhesion between the cathode and electrolyte. This could be further confirmed by an optical top-view for the tested cell shown in Figure 5.22, where we observed that only partial cathode layer (the black part is the cathode) remained after the test. Although the interface between the electrolyte and the anode layer kept its integrity after testing and no delamination or cracks were found, the microstructure of the anode seemed worse than the JÜLICH standard cell. It appeared from Figure 5.21 that Ni grains after reducing were separated from each other. A possible poor inter-connectivity of these Ni grains could also contribute to the large polarization resistance. To sum up, the much higher R_p observed in the impedance should come from the delamination of the cathode and under-development of the anode microstructure. One possible reason for the cathode delamination could be that the surface roughness of GDC electrolyte is too low (seen in Figure 5.13d) to lead a poor adhesion between cathode during sintering.

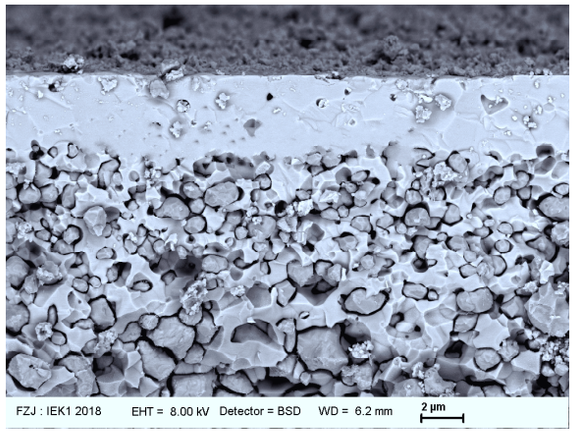

Figure 5.21: SEM fracture of full cell after single cell test

5.3 DEVELOPMENT OF ELECTRONIC BLOCKING LAYER

5.3.1 *PVD development*

In order to avoid the current leakage discussed previously, a PVD deposition of a YSZ layer was developed on top of the GDC electrolyte.

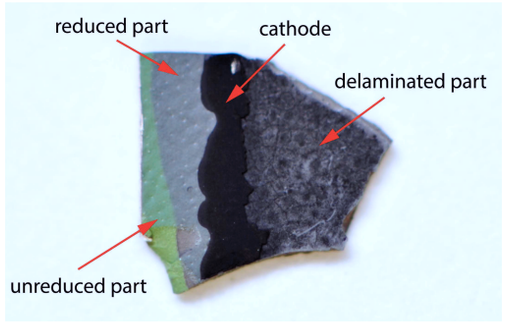

Figure 5.22: Optical photograph of a tested cell

Additionally, a GDC barrier layer was deposited on top of the YSZ layer to prevent the Sr diffusion from cathode. The PVD experiment was conducted several times to aim for thin and dense YSZ and GDC layers. After each measurement, the cross-sectional microstructure was checked by SEM to examine thickness and density. Figure 5.23 shows the optimization of the microstructure for YSZ and GDC layers by PVD step by step.

For the first round of PVD experiment, shown in Figure 5.23a, not fully dense YSZ electron blocking layer and GDC barrier layer were achieved with a corresponding thickness of 2 µm and 500 nm, respectively. As Ar ions assisted electron beam PVD (EB-PVD) was used for the deposition of YSZ layer, we assume the reason for the porous YSZ microstructure could be the bombardment of the Ar ions on the deposited YSZ, leading to the loss of some YSZ material. On the other hand, the GDC layer was deposited on the PVD YSZ layer by non-assisted reactive magnetron sputtering. Therefore, two reasons can lead to the porous GDC microstructure. First, the underlying PVD YSZ layer has a columnar microstructure but is not dense enough, which could not provide a good surface condition for fabricating a dense layer on top of it by PVD. The second reason could be the lack of bias power, as reported by Nédélec et al. [113] that an increased bias power could help to increase the density. Regarding the thicker layer of YSZ, the reason could be that the deposition time is too long, for 45 min.

Therefore, for the second round of PVD experiments, the YSZ layer was deposited by EB-PVD without Ar ions assistance and the deposition time was decreased from 45 min to 30 min; the GDC layer was deposited by bias assisted, with power of 300 *W*, reactive magnetron sputtering and the deposition time was increased a little bit at the same time to try to increase its density. The cross-sectional microstructure is shown in Figure 5.23b. The thickness of YSZ was successfully decreased from 2 µm to desired 600 nm. Moreover, the density of YSZ and GDC were also improved. However, the GDC barrier layer is a little thick, with thickness around 2 µm. The reason for the increased thickness of

GDC layer could be the combined effects of the introduction of the bias power and longer deposition time.

Therefore, for the third round of PVD experiments, the deposition time of the GDC layer was kept the same as the first round and all the other deposition parameters were kept as the same as the second round. The cross-sectional microstructure in Figure 5.23c shows dense and extremely thin YSZ and GDC layers finally realized, each with a thickness around 600 nm and 500 nm. It also shows a continuous and complete coverage of the two PVD layers on top of the underlying layers, which should guarantee good effects of blocking the electron conduction and Sr diffusion.

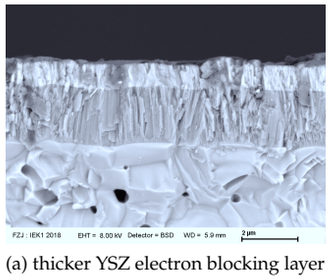

(a) thicker YSZ electron blocking layer

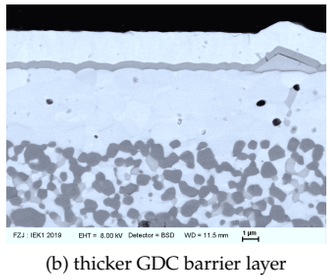

(b) thicker GDC barrier layer

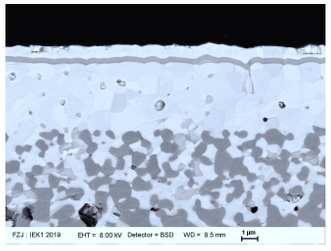

(c) final optimized layer

Figure 5.23: Cross-sectional microstructure of PVD layer, with the top layer of GDC barrier layer, middle layer of YSZ electron blocking layer and bottom layer of screen printed GDC electrolyte layer

Table 5.8: Comparison of PVD coating parameters

Parameters	first round		second round		third round	
	YSZ	GDC	YSZ	GDC	YSZ	GDC
Ar ion assistance	Yes	No	No	No	No	No
deposition time (min)	45	80	30	180	30	60
bias power (*W*) No	No	No	No	300	No	300

5.3.2 *Single cell performance*

After the addition of an YSZ electron blocking layer and a GDC barrier layer, a full cell was fabricated and measured the single cell performance (pure H_2 with 10 % H_2O is used as the fuel and ambient air is used as the oxygen). Prior to the single cell test, the cell was reduced at 850 °C until the monitored OCV stabilized. The cell voltage was recorded as a function of current density and the power density was also calculated, as shown in Figure 5.24. A very high performance was achieved not only for the high current density but also for a low current density (low current density is more suitable for stack application). For example, at 800 °C, a power density of 1.729 $W\,cm^{-2}$ could be achieved at 2 $A\,cm^{-2}$ while a high voltage of 0.969 V was reached at a low current density of 0.5 $A\,cm^{-2}$. The powder density at 0.7 V is commonly a "reference" to evaluate the cell performance. However, due to the the high performance of our cell, when the temperature is higher than 650 °C, the cell still maintains a high voltage than 0.7 V. On the other hand, with lower temperature, lower than 650 °C, the cell performance decreased a lot. For instance, when temperature went down to 500 °C, only a power density of 0.098 $W\,cm^{-2}$ was obtained at 0.7 V. The detailed cell performance at each temperature is compared in Table 5.9.

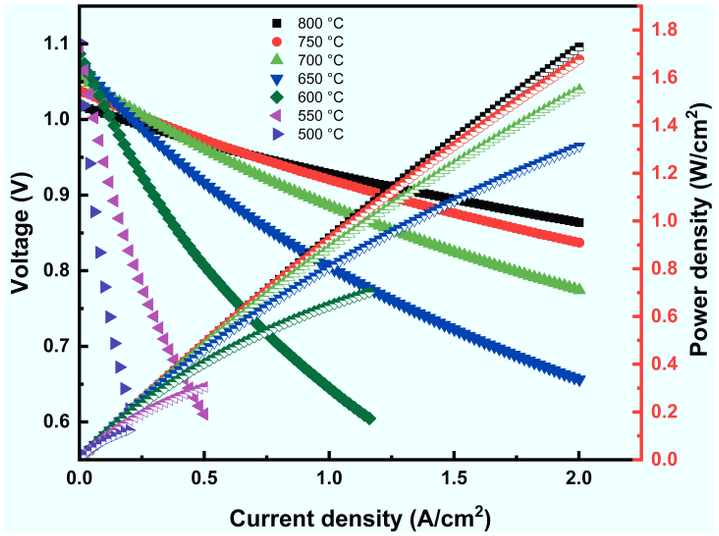

Figure 5.24: Cell voltage and power density as a function of current density.

In addition to the high performance, the measured OCV at all temperature were all above 1 V, an improvement compared to the lower OCV, lower than 0.9 V, observed for the cell without electron blocking layer (seen on page 75). Moreover, compared in Figure 5.25, the measured OCV were close to the Nernst voltage under the same

fuel condition (H_2 with 10 % H_2O). That indicates the strategy to use YSZ as electron blocking layer works effectively.

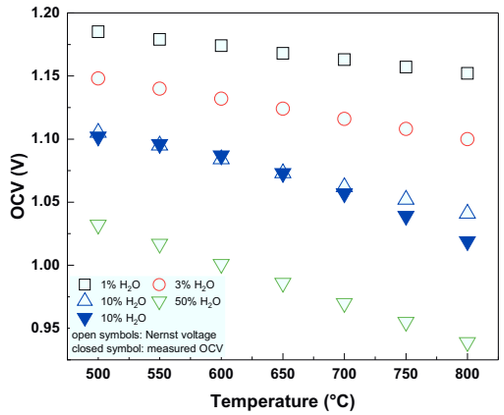

Figure 5.25: The effect of humidity concentration in the fuel on the Nernst voltage and comparison with measured OCV at different temperature

Figure 5.26 shows the EIS (under OCV) of the cell. It shows the cell has low R_o, even at low temperature. For example, at 500 °C, the R_o is only 125.2 $m\Omega\,cm^2$. The extremely low R_o comes from the thin thickness of GDC and its superior ionic conductivity. In addition to that, the low R_o also means that the addition of YSZ electron layer and GDC barrier did not add too much resistance because of their extremely thin thickness and dense microstructure. The detailed values of R_o at other temperature were compared in Table 5.9.

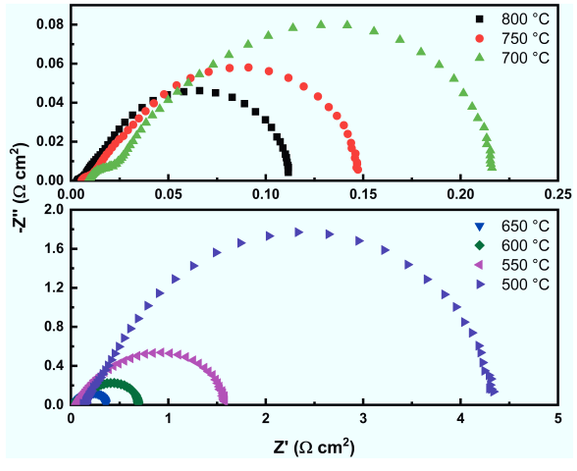

Figure 5.26: Impedance spectra measured from 800 °C to 500 °C

The R_p measured from Figure 5.26 was low at high temperature. At 800 °C, 750 °C, and 700 °C, R_p was only 112.1 $m\Omega\,cm^2$, 145.3 $m\Omega\,cm^2$ and 211.5 $m\Omega\,cm^2$, respectively. However, R_p increased significantly with lower temperature. For instance, at 500 °C R_p increased to 4201 $m\Omega\,cm^2$, more than 30 times larger than R_o. Therefore, R_p should be the reason for the lower performance at lower temperature observed in Figure 5.24.

In Figure 5.27, the area specific resistance for R_o and R_p on temperature is shown in the form of Arrhenius plot. R_p has a larger activation energy (E_a) than R_o (0.94 *eV* compared to 0.88 *eV*), which is consistent with the dominant contribution of R_p observed in Figure 5.26. However, it was also found that while R_o shows a linear behavior in the Arrhenius plot (indicating a single activation energy across the entire temperature range), there is a bending for the dependence of R_p on temperature, marked with a blue dashed line in Figure 5.27 for better visibility. When fitting the low- and high-temperature region separately, an activation energy E_a of 0.57 *eV* and 1.02 *eV* was separately obtained for 800–700 °C and 650–400 °C. One possible explanation for this could be that such bending of R_p is caused by the change of the electronic conductivity of the GDC used in the anode. Wang et al. [159] also reported similar behavior. At a given p_{O_2}, the total conductivity (mainly determined by the electronic conductivity due to the much higher mobility of electrons compared to ions) decreases significantly at low temperature, and the dependence of the total conductivity on reciprocal temperature is also not linear. A total conductivity of 0.96 $S\,cm^{-1}$, 0.2 $S\,cm^{-1}$ and 0.05 $S\,cm^{-1}$ at 900 °C, 800 °C and 700 °C was reported, respectively. However, this needs to be further verified by the separation of anode and cathode resistance from the total R_p, for example using the Distribution Relaxation Time (DRT) analysis of the EIS.

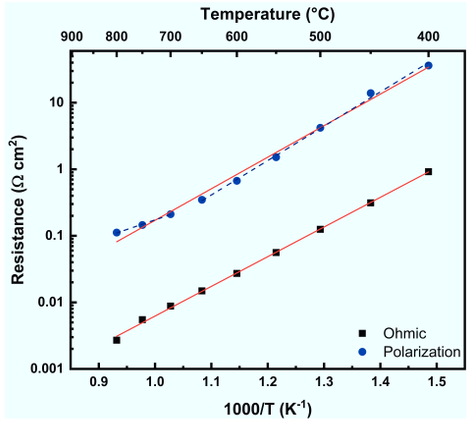

Figure 5.27: Comparison of dependence of area specific resistance for R_o and R_p on temperature

Table 5.9: Comparison of cell performance and resistance at different temperature

Temperature	cell performance			cell resistance	
	OCV	power density		R_o	R_p
		@0.7 V	@2 A cm^{-2}		
°C	V	$W\,cm^{-2}$		$\Omega\,cm^2$	
800	1.019		1.729	0.0027	0.1121
750	1.039		1.676	0.0055	0.1453
700	1.057		1.550	0.0088	0.2115
650	1.073	1.163	1.314	0.0149	0.3482
600	1.087	0.561		0.0272	0.6698
550	1.096	0.250		0.0561	1.5147
500	1.102	0.098		0.1252	4.2013

5.3.2.1 *Comparison with state-of-the-art thin film electrolyte JÜLICH cell*

The difference between the cell fabricated in this work and the state-of-the-art JÜLICH AS-SOFC (for simplicity, it will be called JÜLICH reference cell in the following) with thin film electrolyte is investigated in following section.

First, the composition of anode layer is different. In this work, the anode layer consists of NiO and GDC, while NiO and YSZ is used in the JÜLICH reference cell. The fabrication method is same (both used screen printing), but the microstructure and composition of NiO is different.

Second, the electrolyte is different. In this work, the electrolyte consists of a 3.5 µm GDC fabricated by screen printing and a 600 nm YSZ by PVD, while a 1 µm YSZ fabricated by spin coating is used in the JÜLICH reference cell.

In addition to the listed differences above, all the other layers, including the anode support, barrier layer and cathode layer, are same in terms of composition, fabrication method, microstructure. More details about the JÜLICH reference cell can be found in Han's thesis [168] and publication [38].

Figure 5.28a is the single cell performance comparison. We can observe that at high temperature (800 °C, 750 °C and 700 °C), our cell has a nearly same (or close) performance compared to the JÜLICH reference cell. However, the fuel conditions are different for Figure 5.28a:

our cell is measured by using H_2 with 10 % H_2O while the reference cell uses H_2 with 3 % H_2O. As shown in Figure 5.25, pure H_2 with 3 % H_2O compared to 10 % H_2O will lead to around 50 mV higher Nernst voltage. It means that if measured in the same fuel condition, our cell is expected to have a better performance than the JÜLICH reference cell at temperatures higher than 700 °C. On the other hand, our cell has a worse performance at temperature below 650 °C. Specially, this decreasing performance happens at high current density. For example, at 650 °C and above 0.5 A cm^{-2}, our cell performance is same to the the JÜLICH reference but at a current density above 0.5 A cm^{-2} the performance of ours is worse. Similarly, at 600 °C, at current density higher than 0.25 A cm^{-2}, our cell performance is lower than the JÜLICH reference.

Figure 5.28b shows the cell resistance comparison. Even if the YSZ has an extremely thin thickness of 1 µm, due to its higher resistance, the ASR is still higher than that of 3.5 µm GDC. For example, at 800 °C, the ASR for R_o of YSZ and GDC are 12 mΩ cm^2 and 2.7 mΩ cm^2, respectively; while at 550 °C, the ASR for R_o of YSZ and GDC are 167 mΩ cm^2 and 56.1 mΩ cm^2. In addition to the ohmic resistance comparison, it was also find that the ASR of R_p at OCV for our cell is also lower compared to that of the JÜLICH reference cell, which could be due to the high electronic conductivity of GDC compared to that of YSZ. However, an interesting thing is that although both lower R_p and R_o are observed compared to the JÜLICH reference cell, the cell performance at high current densities is lower. Since Han [168] found that his recorded current density is even higher than the theoretical current density, the high currents could reach the range of 30–45 A for a cathode area of 4 cm×4 cm, therefore, we think that such high current could generate enormous heat. As a result of that, the real cell temperature is significantly higher than the "measured" temperature because of the generated heat, resulting a "measured higher" performance. We assume this could be one of the reasons why the ASR of R_o and R_p of the JÜLICH reference cell are both higher than ours but performance is a little better.

From this comparison in terms of single cell performance and ASR, we can see the advantage of using GDC as electrolyte for SOFC. At 500 °C, 1 µm YSZ is needed to decrease its ASR of R_o, requiring a time consuming technique, spin coating, involving multiple coating, drying and heating treatment. While for GDC, only a single-step screen printing is needed and can provide the same (or better) performance.

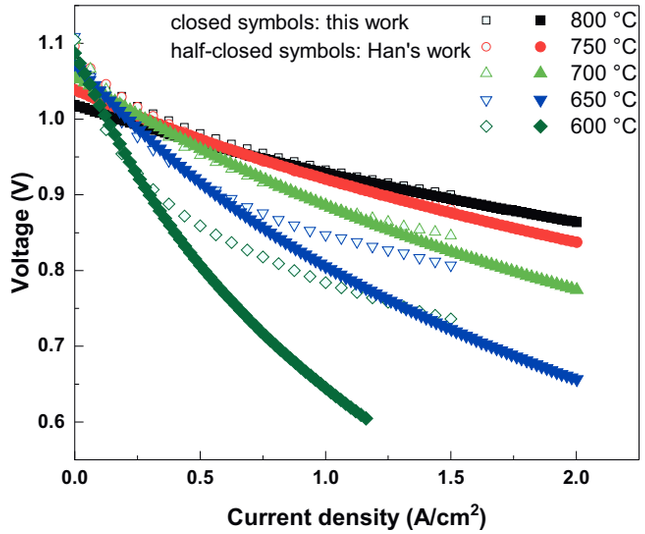

(a) cell performance

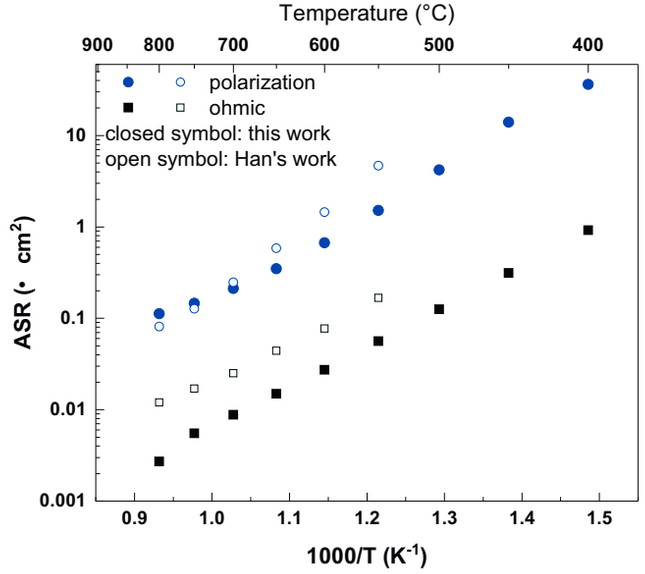

(b) resistance comparison

Figure 5.28: Single cell performance and resistance as a function of temperature

5.3.3 *Single cell test at lower temperature*

In addition to the single cell test at KIT, another test (air, H_2+3 %H_2O) was also done at KIST with identical cell but different reduction temperature due to technical limitations of the setup. The cell was reduced at 650 °C until the monitored OCV reached stabilization. As described in the experiment, ambient air was used as oxygen source and humidified H_2 (3 % H_2O) was used as fuel. The cell voltage was recorded as a function of current density and the power density was also calculated, as shown in Figure 5.29. Compared with the Nernst voltage at each temperature (seen in Figure 5.30), the recorded OCV at each temperature was around 150 mV lower than that. For example, at 650 °C, the OCV was around 0.993 V, instead of 1.076 V. The deviation from the Nernst voltage indicates minor gas leakage in the electrolyte. However, we cannot reliably confirm this point by air leakage rate test due to the mismatch of the cell geometry tested at KIST (2 cm × 2 cm) and the required geometry by our leakage test device (4 cm × 4 cm). In addition to the OCV, the power performance is lower compared to the performance measured at KIT. For example, a recorded powder density, at 0.7 V, of 0.45 $W\,cm^{-2}$, 0.243 $W\,cm^{-2}$, 0.123 $W\,cm^{-2}$ was achieved at 650 °C, 600 °C and 550 °C, respectively. As a comparison, for the cell test at KIT, at 0.7 V, a recorded power density of 1.163 $W\,cm^{-2}$, 0.561 $W\,cm^{-2}$, 0.250 $W\,cm^{-2}$ was achieved at 650 °C, 600 °C and 550 °C, respectively. There are two possible reasons for the lower performance obtained at KIST. First is the lower OCV mentioned before. Second is the smaller area of anode TPB for the cell tested at KIST caused by the lower reduction temperature.

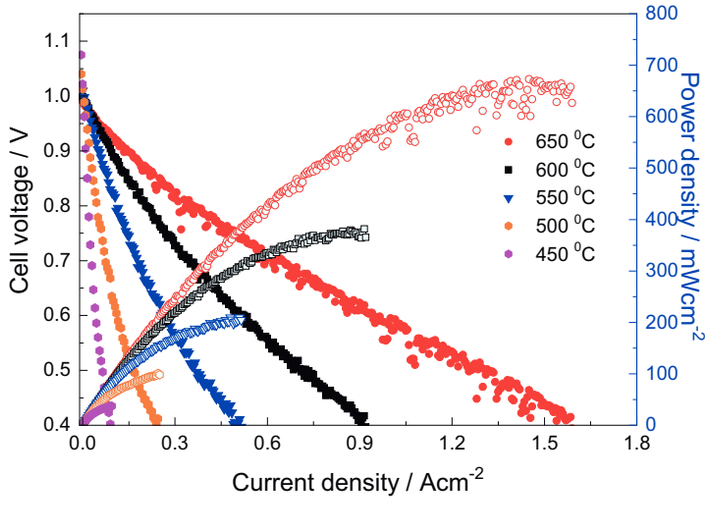

Figure 5.29: Cell voltage and power density as a function of current density

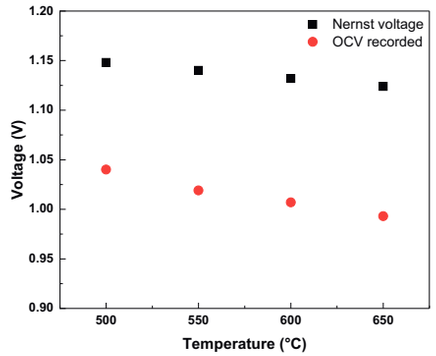

Figure 5.30: Cell voltage as function of temperature

To determine the resistance contribution of the cell, the EIS under OCV was recorded (Figure 5.31). Obviously, R_p increased significantly at low temperature. For example, at 450 °C, R_p reached a value of as high as $13\,\Omega\,cm^2$. As the fuel condition used for the two tests are different (H_2O + 3 % H_2O for KIST and H_2O + 10 % H_2O for KIT), only R_o is compared in Figure 5.32 (since R_p is affected by the humidity in the fuel). It is interesting to see that the ASR_{ohm} is different for the two nearly identical cells. Thus the reason could be the additional higher resistance coming from the test setup, contributing to the total ASR_{ohm}. Through the linear fitting, an activation energy E_a of 0.808 eV for the ASR_{ohm} tested at KIT and 0.566 eV for KIST was obtained, respectively. Compared with the E_a of 0.77 eV, for the ionic conductivity obtained in the GDC bulk ceramic in the previous chapter, it may further indicate that additional resistance exists besides the ohmic resistance for the test in KIST.

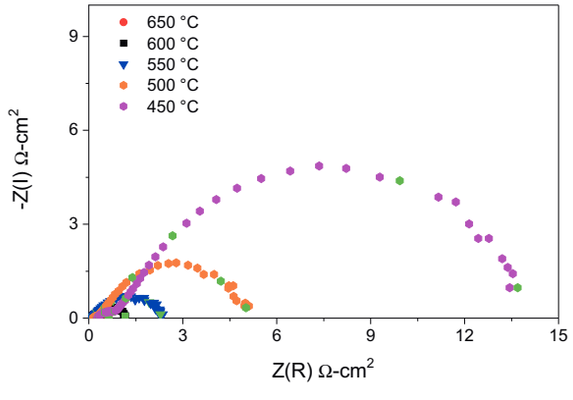

Figure 5.31: Impedance spectra measured from 650 °C to 450 °C

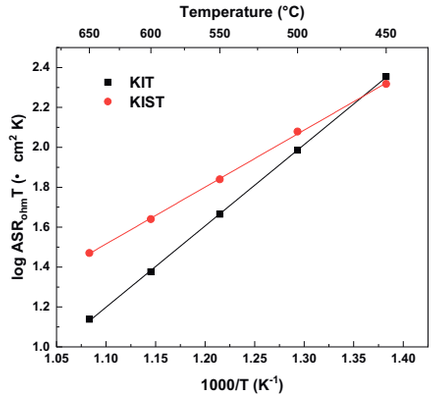

Figure 5.32: Area specific ohmic resistance comparison between KIT and KIST

5.3.4 *Post-test analysis of tested cell*

5.3.4.1 *Topography measurement*

Surface topography of the cell tested at KIT is shown in Figure 5.33. Compared with the same measurement done after sintering, seen in Figure 5.12, the curvature is a little different (the scale bar are same for the two measurements), but there is not severe bending of the cell after testing. As was shown in Figure 5.15, the cell bent severely after reducing due to the expansion caused by the reduction of the GDC electrolyte. In that case, we applied a mechanical load to inhibit the deformation. Here we confirm that in an actual cell test, the deformation of the GDC electrolyte can be effectively inhibited by the testing setup (where the cell is mechanically clamped).

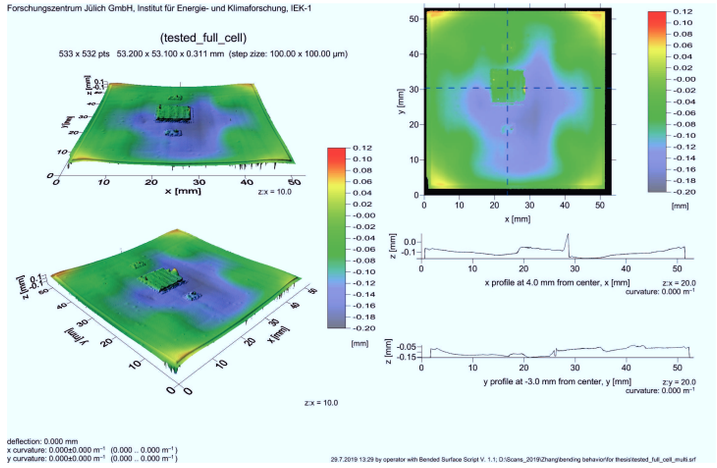

Figure 5.33: Surface topography of the tested full-cell

5.3.4.2 *Laser confocal microscopy*

A laser microscopy was used to check the top-view of the electrolyte surface, shown in Figure 5.34. In a low magnification picture (Figure 5.34b), many "defects" with different morphology were observed on the surface of the electrolyte after the single cell test. An observation at higher resolution was made to determine if the "defect" were holes or agglomerates or dust. For the defect (#1) marked in round shape, they were convex and could be originated from the substrate (Figure 5.34b and Figure 5.34c). For the defect (#2) marked by an ellipse, they were not flat part (Figure 5.34d and Figure 5.34e) and could be caused by the in-homogeneous screen printing of the electrolyte. For the defect (#3) marked by a rectangle, they were concave (Figure 5.34f and Figure 5.34g) and should be some minor holes which were not completely covered by the electrolyte. Therefore, we think that there is still room to improve the quality of the electrolyte paste to achieve a more homogeneous electrolyte with fewer defects.

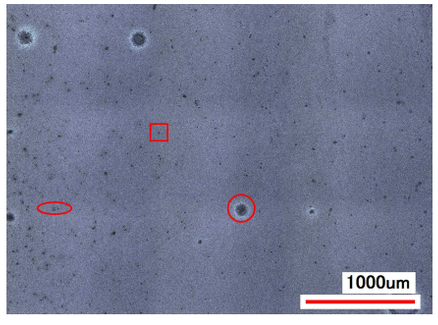

(a) Overview

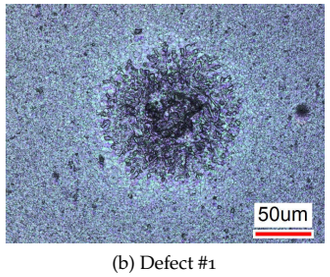

(b) Defect #1

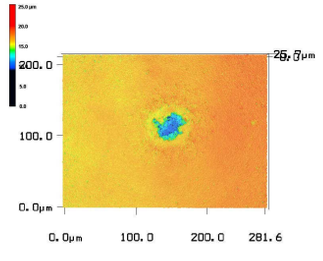

(c) 3D morphology of defect #1

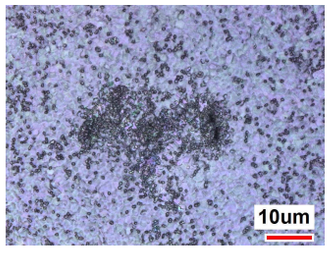

(d) Defect #2

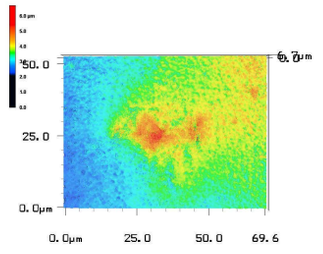

(e) 3D morphology of defect #2

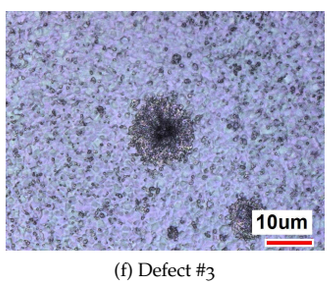

(f) Defect #3

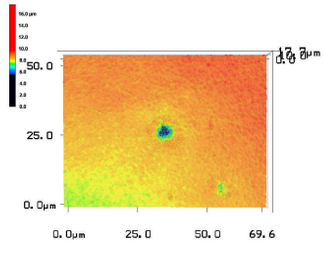

(g) 3D morphology of defect #3

Figure 5.34: Top view of the electrolyte surface for the tested cell by laser microscope

5.3.4.3 *SEM cross-section observation*

Figure 5.35 shows the cross-sectional SEM images of the tested cell at KIT. In low magnification figure (Figure 5.35a), it seems that all the layers maintained their structural integrity after testing. No delamination was observed and each function layer fully and continuously covered the underlying layer. The cracks observed in the cathode layer could be due to the SEM sample preparation. Figure 5.35b shows a cross-sectional microstructure with higher magnification. The cathode layer with thickness around 50 µm adheres tightly to the GDC barrier layer, indicating the good bonding between the LSC cathode and GDC barrier layer can withstand their TEC mismatch. Moreover, there is sufficient porosity in the cathode. Similarly, a strong connection was also observed between the anode and electrolyte probably because GDC was used both in anode and electrolyte. However, it seemed that there was inadequate porosity in the anode and some Ni grains seemed to be agglomerated. Therefore, in the future, the microstructure of the anode still needs to be optimized. Some big holes observed in the interface between anode and substrate is due to the reaction between YSZ and GDC [31]. For a detained observation of the electrolyte (Figure 5.35b), it nearly kept its original structure after the test. Though GDC is easily reduced under reducing atmosphere and as a result chemical expansion of the electrolyte can be expected, the load on top of the cell during the cell test can help to clamp the cell and maintain the integrity of the electrolyte.

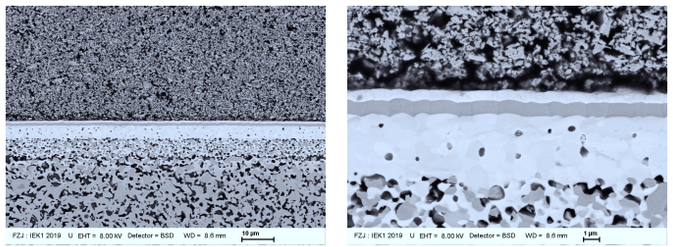

(a) Full cell microstructure (b) Electrolyte microstructure

Figure 5.35: Cross-sectional SEM microstructure of the tested cell

5.4 SOEC PERFORMANCE

5.4.1 *I-V curve*

An SOFC can also be operated in its inverse mode, solid oxide electrolysis cell (SOEC) mode, to evaluate its ability to split water into hydrogen and oxygen. Therefore, a single cell test was carried out that switched

reversibly between SOFC and SOEC mode (rSOC mode), as shown in Figure 5.36. No discontinuity occurred in the shift from fuel cell to electrolysis operation (Figure 5.36a). Like an SOFC mode, high performance was achieved for SOEC mode. For example, at 800 °C and 2 $A\,cm^{-2}$, a voltage of 1.12 V was measured. However, with continued SOEC test at 700 °C, a jump of voltage was observed when the current density was higher than 1.5 $A\,cm^{-2}$. Following that for the SOFC mode, an unexpected decrease of OCV was observed at 700 °C, 1.011 V, compared to 1.018 V at 750 °C (the OCV should increase with lower temperature according to the Nernst equation). Moreover, larger decrease of OCV was observed when the temperature went down to 650 °C. To figure out the reason and exclude the experimental error during the test, a repeated test with identical cell was conducted, shown in Figure 5.36b (note that the humidity ratio of the fuel in SOFC and SOEC mode is different for this test). Similarly, a jump of voltage was observed for a second time at the same temperature, 700 °C for the SOEC mode and the decrease of OCV was also observed at 700 °C compared to 750 °C for SOFC mode. Therefore, we can exclude the experimental error and assume that the jump of voltage in SOEC mode and drop of OCV might be caused by cracks, which will be confirmed by the following SEM check.

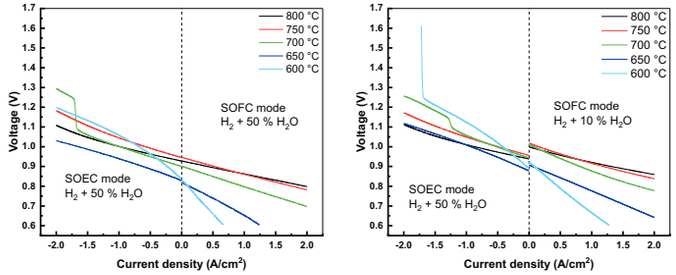

(a) The 1st measurement of I-V curve (b) The 2nd measurement of I-V curve

Figure 5.36: Cell voltage as a function of current density for SOFC and SOEC mode

5.4.2 *SEM observation*

The microstructure of the two cells after the test between SOFC and SOEC were examined in Figure 5.37. As can be found that, unlike the microstructure of the cell only underwent SOFC test (Figure 5.35b), so many cracks were found for both two cells. They were tested in the same conditions, only for different mode. Therefore, the switch between the SOFC and SOEC mode possibly lead to these cracks. The cell test switch between SOFC mode and SOEC mode may change the oxygen partial

pressure (p_{O_2}) at the interfaces between electrolyte and air electrode as well as electrolyte and fuel electrode. When in SOFC mode, GDC is easily reduced under reducing atmosphere. High current densities in SOFC mode will increase the oxygen activity in the electrolyte, whereas high current densities (and electrode over-potentials) in SOEC mode will further lower the oxygen activity in the electrolyte. Moreover, observed jumps happened at the same temperature, 700 °C. This may be due to the fact that the polarization resistance increases significantly at low temperature (the cell test was performed from high temperature to low temperature), which changes the critical P_{O_2} for the oxidization of GDC. In a word, the switch between SOFC and SOEC mode caused GDC electrolyte to cycle between reduction and oxidization, and the resulted expansion and shrinkage leads to the cell damage which resulted in the jump of voltage in SOEC and drop of OCV in SOFC.

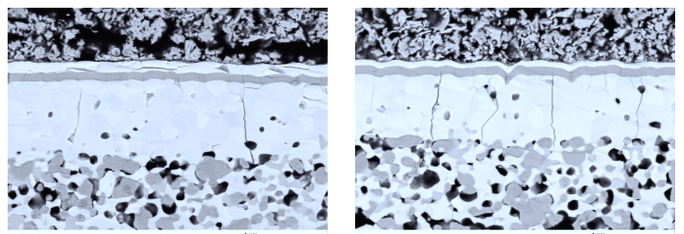

(a) Microstructure of the 1^{st} tested cell (b) Microstructure of the 2^{nd} tested cell

Figure 5.37: Cross-sectional SEM microstructure of the tested cell between SOFC and SOEC mode

5.4.3 *EIS measurement and DRT analysis*

Shown in Figure 5.38 is the EIS comparison under OCV (same fuel and air condition for all of them) for the two tests in SOEC mode and the test only in SOFC mode. It is observed that, before 700 °C, all R_p and R_o are nearly the same no matter if the cell is tested in only SOFC mode or in SOEC mode. However, at 700 °C, both R_p recorded for the SOEC mode decreased by nearly 30 $m\Omega\,cm^2$, more than 25 % decrease compared to R_p in SOFC mode. At the same time, after 700 °C, R_o increased in SOEC mode, compared to only SOFC mode. Moreover, R_p decreased significantly for SOEC mode. To verify the change of R_o and R_p, the distribution of relaxation time (DRT) of corresponding EIS in Figure 5.38 was compared in Figure 5.39 from 800 °C to 550 °C. As can be observed, at 800 °C and 750 °C, the position of the peaks were nearly unchanged, however, at 700 °C, the peaks at position of 10 Hz and 400 Hz for the SOEC mode moved to higher frequencies compared to the peaks of SOFC mode. With lower temperature, such change of the position of the peaks is more obvious. Therefore, we think the

above assumption stands, R_o could increase due to the broken of the electrolyte and then R_p decrease because of the direct contact between oxygen and hydrogen.

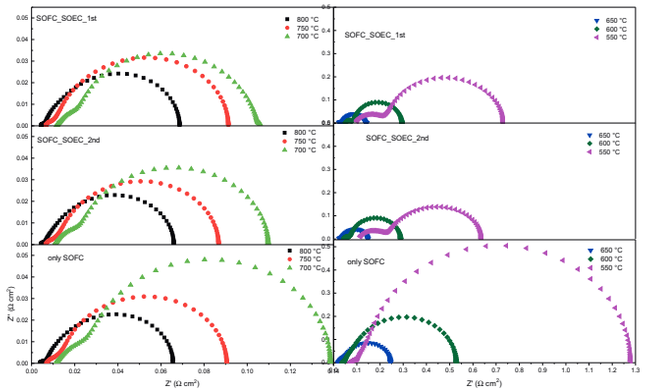

Figure 5.38: EIS comparison of SOFC and SOEC mode

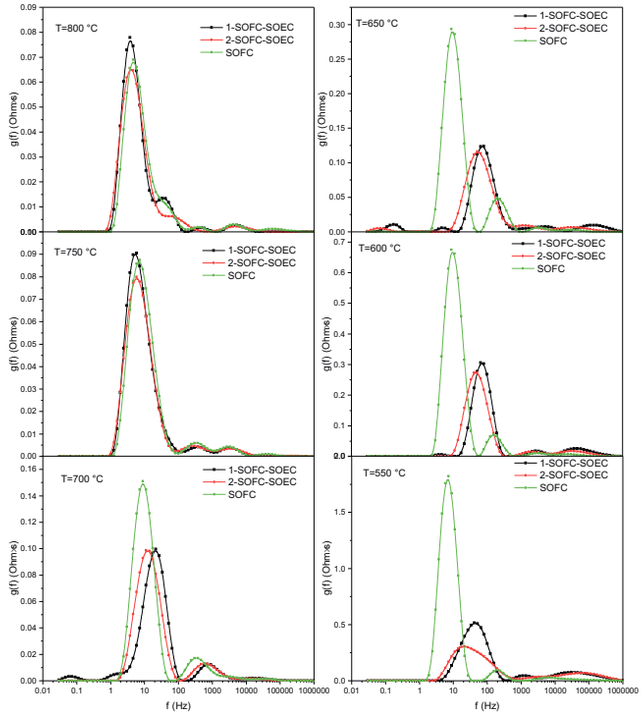

Figure 5.39: DRT comparison at different temperatures

5.5 SUMMARY

In this chapter, we introduce two strategies of using screen printing to fabricate a GDC electrolyte on two different anode layers: NiO/YSZ and NiO/GDC.

For the first strategy, nano-sized GDC is used for the electrolyte to lower the required sintering temperature. However, due to the large specific surface area of the nano-particles, the solid content in the screen printing paste is extremely low and as a result, there are cracks formed after drying. Therefore, a series of pastes with different ratio between solid, binder, solvent, and dispersant content are synthesized. It is found that more binder and higher solid content help to mitigate the cracks forming behavior but there exists a maximum content for them. Finally, after optimizing the dispersant content, a crack-free layer is achieved. After that, to further increase the green density of the screen printed layer, infiltration of GDC suspension is added into the calcined GDC electrolyte layer. However, due to the use of a non-shrinking substrate, a dense GDC electrolyte layer is not achieved after sintering even with infiltration. Therefore, we conclude that a dense electrolyte layer is difficult to obtain via screen printing of nano-sized GDC on a non-shrinking substrate.

For the second strategy, an optimized GDC screen printing paste, which produces a crack-free layer after drying, is obtained by following the standard recipe for YSZ screen printing paste with YSZ powder substituted for GDC powder. The sintering behavior is checked and showed that a thin and dense GDC electrolyte layer is achieved after co-sintering with the NiO/GDC anode layer. Checked by SEM, the thickness is as thin as 3.5 µm. Shown by air leakage rate test of the reduced half-cell, the electrolyte is as dense as "JÜLICH standard half-cell". The following single cell performance shows the full cell with the GDC electrolyte with low OCV and power performance, 0.76 V and 102.4 $mW\,cm^{-2}$ (peak power density) at 650 °C using pure H_2 with 3 % H_2O. We assume the reason for the low OCV is due to the current leakage in the GDC electrolyte. The low performance is caused by the low OCV and a poor adhesion between the cathode and electrolyte (proved by the SEM cross-sectional observation of the tested cell). Therefore, a development of an electron blocking layer is carried out. The single cell performance is measured again and shows that the OCV is successfully increased to close to Nernst voltage, 1.10 V at 500 °C for pure H_2 with 10 % H_2O. A high power density is also achieved (0.84 V at 2 $A\,cm^{-2}$ and 750 °C). EIS shows that a very low ohmic resistance is obtained, only 125.2 $m\Omega\,cm^2$ at 500 °C. The SEM cross-sectional observation for the tested cell shows that no severe delamination or deformation observed after testing. All the interfaces keep their integrity after cell testing. Especially for the electrolyte, no cracks or severe defects are observed after cell testing. For the same cell, its SOEC

performance is also characterized and the result shows a voltage of 1.2 V when a current density of 2 A cm^{-2} is applied at 800 °C. However, a voltage jump is observed with decreasing temperature. Through the microstructure and impedance analysis, the possible reason could be that some cracks happen. The switch between SOFC and SOEC changes the over potentials at the interface between electrolyte and electrodes, caused a switch between oxidized and reduced state of the GDC electrolyte and the electrolyte cracks as a result of that.

6

SUMMARY AND OUTLOOK

SUMMARY

The scope of this work is to find an electrolyte material which is suitable for low temperature SOFC application and explore the corresponding thin film fabrication by screen printing. The challenge is that in literature there are confusing conductivity values for some commonly investigated electrolyte materials and therefore confusion exists about the choice of electrolyte material for low temperature application. A systematical, trustworthy and reliable conductivity comparison thereby has been conducted by controlling some potential effects that could affect the ionic conductivity. Following that, fabrication routes of thin electrolyte on actual substrate have been explored. Characterizations of drying, sintering, reducing behavior and single cell performance have been performed.

Electrolyte material choice

The conductivity values of dense YSZ, ScSZ and GDC ceramics made from well-defined, industrial-grade starting powders have been compared by electrochemical impedance spectroscopy (EIS) from 300 °C to 800 °C. The starting powder properties, powder processing and the ceramic microstructure have all been taken into account and the results have excluded the effects of impurity, agglomeration of raw powder and porosity in the sintered ceramics on conductivity, which are often neglected in other reports. The grain and grain boundary contributions to the conductivity at low temperatures, as well as the total conductivity at typical SOFC operation temperatures have been determined by EIS. The experimental results have been applied into a simple "brick-layer" model to predict the influence of the grain size of an electrolyte on its conductivity. That is an important and often neglected factor for the conductivity of thin electrolyte supported SOFC, which is mandatory for operation at 500 °C. The generic model shows the advantage of using GDC as an electrolyte at low temperature: a 5 µm GDC electrolyte can meet the ASR requirement at 500 °C and that thickness is easily achieved by scale-able techniques such as screen printing or tape casting. Based on this result, the fabrication of thin GDC electrolyte on actual substrate has been performed by screen printing.

Fabrication of thin GDC electrolyte

NiO/YSZ is the state-of-the-art anode, therefore, screen printing of GDC electrolyte on NiO/YSZ anode has been carried out. Due to the inter-diffusion reaction between YSZ and GDC at high co-sintering temperature (> 1200 °C), nano-sized GDC has been used for the screen printing paste to lower the required densification temperature and NiO/YSZ substrate had been fully sintered prior to the GDC fabrication to avoid the following high co-sintering temperature. Because of the high specific surface area of nano-sized GDC, it is difficult to put as much solid content as the micro-sized powder in the screen printing paste and therefore, cracks are observed after drying. After adjusting the paste composition by controlling the solvent, binder and dispersant content, drying cracks have been eliminated. Infiltration of GDC precursor solution in the electrolyte has been carried out after the binder burn-out in order to improve the green density. However, the full densification of GDC electrolyte still fails due to the non-shrinking substrate.

Compared to NiO/YSZ anode, NiO/GDC is under-developed, however, the screen printing of GDC electrolyte can be easier since there is no need to use nano-sized GDC powder and fully sintered NiO/YSZ anode to avoid the inter-diffusion. By adjusting the standard screen printing recipe for YSZ electrolyte developed at IEK-1, a qualified GDC screen printing paste has been achieved. By using that paste, a thin and dense GDC layer has been obtained after sintering at 1400 °C for 5 h, with thickness around 3.5 µm and an acceptable air leakage rate. A following single cell test has been characterized but shows a poor cell performance, partially caused by the current leakage in GDC electrolyte. Additional YSZ electron blocking layer, with thickness around 600 nm, has been developed between the GDC electrolyte and cathode to solve the current leakage problem. The subsequent high cell performance, an OCV of 1.06 V and measured voltage of 0.77 V at a current density of 2 A cm^{-2} and 700 °C (air, H_2+10 % H_2O), confirms the function of the developed YSZ layer. The EIS shows that, compared to 1 µm YSZ, the ohmic resistance is decreased from 167 mΩ cm^2 to 56.1 mΩ cm^2 at 550 °C for a 3.5 µm GDC. Therefore, this part demonstrates a high performance SOFC with GDC electrolyte fabricated by screen printing.

OUTLOOK

For the future work, there are several experiments that should be conducted to further understand the thin electrolyte material choice and fabrication for the SOFC operated at low temperature.

First, the "Brick layer" model developed in this work has to be validated by experiment. A series of thin electrolyte films with different thickness (1–10 μm) should be developed for YSZ, ScSZ and GDC. Different techniques have to be explored for the fabrication of different thickness electrolyte and the corresponding fabrication cost and challenge should be evaluated. For each thickness electrolyte, different microstructure, ranging from single grain to multiple grains (a series of grain size), should be reached by different heat treatment. A series ionic conductivity characterization for these thin film electrolyte should be carried out.

Second, the thin GDC electrolyte development. In this work, a high performance SOFC (5 cm$\times$5 cm), with thin GDC electrolyte, has been demonstrated. However, the cell performance at temperature below 600 °C is still poorer than the state-of-the-art SOFC, even though the ohmic resistance of our cell is much lower. According to the assumption in this work, follow-up work should be continued on the development of the anode layer, in terms of the microstructure (porosity, grain size, TPB), composition (content of NiO and GDC), and thickness. Moreover, future work should scale the cell geometry up to 10 cm $\times$ 10 cm. The larger cells should be assembled into a stack and operated to evaluate the long term stability of such thin GDC electrolyte under stack operation conditions. Furthermore, the cell developed in this work also has a promising SOEC performance. But the problem of the observed cracks should be solved. It is assumed that the switch between SOFC and SOEC mode leads to a change of the electrochemical over-potential and that results in a repeated oxidization and reduction of GDC electrolyte. Further experiment should be carried out to validate that hypothesis and then design a strategy to avoid that.

****

BIBLIOGRAPHY

[1] *BP Statistical Review of World Energy 2018*.

[2] *Global greenhouse gas emissions scenarios*. https://ourworldindata.org/co2-and-other-greenhouse-gas-emissions. Online; accessed 18-Sep.-2019.

[3] R. Peters et al. "Analysis of solid oxide fuel cell system concepts with anode recycling." In: *International Journal of Hydrogen Energy* 38.16 (2013), pp. 6809–6820. DOI: 10.1016/j.ijhydene.2013.03.110.

[4] Z. Gao et al. "A perspective on low-temperature solid oxide fuel cells." In: *Energy & Environmental Science* 9.5 (2016), pp. 1602–1644. DOI: 10.1039/c5ee03858h.

[5] E. D. Wachsman and K. T. Lee. "Lowering the Temperature of Solid Oxide Fuel Cells." In: *Science* 334.6058 (2011), pp. 935–939. DOI: 10.1126/science.1204090.

[6] K. Yoshinori et al. "Extremely high-efficiency thermal power system-solid oxide fuel cell (SOFC) triple combined-cycle system." In: *Mitsubishi Heavy Industries Technical Review* 48.3 (2011), pp. 9–15.

[7] S. Singhal. "Advances in solid oxide fuel cell technology." In: *Solid State Ionics* 135.1-4 (2000), pp. 305–313. DOI: 10.1016/s0167-2738(00)00452-5.

[8] E. Ivers-Tiffée, A. Weber, and D. Herbstritt. "Materials and technologies for SOFC-components." In: *Journal of the European Ceramic Society* 21.10-11 (2001), pp. 1805–1811. DOI: 10.1016/s0955-2219(01)00120-0.

[9] R. M. Ormerod. "Solid oxide fuel cells." In: *Chemical Society Reviews* 32.1 (2002), pp. 17–28. DOI: 10.1039/b105764m.

[10] C. Lenser et al. "Interaction of a ceria-based anode functional layer with a stabilized zirconia electrolyte: Considerations from a materials perspective." In: *Journal of the American Ceramic Society* 101.2 (2018), pp. 739–748. DOI: 10.1111/jace.15214.

[11] A. Tsoga et al. "Gadolinia-doped ceria and yttria stabilized zirconia interfaces: regarding their application for SOFC technology." In: *Acta Materialia* 48.18-19 (2000), pp. 4709–4714. DOI: 10.1016/s1359-6454(00)00261-5.

[12] Y. Larring and M.-L. Fontaine. "Critical Issues of Metal-Supported Fuel Cell." In: *Solid Oxide Fuels Cells: Facts and Figures*. Springer London, 2012, pp. 71–93. DOI: 10.1007/978-1-4471-4456-4_4.

[13] R. Balmer. *Thermodynamics*. West Publishing Company, 1990. ISBN: 9780314470089.

[14] J. Larminie and A. Dicks. *Fuel Cell Systems Explained*. John Wiley & Sons, Ltd, ., 2003. DOI: 10.1002/9781118878330.

[15] I. Pilatowsky et al. *Cogeneration Fuel Cell-Sorption Air Conditioning Systems*. Springer London, 2011. DOI: 10.1007/978-1-84996-028-1.

[16] P. Gellings and H. Bouwmeester. *The CRC Handbook of Solid State Electrochemistry*. Enschede, The Netherlands: CRC Press, 1997. ISBN: 0-8493-8956-9.

[17] S. Chan, K. Khor, and Z. Xia. "A complete polarization model of a solid oxide fuel cell and its sensitivity to the change of cell component thickness." In: *Journal of Power Sources* 93.1-2 (2001), pp. 130–140. DOI: 10.1016/s0378-7753(00)00556-5.

[18] N. Q. Minh. "Ceramic Fuel Cells." In: *Journal of the American Ceramic Society* 76.3 (1993), pp. 563–588. DOI: 10.1111/j.1151-2916.1993.tb03645.x.

[19] O. Büchler et al. "Preparation and properties of thin $La_{1-x}Sr_xCo_{1-y}Fe_yO_{3-\delta}$ perovskitic membranes supported on tailored ceramic substrates." In: *Solid State Ionics* 178.1-2 (2007), pp. 91–99. DOI: 10.1016/j.ssi.2006.11.015.

[20] P. Vozdecky et al. "Properties of tape-cast Y-substituted strontium titanate for planar anode substrates in SOFC applications." In: *Journal of Materials Science* 46.10 (2011), pp. 3493–3499. DOI: 10.1007/s10853-011-5255-8.

[21] W. Schafbauer, N. H. Menzler, and H. P. Buchkremer. "Tape Casting of Anode Supports for Solid Oxide Fuel Cells at Forschungszentrum Jülich." In: *International Journal of Applied Ceramic Technology* 11.1 (2012), pp. 125–135. DOI: 10.1111/j.1744-7402.2012.02839.x.

[22] L. Blum et al. "Solid Oxide Fuel Cell Development at Forschungszentrum Juelich." In: *Fuel Cells* 7.3 (2007), pp. 204–210. DOI: 10.1002/fuce.200600039.

[23] C. Xia and M. Liu. "Microstructures, conductivities, and electrochemical properties of $Ce_{0.9}Gd_{0.1}O_2$ and GDC–Ni anodes for low-temperature SOFCs." In: *Solid State Ionics* 152-153 (2002), pp. 423–430. DOI: 10.1016/s0167-2738(02)00381-8.

[24] S. Zha, W. Rauch, and M. Liu. "Ni-$Ce_{0.9}Gd_{0.1}O_{1.95}$ anode for GDC electrolyte-based low-temperature SOFCs." In: *Solid State Ionics* 166.3-4 (2004), pp. 241–250. DOI: 10.1016/j.ssi.2003.11.012.

[25] H. Uchida, H. Suzuki, and M. Watanabe. "High-Performance Electrode for Medium-Temperature Solid Oxide Fuel Cells." In: *Journal of The Electrochemical Society* 145.2 (1998), p. 615. DOI: 10.1149/1.1838312.

[26] T. Tsai and S. A. Barnett. "Effect of Mixed-Conducting Interfacial Layers on Solid Oxide Fuel Cell Anode Performance." In: *Journal of The Electrochemical Society* 145.5 (1998), p. 1696. DOI: 10.1149/1.1838542.

[27] M. Watanabe, H. Uchida, and M. Yoshida. "Effect of Ionic Conductivity of Zirconia Electrolytes on the Polarization Behavior of Ceria-Based Anodes in Solid Oxide Fuel Cells." In: *Journal of The Electrochemical Society* 144.5 (1997), p. 1739. DOI: 10.1149/1.1837671.

[28] P. Hofmann et al. "Integrating biomass gasification with solid oxide fuel cells: Effect of real product gas tars, fluctuations and particulates on Ni-GDC anode." In: *International Journal of Hydrogen Energy* 33.11 (2008), pp. 2834–2844. DOI: 10.1016/j.ijhydene.2008.03.020.

[29] T. Namioka, T. Naruse, and R. Yamane. "Behavior and mechanisms of Ni/ScSZ cermet anode deterioration by trace tar in wood gas in a solid oxide fuel cell." In: *International Journal of Hydrogen Energy* 36.9 (2011), pp. 5581–5588. DOI: 10.1016/j.ijhydene.2011.01.165.

[30] J. Mermelstein, M. Millan, and N. Brandon. "The impact of carbon formation on Ni–YSZ anodes from biomass gasification model tars operating in dry conditions." In: *Chemical Engineering Science* 64.3 (2009), pp. 492–500. DOI: 10.1016/j.ces.2008.09.020.

[31] H. Jeong. "Coupling a Solid Oxide Fuel Cell with a Biomass Gasifier: Degradation Mechanisms and Alternative Anode Materials." PhD thesis. RWTH Aachen University, 2019. ISBN: 978-3-95806-382-2.

[32] S. B. Adler. "Factors Governing Oxygen Reduction in Solid Oxide Fuel Cell Cathodes†." In: *Chemical Reviews* 104.10 (2004), pp. 4791–4844. DOI: 10.1021/cr020724o.

[33] S. Jiang. "A comparison of O_2 reduction reactions on porous (La,Sr)MnO_3 and (La,Sr)(Co,Fe)O_3 electrodes." In: *Solid State Ionics* 146.1-2 (2002), pp. 1–22. DOI: 10.1016/s0167-2738(01)00997-3.

[34] G. Stochniol, E. Syskakis, and A. Naoumidis. "Chemical Compatibility between Strontium-Doped Lanthanum Manganite and Yttria-Stabilized Zirconia." In: *Journal of the American Ceramic Society* 78.4 (1995), pp. 929–932. DOI: 10.1111/j.1151-2916.1995.tb08416.x.

[35] C. Clausen et al. "Microstructural and microchemical characterization of the interface between $La_{0.85}Sr_{0.15}MnO_3$ and Y_2O_3-stabilized ZrO_2." In: *Solid State Ionics* 70-71 (1994), pp. 59–64. DOI: 10.1016/0167-2738(94)90287-9.

[36] O. Yamamoto et al. "Perovskite-type oxides as oxygen electrodes for high temperature oxide fuel cells." In: *Solid State Ionics* 22.2-3 (1987), pp. 241–246. DOI: 10.1016/0167-2738(87)90039-7.

[37] K. T. Lee and A. Manthiram. "Comparison of $Ln_{0.6}Sr_{0.4}CoO_{3-\delta}$ (Ln=La, Pr, Nd, Sm, and Gd) as Cathode Materials for Intermediate Temperature Solid Oxide Fuel Cells." In: *Journal of The Electrochemical Society* 153.4 (2006), A794. DOI: 10.1149/1.2172572.

[38] F. Han et al. "Novel high-performance solid oxide fuel cells with bulk ionic conductance dominated thin-film electrolytes." In: *Journal of Power Sources* 218 (2012), pp. 157–162. DOI: 10.1016/j.jpowsour.2012.06.087.

[39] Z. Shao and S. M. Haile. "A high-performance cathode for the next generation of solid-oxide fuel cells." In: *Nature* 431.7005 (2004), pp. 170–173. DOI: 10.1038/nature02863.

[40] Z. Shao et al. "A thermally self-sustained micro solid-oxide fuel-cell stack with high power density." In: *Nature* 435.7043 (2005), pp. 795–798. DOI: 10.1038/nature03673.

[41] Z. Shao et al. "Investigation of the permeation behavior and stability of a $Ba_{0.5}Sr_{0.5}Co_{0.8}Fe_{0.2}O_{3-\delta}$ oxygen membrane." In: *Journal of Membrane Science* 172.1-2 (2000), pp. 177–188. DOI: 10.1016/s0376-7388(00)00337-9.

[42] K. Efimov, Q. Xu, and A. Feldhoff. "Transmission Electron Microscopy Study of $Ba_{0.5}Sr_{0.5}Co_{0.8}Fe_{0.2}O_{3-\delta}$ Perovskite Decomposition at Intermediate Temperatures." In: *Chemistry of Materials* 22.21 (2010), pp. 5866–5875. DOI: 10.1021/cm101745v.

[43] P. Müller et al. "Decomposition pathway of cubic $Ba_{0.5}Sr_{0.5}Co_{0.8}Fe_{0.2}O_{3-\delta}$ between 700 °C and 1000 °C analyzed by electron microscopic techniques." In: *Solid State Ionics* 206 (2012), pp. 57–66. DOI: 10.1016/j.ssi.2011.10.013.

[44] M. Arnold et al. "Correlation of the Formation and the Decomposition Process of the BSCF Perovskite at Intermediate Temperatures." In: *Chemistry of Materials* 20.18 (2008), pp. 5851–5858. DOI: 10.1021/cm801463h.

[45] J. Kilner. "Fast oxygen transport in acceptor doped oxides." In: *Solid State Ionics* 129.1-4 (2000), pp. 13–23. DOI: 10.1016/s0167-2738(99)00313-6.

[46] D. Y. Wang et al. "Oxygen-ion conductivity and defect interactions in yttria-doped ceria☆." In: *Solid State Ionics* 2.2 (1981), pp. 95–105. DOI: 10.1016/0167-2738(81)90005-9.

[47] U. of Cambridge. *Yttria-stabilized zirconia (YSZ) crystal structure*. https://www.doitpoms.ac.uk/tlplib/fuel-cells/printall.php. Online; accessed 15-August-2019.

[48] X. Guo and J. Maier. "Grain Boundary Blocking Effect in Zirconia: A Schottky Barrier Analysis." In: *Journal of The Electrochemical Society* 148.3 (2001), E121. DOI: 10.1149/1.1348267.

[49] X. Guo. "Physical origin of the intrinsic grain-boundary resistivity of stabilized-zirconia: Role of the space-charge layers." In: *Solid State Ionics* 81.3-4 (1995), pp. 235–242. DOI: 10.1016/0167-2738(95)00180-e.

[50] T. H. Etsell and S. N. Flengas. "Electrical properties of solid oxide electrolytes." In: *Chemical Reviews* 70.3 (1970), pp. 339–376. DOI: 10.1021/cr60265a003.

[51] B. Steele. "Oxygen transport and exchange in oxide ceramics." In: *Journal of Power Sources* 49.1-3 (1994), pp. 1–14. DOI: 10.1016/0378-7753(93)01789-k.

[52] J. B. Goodenough. "Oxide-Ion Electrolytes." In: *Annual Review of Materials Research* 33.1 (2003), pp. 91–128. DOI: 10.1146/annurev.matsci.33.022802.091651.

[53] H. G. Scott. "Phase relationships in the zirconia-yttria system." In: *Journal of Materials Science* 10.9 (1975), pp. 1527–1535. DOI: 10.1007/bf01031853.

[54] D.-S. Lee et al. "Characterization of ZrO_2 co-doped with Sc_2O_3 and CeO_2 electrolyte for the application of intermediate temperature SOFCs." In: *Solid State Ionics* 176.1-2 (2005), pp. 33–39. DOI: 10.1016/j.ssi.2004.07.013.

[55] V. Kharton, F. Marques, and A. Atkinson. "Transport properties of solid oxide electrolyte ceramics: a brief review." In: *Solid State Ionics* 174.1-4 (2004), pp. 135–149. DOI: 10.1016/j.ssi.2004.06.015.

[56] J. A. Kilner and M. Burriel. "Materials for Intermediate-Temperature Solid-Oxide Fuel Cells." In: *Annual Review of Materials Research* 44.1 (2014), pp. 365–393. DOI: 10.1146/annurev-matsci-070813-113426.

[57] M. Kurumada, H. Hara, and E. Iguchi. "Oxygen vacancies contributing to intragranular electrical conduction of yttria-stabilized zirconia (YSZ) ceramics." In: *Acta Materialia* 53.18 (2005), pp. 4839–4846. DOI: 10.1016/j.actamat.2005.06.027.

[58] T. Ishii. "Structural phase transition and ionic conductivity in 0.88 ZrO_2–(ů $_{12}$–x)Sc_2O_3–xAl_2O_3." In: *Solid State Ionics* 78.3-4 (1995), pp. 333–338. DOI: 10.1016/0167-2738(95)00118-p.

[59] H. Yamamura et al. "Electrical conductivity in the system ZrO_2–Y_2O_3–Sc_2O_3." In: *Solid State Ionics* 107.3-4 (1998), pp. 185–189. DOI: 10.1016/s0167-2738(97)00534-1.

[60] S. Badwal et al. "An investigation of conductivity, microstructure and stability of electrolyte compositions in the system 9 mol % (Sc_2O_3–Y_2O_3)–ZrO_2(Al_2O_3)." In: *Solid State Ionics* 109.3-4 (1998), pp. 167–186. DOI: 10.1016/s0167-2738(98)00079-4.

[61] K. Nomura et al. "Aging and Raman scattering study of scandia and yttria doped zirconia." In: *Solid State Ionics* 132.3-4 (2000), pp. 235–239. DOI: 10.1016/s0167-2738(00)00648-2.

[62] Y. Arachi et al. "Electrical Conductivity of ZrO_2–Sc_2O_3 Doped with HfO_2, CeO_2, and Ga_2O_3." In: *Journal of The Electrochemical Society* 148.5 (2001), A520. DOI: 10.1149/1.1366622.

[63] B. C. H. Steele. "Appraisal of $Ce_{1-y}Gd_yO_{2-y/2}$ electrolytes for IT-SOFC operation at 500 °C." In: *Solid State Ionics* 129.1-4 (2000), pp. 95–110. DOI: 10.1016/s0167-2738(99)00319-7.

[64] M. Mogensen, N. M. Sammes, and G. A. Tompsett. "Physical, chemical and electrochemical properties of pure and doped ceria." In: *Solid State Ionics* 129.1-4 (2000), pp. 63–94. DOI: 10.1016/s0167-2738(99)00318-5.

[65] C. Xia and M. Liu. "Low-temperature SOFCs based on $Gd_{0.1}Ce_{0.9}O_{1.95}$ fabricated by dry pressing." In: *Solid State Ionics* 144.3-4 (2001), pp. 249–255. DOI: 10.1016/s0167-2738(01)00980-8.

[66] R. Doshi et al. "Development of Solid-Oxide Fuel Cells That Operate at 500 °C." In: *Journal of The Electrochemical Society* 146.4 (1999), p. 1273. DOI: 10.1149/1.1391758.

[67] S. Zha et al. "GDC-Based Low-Temperature SOFCs Powered by Hydrocarbon Fuels." In: *Journal of The Electrochemical Society* 151.8 (2004), A1128. DOI: 10.1149/1.1764566.

[68] A. J. Jacobson. "Materials for Solid Oxide Fuel Cells†." In: *Chemistry of Materials* 22.3 (2010), pp. 660–674. DOI: 10.1021/cm902640j.

[69] C. Lenser et al. "Interaction of a ceria-based anode functional layer with a stabilized zirconia electrolyte: Considerations from a materials perspective." In: *Journal of the American Ceramic Society* 101.2 (2017), pp. 739–748. DOI: 10.1111/jace.15214.

[70] N. Sammes, G. Tompsett, and Z. Cai. "The chemical reaction between ceria and fully stabilised zirconia." In: *Solid State Ionics* 121.1-4 (1999), pp. 121–125. DOI: 10.1016/s0167-2738(98)00538-4.

[71] G. A. Tompsett, N. M. Sammes, and O. Yamamoto. "Ceria-Yttria-Stabilized Zirconia Composite Ceramic Systems for Applications as Low-Temperature Electrolytes." In: *Journal of the American Ceramic Society* 80.12 (2005), pp. 3181–3186. DOI: 10.1111/j.1151-2916.1997.tb03247.x.

[72] K. L. Duncan, K.-T. Lee, and E. D. Wachsman. "Dependence of open-circuit potential and power density on electrolyte thickness in solid oxide fuel cells with mixed conducting electrolytes." In: *Journal of Power Sources* 196.5 (2011), pp. 2445–2451. DOI: 10.1016/j.jpowsour.2010.10.034.

[73] B. C. H. Steele. "Material science and engineering: The enabling technology for the commercialisation of fuel cell systems." In: *Journal of Materials Science* 36.5 (2001), pp. 1053–1068. DOI: 10.1023/a:1004853019349.

[74] H. Hayashi et al. "Thermal expansion of Gd-doped ceria and reduced ceria." In: *Solid State Ionics* 132.3-4 (2000), pp. 227–233. DOI: 10.1016/s0167-2738(00)00646-9.

[75] A. Atkinson. "Chemically-induced stresses in gadolinium-doped ceria solid oxide fuel cell electrolytes." In: *Solid State Ionics* 95.3-4 (1997), pp. 249–258. DOI: 10.1016/s0167-2738(96)00588-7.

[76] T. Kudo and H. Obayashi. "Mixed Electrical Conduction in the Fluorite-Type $Ce_{1-x}Gd_xO_{2-x/2}$." In: *Journal of The Electrochemical Society* 123.3 (1976), p. 415. DOI: 10.1149/1.2132840.

[77] T. Ishihara, H. Matsuda, and Y. Takita. "Doped $LaGaO_3$ Perovskite Type Oxide as a New Oxide Ionic Conductor." In: *Journal of the American Chemical Society* 116.9 (1994), pp. 3801–3803. DOI: 10.1021/ja00088a016.

[78] T. Ishihara et al. "Recent progress in $LaGaO_3$ based solid electrolyte for intermediate temperature SOFCs." In: *Solid State Ionics* 177.19-25 (2006), pp. 1949–1953. DOI: 10.1016/j.ssi.2006.01.044.

[79] P. Majewski, M. Rozumek, and F. Aldinger. "Phase diagram studies in the systems La_2O_3–SrO–MgO–Ga_2O_3 at 1350–1400 °C in air with emphasis on Sr and Mg substituted $LaGaO_3$." In: *Journal of Alloys and Compounds* 329.1-2 (2001), pp. 253–258. DOI: 10.1016/s0925-8388(01)01583-3.

[80] T. Ishihara, H. Matsuda, and Y. Takita. "Effects of rare earth cations doped for La site on the oxide ionic conductivity of $LaGaO_3$-based perovskite type oxide." In: *Solid State Ionics* 79 (1995), pp. 147–151. DOI: 10.1016/0167-2738(95)00054-a.

[81] J. W. Fergus. "Electrolytes for solid oxide fuel cells." In: *Journal of Power Sources* 162.1 (2006), pp. 30–40. DOI: 10.1016/j.jpowsour.2006.06.062.

[82] S. Badwal. "Stability of solid oxide fuel cell components." In: *Solid State Ionics* 143.1 (2001), pp. 39–46. DOI: 10.1016/s0167-2738(01)00831-1.

[83] J. W. Yan et al. "Fabrication and Testing of a Doped Lanthanum Gallate Electrolyte Thin-Film Solid Oxide Fuel Cell." In: *Journal of The Electrochemical Society* 149.9 (2002), A1132. DOI: 10.1149/1.1496485.

[84] M. Shi et al. "Preparation of electrolyte foils $La_{0.85}Sr_{0.15}Ga_{0.85}Mg_{0.15}O_{2.85}$ (LSGM) by means of tape casting." In: *Journal of Materials Processing Technology* 169.2 (2005), pp. 179–183. DOI: 10.1016/j.jmatprotec.2005.04.093.

[85] P. Huang, A. Horky, and A. Petric. "Interfacial Reaction between Nickel Oxide and Lanthanum Gallate during Sintering and its Effect on Conductivity." In: *Journal of the American Ceramic Society* 82.9 (1999), pp. 2402–2406. DOI: 10.1111/j.1151-2916.1999.tb02096.x.

[86] P. Shuk et al. "Oxide ion conducting solid electrolytes based on Bi_2O_3." In: *Solid State Ionics* 89.3-4 (1996), pp. 179–196. DOI: 10.1016/0167-2738(96)00348-7.

[87] H. Harwig and A. Gerards. "Electrical properties of the α, β, γ, and δ phases of bismuth sesquioxide." In: *Journal of Solid State Chemistry* 26.3 (1978), pp. 265–274. DOI: 10.1016/0022-4596(78)90161-5.

[88] N. Sammes et al. "Bismuth based oxide electrolytes— structure and ionic conductivity." In: *Journal of the European Ceramic Society* 19.10 (1999), pp. 1801–1826. DOI: 10.1016/s0955-2219(99)00009-6.

[89] A. M. Azad, S. Larose, and S. A. Akbar. "Bismuth oxide-based solid electrolytes for fuel cells." In: *Journal of Materials Science* 29.16 (1994), pp. 4135–4151. DOI: 10.1007/bf00414192.

[90] A. A. Yaremchenko et al. "Oxygen ionic transport in Bi_2O_3 -based oxides: II. The Bi_2O_3 -ZrO_2 -Y_2O_3 and Bi_2O_3 -Nb_2O_5 -Ho_2O_3 solid solutions." In: *Journal of Solid State Electrochemistry* 2.5 (1998), pp. 308–314. DOI: 10.1007/s100080050105.

[91] N. Jiang, E. D. Wachsman, and S.-H. Jung. "A higher conductivity Bi_2O_3-based electrolyte." In: *Solid State Ionics* 150.3-4 (2002), pp. 347–353. DOI: 10.1016/s0167-2738(02)00291-6.

[92] E. D. Wachsman et al. "Stable High Conductivity Ceria/Bismuth Oxide Bilayered Electrolytes." In: *Journal of The Electrochemical Society* 144.1 (1997), p. 233. DOI: 10.1149/1.1837390.

[93] J. S. Ahn et al. "High-performance bilayered electrolyte intermediate temperature solid oxide fuel cells." In: *Electrochemistry Communications* 11.7 (2009), pp. 1504–1507. DOI: 10.1016/j.elecom.2009.05.041.

[94] M. R. Somalu and N. P. Brandon. "Rheological Studies of Nickel/Scandia-Stabilized-Zirconia Screen Printing Inks for Solid Oxide Fuel Cell Anode Fabrication." In: *Journal of the American Ceramic Society* 95.4 (2011). Ed. by R. Koc, pp. 1220–1228. DOI: 10.1111/j.1551-2916.2011.05014.x.

[95] J. H. Sung et al. "Effect of particle size in Ni screen printing paste of incompatible polymer binders." In: *Journal of Materials Science* 45.9 (2010), pp. 2466–2473. DOI: 10.1007/s10853-010-4218-9.

[96] P. Ried et al. "Processing of YSZ screen printing pastes and the characterization of the electrolyte layers for anode supported SOFC." In: *Journal of the European Ceramic Society* 28.9 (2008), pp. 1801–1808. DOI: 10.1016/j.jeurceramsoc.2007.11.018.

[97] P. V. Dollen and S. Barnett. "A Study of Screen Printed Yttria-Stabilized Zirconia Layers for Solid Oxide Fuel Cells." In: *Journal of the American Ceramic Society* 88.12 (2005), pp. 3361–3368. DOI: 10.1111/j.1551-2916.2005.00625.x.

[98] J. W. Phair. "Rheological Analysis of Concentrated Zirconia Pastes with Ethyl Cellulose for Screen Printing SOFC Electrolyte Films." In: *Journal of the American Ceramic Society* 91.7 (2008), pp. 2130–2137. DOI: 10.1111/j.1551-2916.2008.02443.x.

[99] R. Mücke et al. "Cofiring of thin zirconia films during SOFC manufacturing." In: *Journal of the American Ceramic Society* 92 (2009), S95–S102. DOI: 10.1111/j.1551-2916.2008.02707.x.

[100] A. Bhatti and P. Farries. "Preparation of Long-fiber-reinforced Dense Glass and Ceramic Matrix Composites." In: *Comprehensive Composite Materials*. Elsevier, 2000, pp. 645–667. DOI: 10.1016/b0-08-042993-9/00107-8.

[101] E.-O. Oh et al. "Extremely Thin Bilayer Electrolyte for Solid Oxide Fuel Cells (SOFCs) Fabricated by Chemical Solution Deposition (CSD)." In: *Advanced Materials* 24.25 (2012), pp. 3373–3377. DOI: 10.1002/adma.201200505.

[102] K. J. Skrobis, D. D. Denton, and A. V. Skrobis. "Effect of early solvent evaporation on the mechanism of the spin-coating of polymeric solutions." In: *Polymer Engineering and Science* 30.3 (1990), pp. 193–196. DOI: 10.1002/pen.760300309.

[103] B. T. Chen. "Investigation of the solvent-evaporation effect on spin coating of thin films." In: *Polymer Engineering and Science* 23.7 (1983), pp. 399–403. DOI: 10.1002/pen.760230706.

[104] J. H. Lai. "An investigation of spin coating of electron resists." In: *Polymer Engineering and Science* 19.15 (1979), pp. 1117–1121. DOI: 10.1002/pen.760191509.

[105] L. L. Spangler, J. M. Torkelson, and J. S. Royal. "Influence of solvent and molecular weight on thickness and surface topography of spin-coated polymer films." In: *Polymer Engineering and Science* 30.11 (1990), pp. 644–653. DOI: 10.1002/pen.760301104.

[106] J. L. Roux and D. Paul. "Preparation of composite membranes by a spin coating process." In: *Journal of Membrane Science* 74.3 (1992), pp. 233–252. DOI: 10.1016/0376-7388(92)80064-q.

[107] B. S. Yilbas, A. Al-Sharafi, and H. Ali. "Surfaces for Self-Cleaning." In: *Self-Cleaning of Surfaces and Water Droplet Mobility*. Elsevier, 2019, pp. 45–98. DOI: 10.1016/b978-0-12-814776-4.00003-3.

[108] A. Babaluo et al. "A modified model for alumina membranes formed by gel-casting followed by dip-coating." In: *Journal of the European Ceramic Society* 24.15-16 (2004), pp. 3779–3787. DOI: 10.1016/j.jeurceramsoc.2004.01.007.

[109] O. Guillon, L. Weiler, and J. Rödel. "Anisotropic Microstructural Development During the Constrained Sintering of Dip-Coated Alumina Thin Films." In: *Journal of the American Ceramic Society* 90.5 (2007), pp. 1394–1400. DOI: 10.1111/j.1551-2916.2007.01565.x.

[110] I. A. Neacşu et al. "Inorganic micro- and nanostructured implants for tissue engineering." In: *Nanobiomaterials in Hard Tissue Engineering*. Elsevier, 2016, pp. 271–295. DOI: 10.1016/b978-0-323-42862-0.00009-2.

[111] T. Tsai and S. A. Barnett. "Bias Sputter Deposition of Dense Yttria-Stabilized Zirconia Films on Porous Substrates." In: *Journal of The Electrochemical Society* 142.9 (1995), p. 3084. DOI: 10.1149/1.2048692.

[112] N. Jordan et al. "$Ce_{0.8}Gd_{0.2}O_{2-\delta}$ protecting layers manufactured by physical vapor deposition for IT-SOFC." In: *Solid State Ionics* 179.21-26 (2008), pp. 919–923. DOI: 10.1016/j.ssi.2007.12.008.

[113] R. Nédélec et al. "Dense yttria-stabilised zirconia electrolyte layers for SOFC by reactive magnetron sputtering." In: *Journal of Power Sources* 205 (2012), pp. 157–163. DOI: 10.1016/j.jpowsour.2012.01.054.

[114] S. Uhlenbruck et al. "Electrode and Electrolyte Layers for Solid Oxide Fuel Cells Applied by Physical Vapor Deposition (PVD)." In: ECS, 2011. DOI: 10.1149/1.3570223.

[115] M. Haydn et al. "Multi-layer thin-film electrolytes for metal supported solid oxide fuel cells." In: *Journal of Power Sources* 256 (2014), pp. 52–60. DOI: 10.1016/j.jpowsour.2014.01.043.

[116] S. E. Veyo et al. "Tubular Solid Oxide Fuel Cell/Gas Turbine Hybrid Cycle Power Systems: Status." In: *Journal of Engineering for Gas Turbines and Power* 124.4 (2000), pp. 845–849. DOI: 10.1115/1.1473148.

[117] T.-H. Yeh, W.-C. Hsu, and C.-C. Chou. "Mechanical and electrical properties of ZrO_2 (3Y) doped with $RENbO_4$ (RE = Yb, Er, Y, Dy, YNd, Sm, Nd)." In: *Journal de Physique IV (Proceedings)* 128 (2005), pp. 213–219. DOI: 10.1051/jp4:2005128032.

[118] D. W. Jung, K. L. Duncan, and E. D. Wachsman. "Effect of total dopant concentration and dopant ratio on conductivity of $(DyO_{1.5})_x$–$(WO_3)_y$–$(BiO_{1.5})_{1-x-y}$." In: *Acta Materialia* 58.2 (2010), pp. 355–363. DOI: 10.1016/j.actamat.2009.08.072.

[119] A. Kumar et al. "Oxygen-ion conduction in scandia-stabilized zirconia-ceria solid electrolyte ($x\,Sc_2O_3$-$1\,CeO_2$-$(_{99}-x)ZrO_2$, $5 \leqslant x \leqslant 11$)." In: *Journal of the American Ceramic Society* 100.2 (2016), pp. 659–668. DOI: 10.1111/jace.14595.

[120] D. J. L. Brett et al. "Intermediate temperature solid oxide fuel cells." In: *Chemical Society Reviews* 37.8 (2008), p. 1568. DOI: 10.1039/b612060c.

[121] B. C. H. Steele and A. Heinzel. "Materials for fuel-cell technologies." In: *Nature* 414.6861 (2001), pp. 345–352. DOI: 10.1038/35104620.

[122] Y. Zhang et al. "Recent Progress on Advanced Materials for Solid-Oxide Fuel Cells Operating Below 500 °C." In: *Advanced Materials* 29.48 (2017), p. 1700132. DOI: 10.1002/adma.201700132.

[123] L. Malavasi, C. A. J. Fisher, and M. S. Islam. "Oxide-ion and proton conducting electrolyte materials for clean energy applications: structural and mechanistic features." In: *Chemical Society Reviews* 39.11 (2010), p. 4370. DOI: 10.1039/b915141a.

[124] O. Bohnke et al. "Ionic and electronic conductivity of 3 mol% Fe_2O_3-substituted cubic yttria-stabilized ZrO_2 (YSZ) and scandia-stabilized ZrO_2 (ScSZ)." In: *Solid State Ionics* 262 (), pp. 517–521. DOI: 10.1016/j.ssi.2013.11.003.

[125] W. Sun et al. "Preparation of dual-pore anode supported Sc_2O_3-stabilized-ZrO_2 electrolyte planar solid oxide fuel cell by phase-inversion and dip-coating." In: *Journal of Power Sources* 218 (2012), pp. 352–356. DOI: 10.1016/j.jpowsour.2012.06.107.

[126] N. Mahato et al. "Progress in material selection for solid oxide fuel cell technology: A review." In: *Progress in Materials Science* 72 (2015), pp. 141–337. DOI: 10.1016/j.pmatsci.2015.01.001.

[127] K. C. Wincewicz and J. S. Cooper. "Taxonomies of SOFC material and manufacturing alternatives." In: *Journal of Power Sources* 140.2 (2005), pp. 280–296. DOI: 10.1016/j.jpowsour.2004.08.032.

[128] S. Singhal. "Solid oxide fuel cells for stationary, mobile, and military applications." In: *Solid State Ionics* 152-153 (2002), pp. 405–410. DOI: 10.1016/s0167-2738(02)00349-1.

[129] T. Mori et al. "Influence of particle morphology on nanostructural feature and conducting property in Sm-doped CeO_2 sintered body." In: *Solid State Ionics* 175.1-4 (2004), pp. 641–649. DOI: 10.1016/j.ssi.2004.09.046.

[130] X. Chen et al. "Influence of microstructure on the ionic conductivity of yttria-stabilized zirconia electrolyte." In: *Materials Science and Engineering: A* 335.1-2 (2002), pp. 246–252. DOI: 10.1016/s0921-5093(01)01935-9.

[131] X. Guo and R. Waser. "Electrical properties of the grain boundaries of oxygen ion conductors: Acceptor-doped zirconia and ceria." In: *Progress in Materials Science* 51.2 (2006), pp. 151–210. DOI: 10.1016/j.pmatsci.2005.07.001.

[132] J. R. M. Evgenij Barsoukov. *Impedance Spectroscopy: Theory, Experiment, and Applications*. Wiley, 2018. ISBN: 9781119333180.

[133] G. instruments. *Basics of Electrochemical Impedance Spectroscopy*. https://www.gamry.com/application-notes/EIS/basics-of-electrochemical-impedance-spectroscopy/. Online; accessed 03-July-2019.

[134] J. T. S. Irvine, D. C. Sinclair, and A. R. West. "Electroceramics: Characterization by Impedance Spectroscopy." In: *Advanced Materials* 2.3 (1990), pp. 132–138. DOI: 10.1002/adma.19900020304.

[135] C. W. Macosko and R. G. Larson. *Rheology: principles, measurements, and applications*. Vch New York, 1994. ISBN: 978-0-471-18575-8.

[136] D. Tsoukleris et al. "2-Ethyl-1-hexanol based screen-printed titania thin films for dye-sensitized solar cells." In: *Solar Energy* 79.4 (2005), pp. 422–430. DOI: 10.1016/j.solener.2005.02.017.

[137] F. J. IEK-1. *Detail of Ekra screen printer*. https://www.fz-juelich.de/iek/iek-1/EN/Expertise/HerstellungsverfahrenGeraete/Pulvertechnologie.html. Online; accessed 01-July-2019.

[138] R. Mücke. "Sinterung von Zirkoniumdioxid- Elektrolyten im Mehrlagenverbund der oxidkeramischen Brennstoffzelle (SOFC)." PhD thesis. Ruhr-Universität Bochum, 2007. ISBN: 978-3-89336-529-6.

[139] F.-I. f. S. I. Center of Device Development. *Technical Data of TOMMI plus*. https://www.ceded.de/en/toms/tommi-plus/reference.html. Online; accessed 20-July-2019.

[140] L. Blum et al. "Recent results in Jülich solid oxide fuel cell technology development." In: *Journal of Power Sources* 241 (2013), pp. 477–485. DOI: 10.1016/j.jpowsour.2013.04.110.

[141] X. Wang et al. "Experimental and numerical studies of a bifunctional proton conducting anode of ceria-based SOFCs free from internal shorting and carbon deposition." In: *Electrochimica Acta* 264 (2018), pp. 109–118. DOI: 10.1016/j.electacta.2018.01.117.

[142] H. Noh et al. "Sandwiched ultra-thin yttria-stabilized zirconia layer to effectively and reliably block reduction of thin-film gadolinia-doped ceria electrolyte." In: *Journal of the Ceramic Society of Japan* 123.1436 (2015), pp. 263–267. DOI: 10.2109/jcersj2.123.263.

[143] H. Timmermann et al. "Kinetics of (reversible) internal reforming of methane in solid oxide fuel cells under stationary and APU conditions." In: *Journal of Power Sources* 195.1 (2010), pp. 214–222. DOI: 10.1016/j.jpowsour.2009.07.019.

[144] C. Ahamer et al. "Revisiting the Temperature Dependent Ionic Conductivity of Yttria Stabilized Zirconia (YSZ)." In: *Journal of The Electrochemical Society* 164.7 (2017), F790–F803. DOI: 10.1149/2.0641707jes.

[145] A. Pimenov. "Ionic conductivity and relaxations in ZrO_2-Y_2O_3 solid solutions." In: *Solid State Ionics* 109.1-2 (1998), pp. 111–118. DOI: 10.1016/s0167-2738(98)00082-4.

[146] Aigars. "Study of the alternating current electrical properties of ZrO_2—7.5 mol %Y_2O_3 ceramics at room temperature and at 457–595 K." In: *Journal of Solid State Electrochemistry* 5.7-8 (2001), pp. 479–486. DOI: 10.1007/s100080000177.

[147] M. Boulouz, F. Tcheliebou, and A. Boyer. "Electrical and optical properties of magnetron-sputtered Y2O3 stabilized ZrO2 thin films." In: *Journal of the European Ceramic Society* 17.14 (1997), pp. 1741–1748. DOI: 10.1016/s0955-2219(97)00035-6.

[148] J. Tao, A. Dong, and J. Wang. "The Influence of Microstructure and Grain Boundary on the Electrical Properties of Scandia Stabilized Zirconia." In: *MATERIALS TRANSACTIONS* 54.5 (2013), pp. 825–832. DOI: 10.2320/matertrans.m2012385.

[149] H. Yamamura, S. Takeda, and K. Kakinuma. "Relationship between oxide-ion conductivity and dielectric relaxation in Sm-doped CeO2." In: *Solid State Ionics* 178.13-14 (2007), pp. 889–893. DOI: 10.1016/j.ssi.2007.04.013.

[150] A. K. Baral and V. Sankaranarayanan. "Electrical study and dielectric relaxation behavior in nanocrystalline $Ce_{0.85}Gd_{0.15}O_{2-\delta}$ material at intermediate temperatures." In: *Applied Physics A* 98.2 (2009), pp. 367–373. DOI: 10.1007/s00339-009-5391-z.

[151] A. S. Nowick, A. V. Vaysleyb, and I. Kuskovsky. "Universal dielectric response of variously dopedCeO2ionically conducting ceramics." In: *Physical Review B* 58.13 (1998), pp. 8398–8406. DOI: 10.1103/physrevb.58.8398.

[152] S. Omar et al. "Electrical conductivity of 10 mol% Sc_2O_3–1 mol% M_2O_3–ZrO_2 ceramics." In: *Journal of the American Ceramic Society* 95.6 (2012), pp. 1965–1972. DOI: 10.1111/j.1551-2916.2012.05126.x.

[153] S. Yarmolenko et al. "Phase Stability and Sintering Behavior of 10 mol% Sc_2O_3 - 1 mol% CeO_2 - ZrO_2 Ceramics." In: *Journal of Fuel Cell Science and Technology* 6.2 (2009), p. 021007. DOI: 10.1115/1.2971126.

[154] F. Ciacchi, K. Crane, and S. Badwal. "Evaluation of commercial zirconia powders forsolid oxide fuel cells." In: *Solid State Ionics* 73.1-2 (1994), pp. 49–61. DOI: 10.1016/0167-2738(94)90263-1.

[155] X. Guo et al. "Ionic conduction in zirconia films of nanometer thickness." In: *Acta Materialia* 53.19 (2005), pp. 5161–5166. DOI: 10.1016/j.actamat.2005.07.033.

[156] Z. Wang et al. "Structure and impedance of ZrO_2 doped with Sc_2O_3 and CeO_2." In: *Materials Letters* 59.19-20 (2005), pp. 2579–2582. DOI: 10.1016/j.matlet.2004.07.065.

[157] J. Tan et al. "Preparation and conductivity of Sc_2O_3–CeO_2–ZrO_2." In: *Solid State Ionics* 292 (2016), pp. 22–26. DOI: 10.1016/j.ssi.2016.03.018.

[158] H. P. Dasari et al. "Synthesis, sintering and conductivity behavior of ceria-doped Scandia-stabilized zirconia." In: *Solid State Ionics* 263 (2014), pp. 103–109. DOI: 10.1016/j.ssi.2014.05.013.

[159] S. Wang et al. "Electrical and Ionic Conductivity of Gd-Doped Ceria." In: *Journal of The Electrochemical Society* 147.10 (2000), p. 3606. DOI: 10.1149/1.1393946.

[160] M. F. Öksüzömer et al. "Microstructure and ionic conductivity properties of gadolinia doped ceria ($Gd_xCe_{1-x}O_{2-x/2}$) electrolytes for intermediate temperature SOFCs prepared by the polyol method." In: *Ceramics International* 39.7 (2013), pp. 7305–7315. DOI: 10.1016/j.ceramint.2013.02.069.

[161] S. Asakura and F. Oosawa. "Interaction between particles suspended in solutions of macromolecules." In: *Journal of Polymer Science* 33.126 (1958), pp. 183–192. DOI: 10.1002/pol.1958.1203312618.

[162] P. Z. Cai, D. J. Green, and G. L. Messing. "Constrained Densification of Alumina/Zirconia Hybrid Laminates, I: Experimental Observations of Processing Defects." In: *Journal of the American Ceramic Society* 80.8 (2005), pp. 1929–1939. DOI: 10.1111/j.1151-2916.1997.tb03075.x.

[163] D.-S. Kim et al. "Improvement of grain-boundary conduction in gadolinia-doped ceria via post-sintering heat treatment." In: *Solid State Ionics* 177.19-25 (2006), pp. 2125–2128. DOI: 10.1016/j.ssi.2005.12.014.

[164] C. Xia and M. Liu. "Low-temperature SOFCs based on $Gd_{0.1}Ce_{0.9}O_{1.95}$ fabricated by dry pressing." In: *Solid State Ionics* 144.3-4 (2001), pp. 249–255. DOI: 10.1016/S0167-2738(01)00980-8.

[165] S. Zha et al. "GDC-based low-temperature SOFCs powered by hydrocarbon fuels." In: *Journal of The Electrochemical Society* 151.8 (2004), A1128–A1133. DOI: 10.1149/1.1764566.

[166] J. S. Ahn et al. "Performance of IT-SOFC with $Ce_{0.9}Gd_{0.1}O_{1.95}$ functional layer at the interface of $Ce_{0.9}Gd_{0.1}O_{1.95}$ electrolyte and Ni-$Ce_{0.9}Gd_{0.1}O_{1.95}$ anode." In: *Fuel Cells* 9.5 (2009), pp. 643–649. DOI: 10.1002/fuce.200900005.

[167] S. Cho et al. "High power density thin film SOFCs with YSZ/GDC bilayer electrolyte." In: *Electrochimica Acta* 56.16 (2011), pp. 5472–5477. DOI: 10.1016/j.electacta.2011.03.039.

[168] F. Han. "Sol-gel and nano-suspension electrolyte layers for high performance solid oxide fuel cells." PhD thesis. Ruhr-Universität Bochum, 2010. ISBN: 978-3-89336-694-1.

ABSTRACT

Solid oxide fuel cells (SOFCs) operating at low temperature (500 °C) enable applications, such as auxiliary power units (APUs) or portable devices. However, the state-of-the-art electrolyte material (yttria-stabilized zirconia (YSZ)) used in intermediate-temperature SOFCs does not provide a sufficiently high ionic conductivity.

Two approaches can therefore be taken to deal with that. First, an alternative electrolyte material to YSZ with a higher conductivity. However, when looking for alternatives, the conductivity values for each material found in widely-cited literature can be confusing, as the reported values are sometimes in conflict with each other. Second, an electrolyte film with thinner thickness. While spin coating is reported to be able to fabricate a YSZ electrolyte with thickness as thin as 1 µm, further thickness decrease by spin coating is a big challenge. Moreover, spin coating is very time consuming, needing multiple steps of coating, drying and heat-treatment, which could take several days.

Therefore, in this study we present a systematic comparison of the conductivity of the three most popular electrolyte materials, i. e., YSZ, scandium-stabilized zirconia (ScSZ), and gadolinium-doped ceria (GDC). Using electrochemical impedance spectroscopy (EIS) to characterize the ionic conductivity, we find that at 500 °C, GDC has a higher ionic conductivity (5.8×10^{-3} S cm^{-1}) than ScSZ (2.5×10^{-3} S cm^{-1}) and YSZ (1.1×10^{-3} S cm^{-1}). The properties of the starting powders, powder processing and the microstructure after sintering are all taken into account. Following up on this, a GDC electrolyte is developed on an industrial scale anode, with a dimension of 5 cm×5 cm, by screen printing. After sintering at 1400 °C for 5 h, a thin and dense GDC electrolyte, with thickness of 3.5 µm and air leakage rate of 3.54×10^{-6} hPa dm^2 s^{-1} cm^{-2}, is achieved. The single cell test shows the cell has a high cell performance, a measured voltage of 0.84 V at a current density of 2 A cm^{-2} and 750 °C (air, H_2 with 10 % H_2O). According to the EIS, a quite low ohmic resistance is achieved, 125.2 mΩ cm^2 at 500 °C.

This comparison of conductivity can be used as a guide when deciding on electrolyte materials for different SOFC applications, especially when the fabrication of the electrolyte layer of different thickness has to be considered, and rectify misleading information in the literature. The development of the thin and dense GDC electrolyte provides a strategy of using GDC as electrolyte for SOFC and confirms the advantage of using GDC while not YSZ for low temperature SOFC, which is the fabrication challenge can be decreased significantly.

ZUSAMMENFASSUNG

Eine Absenkung der Betriebstemperatur von Festoxidbrennstoffzellen (SOFCs) in den Bereich um 500 °C wird angestrebt um Anwendungsfelder wie Brennstoffzellengeneratoren für mobile Anwendungen zu erschließen. Jedoch weist yttriumstabilisiertes Zirkonoxid (YSZ), der nach aktuellem Stand der Technik verwendete Elektrolytwerkstoff, eine unzureichende ionische Leitfähigkeit in diesem Niedertemperaturbereich auf.

Zwei Lösungsansätze können hier Abhilfe schaffen. Der erste, weitverbreitete Ansatz ist die Verwendung eines alternativen Elektrolytwerkstoffs mit höherer Leitfähigkeit. Ein Vergleich von in der relevanten Fachliteratur angegebenen Daten zeigt allerdings uneinheitliche Leitfähigkeitswerte der einzelnen Werkstoffe und deren Verhältnisse zueinander. Der zweite Ansatz ist eine Verringerung der Elektrolytdicke. Über Schleuderbeschichtung (engl: spin coating) können Schichtdicken von etwa 1 µm realisiert werden. Diese Herstellungsmethode ist sehr arbeitsintensiv, da mehrfache Durchläufe von Beschichtungszyklus, Trocknung und Wärmebehandlung notwendig sind. Zudem stellt eine weitere Reduzierung der Schichtdicke eine große Herausforderung dar.

Ziel dieser Arbeit ist ein systematischer Vergleich der ionischen Leitfähigkeit der drei überwiegend verwendeten und kommerziell erhältlichen Elektrolytwerkstoffe. Diese sind YSZ, scandiumstabilisiertes Zirkonoxid (ScSZ) und gadoliniumdotiertes Ceroxid (GDC). Mittels elektrochemischer Impedanzspektroskopie (EIS) konnte gezeigt werden, dass GDC mit $5{,}8 \times 10^{-3}\,\mathrm{S\,cm^{-1}}$ eine höhere ionische Leitfähigkeit bei 500 °C aufweist als ScSZ ($2{,}5 \times 10^{-3}\,\mathrm{S\,cm^{-1}}$) und YSZ ($1{,}1 \times 10^{-3}\,\mathrm{S\,cm^{-1}}$). Diese Analyse erfolgte unter Berücksichtigung von Ausgangspulver, Herstellungsmethode und resultierender Mikrostruktur nach der Sinterung. In weiterführenden Versuchen wurde ein Prozessablauf für die Herstellung eines $5\,\mathrm{cm} \times 5\,\mathrm{cm}$ GDC Elektrolyten über Siebdruck auf eine herkömmliche anodengestützte Zelle entwickelt. Nach der Sinterung bei 1400 °C für 5 Stunden wurde eine Elektrolytdicke von 3,5 µm erreicht, sowie eine ausreichende Luftdichtigkeit mit einer Leckrate von $3{,}54 \times 10^{-6}\,\mathrm{hPa\,dm^2\,s^{-1}\,cm^{-2}}$ ermittelt. Die elektrochemische Charakterisierung einer solchen Einzelzelle zeigte eine hohe Leistungsfähigkeit von $2\,\mathrm{A\,cm^{-2}}$ bei 750 °C und einer Zellspannung von 0,84 V (Kathodengas: Luft, Anodengas: 10 % H_2O in H_2). Mittels EIS wurde ein ohmscher Widerstand von $125{,}2\,\mathrm{m\Omega\,cm^2}$ bei 500 °C ermittelt.

Der vorliegende Vergleich der ionischen Leitfähigkeiten kann als Referenz für weiterführende Arbeiten dienen und Hilfestellung bei der Auswahl eines geeigneten Elektrolytwerkstoffs für die jeweils angestrebte SOFC Anwendung leisten. Dies gilt insbesondere, wenn die

Herstellung unterschiedlicher Schichtdicken berücksichtigt werden soll. Diese Arbeit bietet somit eine solide Basis zur Weiterentwicklung, die in der zuvor publizierten Literatur durch teils widersprüchliche Angaben nicht gegeben war. Die erfolgreiche Entwicklung der dünnen und dichten GDC Elektrolytschicht zeigt die Anwendbarkeit von GDC auf üblichen SOFC Substraten und bestätigt die höhere Leistungsfähigkeit im Vergleich zu YSZ, während ein hoher Herstellungsaufwand für sub-µm Schichten vermieden wird.

Band / Volume 478
Mechanische Eigenschaften von Polymer-Elektrolyt-Membran-Brennstoffzellen
P. Irmscher (2019), vii, 177 pp
ISBN: 978-3-95806-435-5

Band / Volume 479
Morphology and Degradation of High Temperature Polymer Electrolyte Fuel Cell Electrodes
S. Liu (2019), III, 162 pp
ISBN: 978-3-95806-436-2

Band / Volume 480
Structural uptake and retention of safety relevant radionuclides by cementitious materials
S. Lange (2019), 133 pp
ISBN: 978-3-95806-437-9

Band / Volume 481
Quantifying the Impact of Inhomogeneity, Transport and Recombination in Emerging Thin-Film Solar Cells
P. Kaienburg (2019), vii, 258 pp
ISBN: 978-3-95806-440-9

Band / Volume 482
Studies of oxidation resistant tungsten alloys at temperatures of 1100K to 1475K
F. Klein (2019), 158 pp
ISBN: 978-3-95806-444-7

Band / Volume 483
Impact Assessment of Land-Use Change and Agricultural Treatments on Greenhouse Gas Emissions from Wetlands of Uganda and Tanzania
K. X. X. Wagner (2019), 144 pp
ISBN: 978-3-95806-447-8

Band / Volume 484
IEK-3 Report 2019
Tailor-Made Energy Conversion for Sustainable Fuels
D. Stolten, B. Emonts (Eds.) (2020), 162 pp
ISBN: 978-3-95806-451-5

Band / Volume 485
Multiskalare Modellierung integrierter Energie- und Elektrizitätssysteme
T. C. Pesch (2019), XXV, 384 pp
ISBN: 978-3-95806-452-2

Band / Volume 486
Quantitative Untersuchung des Laserablationsprozesses mittels Kombination von optischer Spektroskopie und Massenspektrometrie
J. Oelmann (2020), vii, 141 pp
ISBN: 978-3-95806-453-9

Band / Volume 487
Leistungssteigerung metallgestützter Festelektrolyt-Brennstoffzellen (MSCs) durch gezielte Optimierungen des Anoden/Elektrolytverbunds
C. Bischof (2020), X, 176 pp
ISBN: 978-3-95806-455-3

Band / Volume 488
Aluminiumoxiddispersionsverstärkte Haftvermittlermaterialien in Wärmedämmschichtsystemen
C. Vorkötter (2020), VIII, 99, XXXIII pp
ISBN: 978-3-95806-457-7

Band / Volume 489
The Balmer lines emission of fast hydrogen atoms at the plasma-solid interface in a low density plasma: challenges and applications
S. O. Dickheuer (2020), 117 pp
ISBN: 978-3-95806-458-4

Band / Volume 490
Micromechanical Characterization of Ceramic Solid Electrolytes for Electrochemical Storage Devices
J. F. Nonemacher (2020), xv, 131 pp
ISBN: 978-3-95806-461-4

Band / Volume 491
Nanoscale investigation of high temperature oxidation mechanisms of high-Cr ferritic steels
A. Vayyala (2020), xix, 105 pp
ISBN: 978-3-95806-467-6

Band / Volume 492
Electrolyte development for a SOFC operating at low temperature
J. Zhang (2020), vi, 121 pp
ISBN: 978-3-95806-471-3

Weitere ***Schriften des Verlags im Forschungszentrum Jülich*** unter
http://wwwzb1.fz-juelich.de/verlagextern1/index.asp

Energie & Umwelt / Energy & Environment
Band / Volume 492
ISBN 978-3-95806-471-3

Mitglied der Helmholtz-Gemeinschaft

JÜLICH
Forschungszentrum